Comprehensive Characterization of Deeply Penetrating Charged Droplet Signatures in the High-Vacuum Region of Electrospray Ionization Mass Spectrometry

---

Chris Vico Heintz

May 15, 2025

University of Wuppertal

BERGISCHE
UNIVERSITÄT
WUPPERTAL

School of Mathematics and Natural Sciences
Physical and Theoretical Chemistry

Dissertation

Comprehensive Characterization of Deeply Penetrating Charged Droplet Signatures in the High-Vacuum Region of Electrospray Ionization Mass Spectrometry

Chris Vico Heintz

1. Reviewer Prof. Dr. Thorsten Benter
Physical and Theoretical Chemistry
University of Wuppertal, Germany

2. Reviewer Prof.'in Dr. Julia Bornhorst
Food Chemistry
University of Wuppertal, Germany

3. Reviewer Prof. Dr. Scott Hopkins
Department of Chemistry
University of Waterloo, Canada

Supervisor Dr. Walter Wißdorf

May 15, 2025

Chris Vico Heintz

Comprehensive Characterization of Deeply Penetrating Charged Droplet Signatures in the High-Vacuum Region of Electrospray Ionization Mass Spectrometry

Dissertation, May 15, 2025
Reviewers: Prof. Dr. Thorsten Benter, Prof.'in Dr. Julia Bornhorst and Prof. Dr. Scott Hopkins
Supervisor: Dr. Walter Wißdorf

University of Wuppertal
Physical and Theoretical Chemistry
School of Mathematics and Natural Sciences
Gaußstraße 20
42119 Wuppertal

„Und im Stillen nahm er sich vor nie wieder vor irgendetwas oder irgendwem Angst zu haben, bevor er ihn oder es nicht aus der Nähe betrachtet hätte. Man konnte ja nie wissen, ob es nicht so ähnlich war wie mit Herrn Tur Tur. Er gab sich in Gedanken selbst das Ehrenwort, immer daran zu denken."

— Michael Ende, Jim Knopf
und Lukas der Lokomotivführer

Abstract

Electrospray ionization (ESI) is one of the most widely used techniques in modern mass spectrometry. This work complements and, in part, contradicts the knowledge shared in textbooks and publications about the dynamics of charged droplets generated by ESI in mass spectrometers. It was commonly assumed that those droplets evaporate entirely in the spray chamber and bare ions enter the mass spectrometer. This work reports on the observation of signatures of charged droplets originating from ESI within the detector region of a commercial time-of-flight (TOF) instrument. An oscilloscope connected directly to the on-axis auxiliary control device detected the droplet signatures as intensive bursts of the ion current signal downstream of the orthogonal acceleration (oa) stage. These ion bursts exhibit an intensity and a width significantly larger than those of the average continuous ESI current, whereby the intensity and width vary from burst to burst. The appearance frequency of the signal bursts depends on different source parameters, primarily on those that are most crucial for spray generation.

Long-term experiments demonstrate that the investigated instruments need a stabilization time of about 30 to 60 minutes, during which the ion signals and droplet signature frequency fluctuate. Generally, the rate of observed droplet signatures decreased during the experiments. However, they never disappeared completely. It was determined that ion signals in subsequent experiments stabilized much faster than 30 minutes, which is the typical observed stabilization time for the initial run. After the initialization, the droplet frequency remained relatively low. However, the longer the rest time of the instrument between the experiments, the more time is needed for the re-stabilization of the signal intensities and the droplet signature frequency. A rest time of more than a couple of hours leads to stabilization times of about 30 minutes, as observed in the initial measurement. This recovery to the initial state was significantly accelerated by switching the instrument's polarity mode for a brief period.

Another method for detecting droplet signatures involves analyzing single TOF mass spectra. Typically, thousands of these spectra are combined into a summed mass spectrum. An examination of the single mass spectra indicates a few exceptionally

high-intensity spectra, whereas the majority of the spectra appear to contain no signals at all. The analytical operation mode of TOF instruments wipes out these details completely.

All experiments were repeated using alternative ionization methods, specifically atmospheric pressure chemical ionization (APCI) and atmospheric pressure photoionization (APPI). This approach was used to validate that the observed phenomena can be attributed solely to ESI and do not occur using other ionization techniques.

Danksagung

Als ich 2014 für mein Bachelorstudium an die BUW kam, kannte ich niemanden. Aus meiner Stufe studierten zwar eine Hand voll Leute ebenfalls an der Uni Wuppertal, aber niemand schrieb sich für Chemie ein. Schon in einer der Übungsgruppen im Mathe-Vorkurs lernte ich dann aber Nils kennen. In den ersten Vorlesungen machte ich dann Bekanntschaft mit den Menschen, die mich mein gesamtes Studium bis zur Promotion begleitet haben. Neben Nils waren das Julia, Nicole, Oskar, Moritz, Laura und Daniela. Sie tragen einen bedeutenden Anteil daran, dass ich mich am Ende für die Promotion entschieden habe.

2015 hörte ich "Einführung in die Thermodynamik" bei einem gewissen Prof. Dr. Thorsten Benter. Donnerstags um 8 Uhr morgens... "Das hat der sich bestimmt selbst überlegt, um den Studierenden zu zeigen, dass man in der Chemie früh aufstehen muss...", dachte ich. Meine ersten Vorbehalte gegen ihn verebbten, als ich dann sah, dass diese Uhrzeit für jenen Herrn Benter ein größeres Problem darstellte, als für mich und er müde betonte, dass sein Ruf nach einem anderen Zeitslot seit vielen Jahren keine Beachtung findet. Ein paar Wochen vergingen und Thermodynamik stellte sich als recht trockene Materie heraus. Durch die lockere Art des Professors war es aber im Großen und Ganzen ganz okay. Wurde die Mathematik mal etwas haariger, beruhigte Professor Benter uns und sagte: "Das ist ganz normal". Er würde seiner Tochter regelmäßig die banalsten Sachen erklären müssen.

Ausgleich vom Studium habe ich unter anderem bei meinen Freunden gesucht. Ich hatte vor einigen Jahren auf irgendeiner Party eine Merle kennengelernt. Den Nachnamen kannte ich damals nicht und eigentlich kannten wir uns die ersten Jahre sowieso immer nur betrunken. Viel später fragte sie mich, was ich eigentlich arbeiten würde. "Ich studiere Chemie in Wuppertal", entgegnete ich in der Erwartung gleich das klassische "Uhhh Chemie, das hab‘ ich ganz schnell abgewählt!" zu hören. So etwas in der Art kam dann auch, aber gefolgt von einem "Aber mein Vater ist Professor für Chemie in Wuppertal! Kennst du ihn?". Es stellte sich heraus, dass Professor Benter niemand geringeres als Merles Vater war. Interessant... aber an der trockenen Thermodynamik änderte das leider nichts...

Am Ende der Thermodynamik-Vorlesung zeigte Prof. Benter uns ein paar Folien über die Dinge, die seine Arbeitsgruppe eigentlich so macht. Das sah unerwartet cool aus und vor allem wenig nach Thermodynamik! Die siebte Folie über Laser überzeugte mich dann. Motiviert gingen Nils und ich in einem Anflug von übersteigertem Selbstbewusstsein eines Nachmittags zu Prof. Benter und fragten, ob man nicht mal ein paar dieser coolen Messungen begleiten könne... So als Vorbereitung für die Bachelorarbeit. Na aber sicher ging das! Prof. Benter war ab diesem Zeitpunkt Thorsten und wir waren von da an Teil der Arbeitsgruppe. Auch wenn viele sich zunächst nicht ganz sicher waren, wer Chris und wer Nils war.

Thorsten versuchte uns von Anfang an beizubringen, dass Neugierde das Wichtigste am Experimentieren sei. Man solle sich nicht abschrecken lassen von diesen hübschen Plastik Verschalungen, welche die Instrumente oft von außen einhüllen. Weg damit! Sonst sieht man ja gar nicht was drinnen ist! "Und wenn mal eine Glaskapillare abbricht: Doof, diese Dinger sind teuer, aber shit happens! Nehmt euch die nächste aus der Packung! Und wenn die wieder abbricht, noch eine! Und bei der Dritten fragt ihr euch am besten mal kurz: Mache ich hier vielleicht strukturell etwas falsch?" Und nach diesem Motto habe ich seitdem immer gearbeitet (meine erste und einzige Glaskapillare habe ich übrigens erst in der Promotion abgebrochen!)

Nils und ich bekamen das alte Büro von Detlef Fuchs zugeteilt, zumindest einen Teil davon, den Rest mussten wir uns mit alten kaputten Oszilloskopen, Kabelboxen, diversen Monitoren aus dem 18. Jahrhundert und Kram teilen. Detlef hatte ihn uns netterweise zum "Durchgucken, ob noch was Gutes dabei ist" in praktischer Chaos-Lagerhaltung dagelassen.

Nach und nach lernten wir dann den Rest der Arbeitsgruppe kennen. Klaus versorgte uns mit SHK Verträgen, damit wir in KDs Praktikum erste Lehrerfahrungen sammeln konnten. Dort lernten wir auch Markus, Joshi, Clara und Steffen kennen, die gerade ihre Bachelorarbeit geschrieben haben und mich in weiten Teilen meines Studiums und Promotion begleitet haben! Mit Yessi zusammen durfte ich meine erste Kapillarstrommessung machen und schnell lernte ich dadurch auch Valerie, David, Walter, Christine, Alex, Kai, Marco, Robin, Stefan und Duygu kennen.

Vor Ronnie sollte ich mich in Acht nehmen wurde mir gesagt, "der kann mal böse werden, wenn du dich sehr dumm anstellst!". Meistens habe ich mich nicht sehr dumm angestellt, allenfalls ein bisschen...

Walter hat mich nicht nur während meiner Bachelorarbeit und meiner kompletten Promotion betreut und begleitet, sondern war seitdem immer DER Ansprechpartner für wissenschaftliche Fragen oder wenn ich wissen wollte, wie das Wetter so wird (Kachelmann-Wetter sei Dank!). Ich bin bis heute nicht ganz dahintergekommen,

wie Walters Gehirn funktioniert und bin in regelmäßigen Abständen im positivsten Sinne erstaunt über so viel analytischen Verstand und Wissen.

Hendrik habe ich während meiner Zeit in vielen Hinsichten sehr liebgewonnen. In den Vorlesungen hat er wirklich alles gegeben die Inhalte möglichst lebendig wirken zu lassen und hat beispielsweise sehr eindrucksvoll mit seinem ganzen Körper die Flugbahn einzelner Partikel dargestellt. Als Ansprechpartner hatte er immer ein offenes Ohr und hat bei allem tatkräftig unterstützt. Manchmal bis spät in den Abend hinein, bis er Nachrichten von zu Hause bekam und dann schnell wegmusste. Später haben wir sogar als Segel-Kumpane so manchen See unsicher gemacht (Unterbacher See und Bevertalsperre; mit unsicher ist vor allem Hendriks Wende gemeint, bei der er selbst über Bord gegangen ist).

Thorsten wurde zu meinem Doktorvater und war der beste Chef, den man sich wünschen kann. Es gab nie ein “das geht nicht”, sondern ein “mal schauen was geht”. Meistens ging viel. So sehr ich Thorstens wissenschaftliche Expertise auch schätze, ich werde ihn als Chef vor allem für seine Menschlichkeit vermissen. Gott sei Dank muss man in keinem Angestelltenverhältnis zueinanderstehen, um gemeinsam Ritas und Korn trinken zu dürfen, denn davon wird es hoffentlich noch ein paar geben. Mindestens HUNDERTSECHSUNDNEUNZIG!

Neben dem Studium blieb sogar Zeit für weitere Aktivitäten. Hier bin ich vor allem Kristina dankbar, die mich damals motiviert hat zusammen mit Julia ins JCF zu kommen. Mir gefiel es, mich mit anderen jungen Chemie-Studierenden zu vernetzen. Im Laufe meiner vielen Jahre im JCF, egal ob in Wuppertal oder auf Bundesebene, habe ich sehr, sehr viel gelernt, habe einmalige Einblicke in die Berufswelt bekommen und vor allem viele tolle Menschen kennenlernen dürfen. Hierbei möchte ich vor allem Lorin, Anna, Claudia, Emiel, Feli, Melina, Caro, Monja, Rahel, Karen, Hannah und Max Danke sagen!

Meine spätere Tätigkeit im QSL-Netzwerk der Uni hat mir ebenfalls viel über mich und Reakkreditierungen von Studiengängen beigebracht. An dieser Stelle möchte ich mich ganz besonders bei Isabella bedanken, die immer für alles Verständnis hat und ganz besonders gut zuhören kann. Außerdem Peter und Francesco, die mich als Dekane in vielem sehr unterstützt haben. Mein Dank gilt natürlich auch den anderen QSLern unserer Fakultät, Vera, Michelle, Tom und René ohne deren tolle und engagierte Arbeit sehr viel mehr Arbeit an mir hängen geblieben wäre.

Die Leute, mit denen ich in der Arbeitsgruppe angefangen hatte, verschwanden allmählich und es rückte eine zweite Generation nach. Den Anfang machten Sanna und Niklas, mit denen mich sehr viel gemeinsame Zeit verbindet. Die beiden waren für mich in allen Lebenslagen da und vor allem zeichnet sie aus, dass man mit den

beiden immer eine gute Zeit hat! Und dabei ist es egal ob auf dem Festival, auf Konferenzen, bei Sportevents, oder was auch immer. Sanna, Niklas, lecker Bierchen und es läuft!

Nicht unerwähnt lassen möchte ich Michelle, die während unserer gemeinsamen Promotion eine Freundin geworden ist und immer einen Platz in meinem Herzen haben wird. Ich bin mir sicher, dass sie meine vielen (aus ihrer Sicht sicher trivialen) Fragen vermissen wird! Maja begleitet mich schon sehr lange. Ich habe sie damals in meinem ersten PC0 Praktikum betreut! Scheinbar so gut, dass sie sich auch zur Promotion bei uns entschlossen hat :)

Mit Adem (Bdem, Cdem und Gott bewahre auch Ddem) und Ferdi habe ich mir die längste Zeit meiner Promotion ein Büro geteilt. Ferdi hat sich unvergessen rührend um mein entzündetes Ohr auf der ASMS 2023 gekümmert. Dafür gebührt ihm mein ewiger Dank. Weniger dankbar bin ich ihm für die Erfindung des "Verteilerrats", einer Weiterentwicklung des klassischen Biertrichters.

Die Doktorand*innen der dritten Generation heißen Lena, Laura, Franzi, Markus, Paty, Alex und Maja. Ich habe euch auch spätestens nach der ersten gemeinsamen Konferenz ins Herz geschlossen, und in Alex Fall: der ersten gemeinsamen Hochzeit! Ihr macht das Leben in der PTC bunter und seid für jeden Spaß zu haben. Behaltet euch das bei!

Daniela ist für mich das gute Herz der Arbeitsgruppe. Sie weiß immer über alles Bescheid und hilft wo sie kann. Neben der ganzen Hilfe, die ich in den vielen Jahren von ihr erhalten habe, bleiben mir vor allem unsere vielen tollen Gespräche in Erinnerung!

Zu guter Letzt gilt mein Dank natürlich meinen Eltern, Großeltern, Geschwistern, Vivi und so vielen weiteren Menschen, die nicht direkt Einfluss auf die Promotion genommen haben, aber mich dafür indirekt sehr viel unterstützt haben und mich einfach so genommen haben, wie ich bin (und man munkelt, dass das gar nicht so einfach sei, manchmal...).

Contents

1 Introduction

1.1 How to Read This Work

This dissertation is a cumulative work. It combines the findings and content of three publications that have been published in recent years. An overview of all three publications is provided in section 3, just before the sections discussing the publications in section 4, section 5, and section 6.

Although every publication introduces the topic, they assume some prior knowledge. Therefore, this thesis provides a broader introduction to both the topic and the instruments used. Section 1.2 outlines some general aspects of mass spectrometry, which are crucial for this work. Furthermore, the section will introduce the specific topic of aspirated droplets with electrospray ionization, including a summary of the prior work in this field. For those who have not encountered electrospray before, it is advisable to read section 1.3 first.

A more detailed description of typical components of a mass spectrometer, particularly focusing on the Bruker micrOTOF, is presented in section 2. This section describes the used instrument and the experimental setup. Section 7 summarizes the findings of all publications and adds additional information.

1.2 Context and Background

Mass spectrometry (MS) is an analytical technique for determining the mass-to-charge ratio (m/z) of substances of interest (analytes) within a sample. It has applications in various fields, including biotechnology, environmental studies, quality assurance, and forensics.

Although there are many mass spectrometers for various applications, they typically consist of four components: an inlet system, an ionization source, a mass analyzer, and a detector (see Figure 1.1). Each of these components can have different specifications based on the intended application of the mass spectrometer. For example, a liquid sample requires a different inlet system than a gaseous one, and a

Fig. 1.1: Scheme of the four segments of a generalized mass spectrometer.

rapid online analysis often leads to lower resolution than a single measurement with the highest possible resolution.

Although there are countless possible combinations of components, the functionality of the mass spectrometer can be summarized in just a few sentences to provide a general understanding.

Typically, a sample (collected from the environment, human body, etc.) contains a mixture of various molecules that are mostly neutral. Electrical fields cannot affect the trajectories of neutral particles and molecules, so the molecules are initially ionized. Consequently, these ions can be influenced by the electrical fields generated by electrodes inside the mass spectrometer. The *mass analyzer* acts as a dispersing device that separates different ions based on their mass-to-charge ratio. Filtering can be accomplished through various mechanisms, such as different flight times (see section 2.5). The separated ions must be converted into a measurable signal that the operator can analyze on a computer. A mass spectrometer produces a mass spectrum that contains information about the mass-to-charge (m/z) ratios of detected ions, as well as their relative intensities, which represent ion abundance as a function of the m/z ratio. A mass spectrum does not directly provide information about all analytes present within the sample without additional data from other analytical methods.

The properties of different samples are diverse. In the simplest case, a sample is gaseous and consists of only a few other components. In this scenario, one can easily ionize the gas, for example, through electron bombardment, and direct the resulting ions into the mass spectrometer. The process becomes more complicated when the samples are solid or liquid. Because it is not feasible to directly introduce a liquid into a mass spectrometer without further preparation, the analyte within the liquid must be transferred to the gas phase. The most commonly used method to achieve this is electrospray ionization (ESI). A detailed overview of the ESI mechanism, as currently understood, is provided in section 1.3.1. In summary, ESI employs an analyte-containing solution pumped through a thin metal needle into an electric field, generating a plume of small, charged liquid droplets. These

droplets undergo a shrinking mechanism characterized by the evaporation of solvent molecules, ultimately releasing bare analyte ions.

Over the decades, textbooks and other literature have suggested that droplets completely shrink to bare ions within the electrospray chamber, or at least before entering the vacuum system of a mass analyzer. Gross notes, "At this stage, desolvation of the ions is completed, while the ions are focused into a mass analyzer" [16]. Similar quotes can be found in other literature [20, 7, 4, 24, 6, 25]. However, the issue of incompletely desolvated droplets and residual, large charged clusters has been present since the early days of ESI, as described in section 1.3.2. Recent research has revealed several observations that provide evidence of droplets entering the high-vacuum areas and even the detectors of various commercial mass spectrometers.

Kang et al. [23] reported in 2017 that "ions of interest may be encapsulated within large heterogeneous clusters", which "may have multiple charges, and penetrate into downstream ion optics as far as the detector, leading to charging and contamination". Kang goes on that these clusters "can have m/z exceeding the mass range of a typical triple quadrupole instrument, and therefore they are difficult to detect using current commercially available MS techniques" [23]. However, clusters can also contain thousands of charges, leading to m/z ratios within the range typically observed by mass analyzers despite their high mass. Rajkovic et al. [32] demonstrated through molecular dynamics simulations that collisions between large clusters and surfaces (e.g., a quadrupole electrode surface) may result in the release of a group of smaller clusters that can reach the detector [32] as a correlated ion burst. Such signal bursts have been experimentally observed multiple times [28, 22, 18, 19, 17].

Markert et al. [28] reported the observation of charged droplets or droplet signatures in various API mass spectrometers with significantly different inlet systems. They primarily used a SCIEX Triple Quadrupole 6500 System with an IonDrive Turbo V ion source operated with a TurbolonSpray ESI probe (SCIEX, Ontario, Canada). They also utilized a Bruker amaZon ETD quadrupole ion trap (QIT) equipped with an Apollo ion source (Bruker Daltonics, Bremen, Germany) and an Agilent 6538 UHD Q-ToF (Agilent, Waldbronn, Germany), which also had an identical Apollo ion source. Markert used para-substituted benzylpyridinium ions, referred to as thermometer ions, producing analyte signals around m/z 200.

In contrast to the Bruker and Agilent systems, the SCIEX instrument does not use an inlet capillary as the first gas flow restriction stage; instead, it has a critical orifice located downstream of a curtain plate, which directs ions into the so-called "Q-Jet," the first focusing quadrupole. The instrument features three quadrupole areas: Q1, Q2, and Q3. Q1 can be operated in RF-only mode, meaning the direct current (DC) potential was disabled, with only the radio frequency (RF) potential

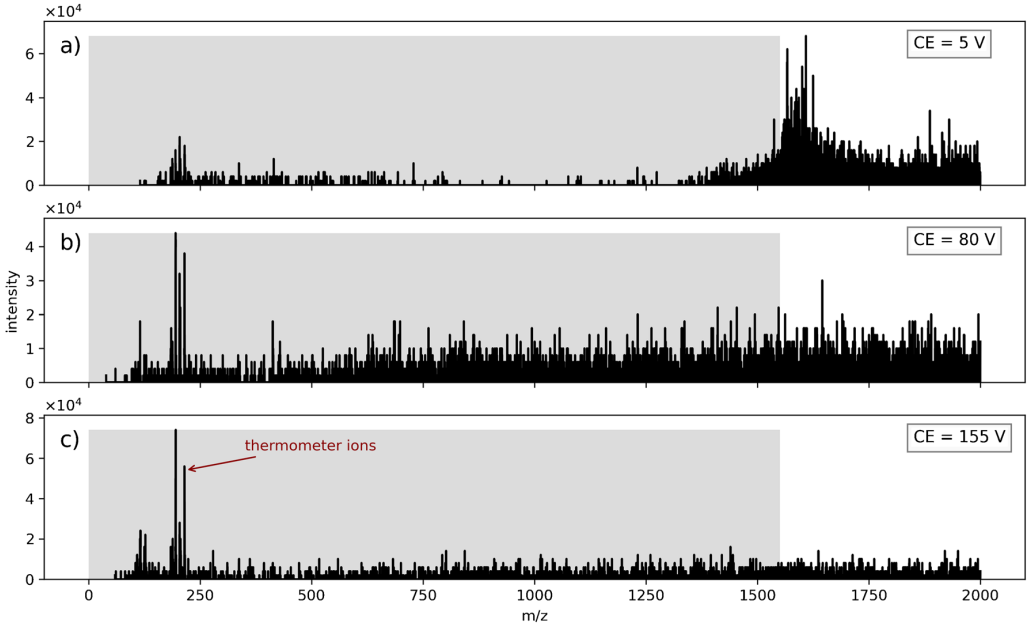

Fig. 1.2: Droplet scan at the SCIEX Triple Quad 6500 using various collision voltages. The shaded areas indicate the lower cutoff *m/z* region resulting from the first quadrupole. Figure was taken from [28].

applied to the quadrupole rods. The quadrupole becomes a high-pass filter in this mode. Consequently, droplets above the low mass cutoff (LMCO) are transmitted into Q2, a collision cell. In this cell, ions are accelerated with specific voltages ("collision energy") and are fragmented by collisions with a collision gas in collision-induced dissociation (CID) processes. Q3 performs a common *m/z* scan. With low collision energies and an LMCO set at *m/z* 1550 in this setup, Markert et al. injected thermometer ions and observed moderate-intensity signals around *m/z* 200, corresponding to the thermometer ions. Meanwhile, the strongest signals are observed just above the LMCO, as shown in Figure 1.2 [28]. Increasing the collision energy reduces this signal above the LMCO, making the thermometer ion signals around *m/z* 200 the most prominent peaks in the spectrum [28]. Markert et al. propose that droplets or droplet debris from the ESI process, aspirated into the instrument, cause the comparably intense signals observed above the LMCO. The increased collision energy in Q2 enhances collision-induced dissociation, potentially breaking down the droplets and droplet debris into their individual constituents, allowing the thermometer ions to reappear in the spectrum [28]. Their observation supports the hypothesis that increasing the collision gas pressure — and thus the number of collisions within the collision cell — produces a similar effect, even though the collision energy remains unchanged. The set of experiments was replicated using reserpine in an isopropanol/water analyte system, and similar results were obtained [28].

Markert et al. conducted a second set of experiments using the Bruker amaZon ETD quadrupole ion trap. They started by injecting thermometer ions, setting the ion isolation window to *m/z* 2500 with a width of ± 50. After a storage time of $40\,\mu\mathrm{s}$, a broad ion signal is observed within the defined isolation window with almost negligible small signals around *m/z* 200. Increasing the trapping time to $1000\,\mathrm{ms}$ results in a less intense but broader signal structure in the isolation window, and thermometer ion signals appear around *m/z* 200. The longer trapping time causes more collisions, ultimately leading to the release of analyte ions from the larger clusters or droplets [28].

The last set of experiments was conducted using an Agilent Q-ToF, which operated with the first quadrupole in RF-only mode, similar to the experiments conducted with the SCIEX instrument [28]. The LMCO was set to approximately *m/z* 2500, and the collision voltage in the subsequent collision cell was ramped from $0\,\mathrm{V}$ to $100\,\mathrm{V}$. The results are similar to those obtained with the SCIEX instrument. A collision voltage of $0\,\mathrm{V}$ allows all larger agglomerates (droplets and droplet debris) to pass through, leading to a broad signal structure around *m/z* 2000. Increasing the collision voltage flattens this peak structure, while the analyte peaks rise in the front part of the spectrum [28].

In 2024, Itzenhäuser et al. [22] built upon the work of Markert et al. [28] and refined the methods to resemble actual analytical conditions better. They replaced the syringe pump with a liquid chromatography (LC) stage and repeated the experiments with different analyte systems and various solvent ratios. The overall findings were consistent with those of Markert et al., but they also showed the influence of different instrument parameters on the composition of droplets or droplet fragments: Varying the dry gas temperature or changing the organic solvent ratio results in different shapes of the signals at high masses, which are attributed to the droplets or droplet fragments [22].

Markert [28] and Itzenhäuser [22] showed that the assumption of ESI droplets disintegrating within the spray chamber is probably not valid for at least a significant fraction. Moreover, Rajkovic's [32] simulations of colliding droplets with surfaces that produce bare analyte molecules after the impact provide a possible explanation for observing low *m/z* signals even when a lower mass cutoff is applied. The findings from this potential explanation will be crucial for the observations in the following work, which explores another method for detecting and characterizing the droplets or droplet debris aspirated deeply into the vacuum system of current mass spectrometers.

This work relates to the previously mentioned studies and investigates the droplets' fragmentation behavior under various conditions. All experiments were conducted using a Bruker micrOTOF, which is described in detail in section 2.

1.3 Electrospray Ionization

1.3.1 Operating Principle

As discussed in the last section of this chapter, the development of modern electrospray ionization was not a straightforward process. However, all the methods developed in the past shared common elements: the spraying of analyte-containing solutions into an electric field at atmospheric pressure, the addition of heat to counteract evaporative cooling, a supersonic expansion into a (rough) vacuum, and a system of differentially pumped areas within the mass spectrometer [16]. The underlying mechanism of ESI can be categorized into three main sub-processes:

1. The creation of a spray that contains charged droplets from the solution containing the analyte.

2. The shrinkage of charged droplets occurs due to the evaporation of solvent molecules and droplet fission, resulting in tiny, charged droplets that can release single ions. [25].

3. The generation of individual ions from droplets.

The name electrospray ionization is misleading. The analyte ions already exist in the solution, and ESI transfers them into the gas phase. On their way to the detector, they can undergo cluster formation, fragmentation, and reactions in the gas phase. However, the required high voltages can lead to corona discharges at the ESI spray capillary, which can influence the generation of additional ions.

A common ESI source is schematically depicted in Figure 1.3: An analyte-containing solution is pumped through a thin metal capillary with a diameter r_c of approx. $75\,\mu\mathrm{m}$ to $100\,\mu\mathrm{m}$ [16, 25]. There is a voltage V_c of about $2\,\mathrm{kV}$ to $4\,\mathrm{kV}$ applied to the spray needle [16, 25], which is typically located at a distance d of $1\,\mathrm{cm}$ to $3\,\mathrm{cm}$ from the large, mostly planar counter electrode, which has an orifice into the mass spectrometer vacuum system [25].

The electrical field E_c at the tip of the capillary (in the absence of solution) can be approximated by estimating a cylindrical electrode held at a voltage above a grounded planar electrode as described in [36, 25]. Using electrostatic approxima-

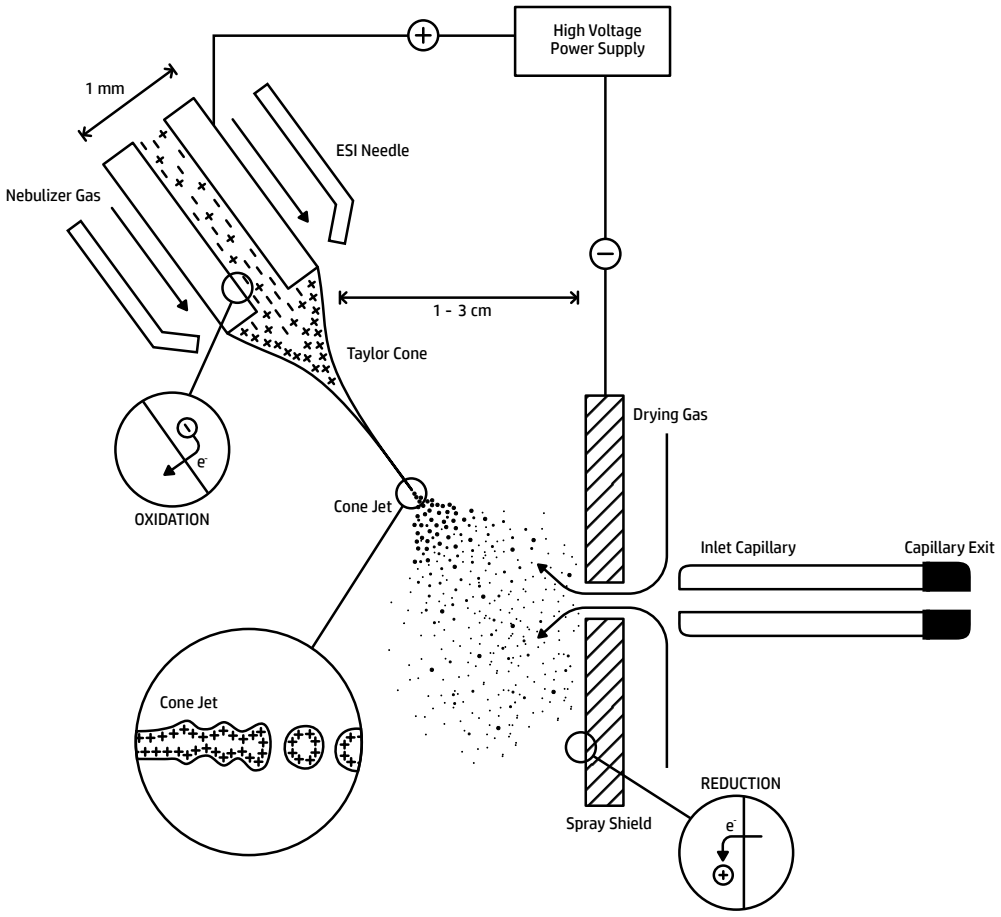

Fig. 1.3: Scheme of a modern electrospray ion source with an additional nebulizer gas flow at the ESI capillary.

tions, the potential around the capillary is calculated, and the electric field is then obtained as the gradient of this potential, evaluated at the capillary surface.

$$E_c = \frac{2V_c}{r_c \ln\left(\frac{4d}{r_c}\right)} . \tag{1.1}$$

Considering the parameters mentioned above, the liquid is exposed to an electrical field of about $1 \cdot 10^6\,\mathrm{V\,m^{-1}}$ at the exit of the spray capillary. It is proportional to the applied voltage V_c and is strongly influenced by the inner diameter of the spray capillary r_c, according to Equation 1.1. The electric field slightly penetrates the liquid, resulting in charge separation [25]. In positive ion mode, negatively charged ions are repelled backward, while positively charged ions are drawn toward the exit of the spray capillary to counteract the electrical field [25]. The accumulation of positively charged ions at the surface of the liquid causes its deformation, forming a liquid cone [25]. Taylor [38] was the first to theoretically describe this cone, which was named after him as the Taylor cone. He examined the conditions required for a stable cone formation [38].

According to this idealized model, the formation of a Taylor cone begins when the spherical liquid surface at the tip of the spray needle stretches into an oval shape as the electric field strength increases. The charge density rises as the oval becomes more curved, causing the field strength to grow even further. Once the electric field reaches a critical level, the electrostatic forces overcome the surface tension, rendering the Taylor cone unstable and initiating the release of a thin, micrometer-thick jet of liquid from its tip toward the counter electrode [41, 38, 25]. In positive mode, the jet carries an excess of positive ions since it originates from the apex of the cone, where charge separation occurs, and the charge density is at its highest [27]. However, the jet becomes unstable after a few $100\,\mu\mathrm{m}$ and quickly breaks into tiny droplets [30]. These droplets, carrying significant excess charge, repel each other due to Coulombic forces, resulting in a fine spray. This operational mode is known as the *cone-jet mode* and is also displayed in Figure 1.3 [16]. At higher electric fields, the single jet will be replaced by multiple jets, releasing droplets. This mode is known as the multijet mode or multi-spray condition [16, 25]. In negative ion mode, all potentials are switched to draw negatively charged ions toward the capillary exit. This leads to an excess of negative charges within the generated droplet plume.

The ion source setup can be seen as an electrodynamic flow cell similar to electrolysis [2, 21, 25]. The conductivity between the spray capillary and counter electrode results from the charge transport of the electrically charged spray [29, 2, 21]. While operating in positive ion mode, the spray needle becomes the anode, where oxidation takes place [21]. This means that anions from the solution are converted into neutral

molecules and electrons, as described in Equation 1.3, which removes the negative counter-ions from positive ions [7]. Alternatively, metal atoms can be converted to positive ions and electrons at the inner wall of the conductive spray needle as displayed in Equation 1.2 [21, 16, 25]. This means that ions that were initially not present are added to the solution [7]. Blades et al. [3] employed a zinc spray capillary and successfully detected Zn^{2+} ions in the mass spectra. Additionally, they identified Fe^{2+} ions when using a stainless steel capillary.

$$\mathrm{M_{(S)}} \longrightarrow \mathrm{M_{aq}^{2+}} + 2\,\mathrm{e^-} \tag{1.2}$$

$$4\,\mathrm{OH_{aq}^-} \longrightarrow \mathrm{O_{2(g)}} + 2\,\mathrm{H_2O} + 4\,\mathrm{e^-} \tag{1.3}$$

At the counter electrode, which serves as the cathode, positively charged droplets that collide with the electrode are reduced and neutralized, mostly yielding Hydrogen [21, 16].

Despite its significant role in modern mass spectrometry, the exact mechanism of electrospray remains not fully understood [25]. It is clear that various parameters influence the initial droplet size [7], but it is typically in the range of a few micrometers [16]. There are several initial droplet sizes reported in the literature, which vary between $4\,\mu\mathrm{m}$ to $100\,\mu\mathrm{m}$ [35, 15, 9, 14, 37, 34, 11]. Each droplet, generated by an ideal cone-jet spray, is assumed to carry about ten thousand charges [16]. Evaporation of solvent molecules from the droplets increases the charge density until it reaches the Rayleigh limit Q_{Ry}, described by

$$Q_{Ry} = 8\pi\sqrt{\epsilon_0 \gamma R^3} \tag{1.4}$$

where ϵ_0 is the electrical permittivity, γ is the surface tension of the solvent, and R is the droplet's radius [33, 7].

The evaporation energy comes from the thermal energy of ambient air [7]. When the Coulomb forces overcome the droplet's surface tension, the droplet is caused to decompose by releasing a jet of smaller progeny droplets [7, 16]. Initially, the decomposition was believed to happen as a so-called Coulomb explosion or Coulomb fission [16]. Further studies report an aerodynamic reason for the droplets to break apart rather than an electrostatic one [26]. Davis [9] and Taflin [37] et al. reported that the generated progeny droplets lead to a mass loss between $2\,\%$ and $5\,\%$.

However, the charge loss of the parent droplet is between $15\,\%$ and $25\,\%$. Grimm et al. [15] report a parent droplet diameter reduction from $27\,\mu\mathrm{m}$ to $5\,\mu\mathrm{m}$ within about $0.22\,\mathrm{s}$. Duft et al. [11] report on a $25\,\mu\mathrm{m}$ droplet which loses about $33\,\%$ of its charge but only $0.3\,\%$ of its mass in about 100 progeny droplets. Parent and progeny droplets further shrink due to solvent evaporation and then eject a second generation of progeny droplets [7].

Considering all this information, one can visualize a large parent droplet, from which a small part splits into multiple progeny droplets at each step. Markert et al. [28] estimated the ion mobilities for typical initial droplets and calculated that a typical initial droplet needs about $0.8\,\mathrm{ms}$ to $1.3\,\mathrm{ms}$ to reach the mass spectrometer's inlet system. The transfer time mostly depends on the droplet's radius and the electrical field. Wang et al. [39] numerically simulated transfer times in nano-ESI. For ions with similar ion mobilities, transfer times were observed in the range of a few milliseconds. This time is much shorter than the reported average droplet lifetimes of about $1\,\mathrm{ms}$ [28] of the initial droplets.

1.3.2 Non-Dissolved Charged Droplets in ESI: A Brief History Lesson

A possible starting point of the development of electrospray ionization — and thus the issue of non-dissolved droplets — was in 1968, when Malcolm Dole described a method of "electrospraying a dilute polymer solution into an evaporation chamber" [10].

The general concept of his work was based on the research of Zeleny [43] and Taylor [38] from 1917 and 1964, respectively. Zeleny experimented with the "instability of electrified liquid surfaces" [43] and discovered that if a sufficiently high level of "electrification" is applied to a liquid surface inside a tube, "the liquid at this place is pulled out into a fine thread, which eventually breaks up into minute drops" [43]. Taylor enhanced Zeleny's research by calculating stability parameters and describing an axial jet that develops at conical points of an unstable drop [38]. These axial jets were later referred to as the "Taylor cone" [16].

From today's perspective, Dole performed a so-called Electrohydrodynamic Ionization (EHI) [16]. He used a low-volatile polystyrene solution and pumped it through a hypodermic needle in an evacuated chamber, interacting with a strong electrostatic field by applying a potential in the order of $40\,\mathrm{kV}$ [10]. The liquid surface at the tip of the needle distorts the meniscus into a sharp cone due to the electrostatic forces [12]. A mist of charged droplets expands at supersonic speeds in a vacuum [16].

In Doles's case, the generated charged droplets contain polystyrene and solvent molecules. The latter begins to evaporate, causing the droplets to shrink and resulting in an increased charge density. Already in 1882, Lord Rayleigh [33] described that droplet shrinkage causes the droplet to overcome the "Rayleigh limit" of stability. It defines the maximum charge a liquid droplet can carry before electrostatic repulsion overcomes surface tension, leading to Coulombic fission. Building on this, Dole presents a working hypothesis that is still found in many textbooks: "By using an electrospray it was thought that the drops on evaporation of the solvent, would become electrically unstable and break down into smaller drops until possibly drops containing only one macromolecule per drop would result."[10]. The disadvantage of Dole's EHI method is that the solvents used must have a very low vapor pressure to prevent too rapid evaporation. However, only a limited number of suitable solvents have this characteristic [13]. This leads to a few application cases and a small number of practitioners of the method.

ESI, as we understand it today, was first described by Yamashita [42], Whitehouse [40], and Fenn [13], who were all colleagues reporting on an instrument that operates based on the same principles as current devices. Like EHI, ESI also generates a mist of electrically charged droplets using the same shrinkage mechanism, but differs in that ESI operates at atmospheric pressure. Fenn et al. employ a syringe pump to inject the analyte-containing solution at a flow rate between 1 and $20\,\mu\mathrm{L\,min^{-1}}$ into a hypodermic needle, the spray capillary [13, 16]. A potential of several kilovolts is applied to the needle relative to the surrounding metal spray chamber, pulling the generated charged droplets into a glass capillary on the opposite wall of the chamber [13]. At that time, Fenn uses a heated countercurrent of nitrogen at a flow rate of approximately $100\,\mathrm{mL\,s^{-1}}$ to prevent the droplets from "freeze-drying" due to evaporative cooling while entering the rough vacuum in an adiabatic expansion [13, 16]. That indicates that they were aware of droplets surviving upon passage through the spray chamber.

Another essential step was adapting this interface for higher liquid flow rates, which occur when a mass spectrometer is connected to liquid chromatography (LC). This adaptation was also achieved in the late '80s by Bruins, Covey, and Henion [5, 8]. They designed a pneumatically assisted ESI interface that is still considered standard in many applications [16]. Flow rates generated by LC conditions would likely result in an unstable spray [8] and, consequently, could lead to unreliable initial droplet formation. A higher liquid flow F_{liquid} results in larger droplet diameters R as indicated by Equation 1.5 [7].

$$R \propto \sqrt[3]{F_{\mathrm{liquid}}} \tag{1.5}$$

For this reason, the new ESI interface differs from Fenn's interface by introducing a concentric flow of gas around the nozzle of the spray capillary [16]. This additional gas flow increases the analyte flow and decreases the surface tension, supporting the spray generation [21]. Rather than liquid flow rates between 1 and $20\,\mu\mathrm{L\,min^{-1}}$, this interface can handle flow rates between 10 and $200\,\mu\mathrm{L\,min^{-1}}$ [16].

Fenn and his group made several improvements since the publication of the original design, which enhanced the robustness of operation, ion transmission, and ion yield [16]. Together with Koichi Tanaka, Fenn was awarded the Nobel Prize in Chemistry in 2002 "for their development of soft desorption ionization methods for mass spectrometric analyses of biological macromolecules" [31].

One of the most significant issues associated with the first on-axis arrangement of the spray capillary and inlet system was the clogging of capillaries and skimmers in the first stages of the MS-vacuum system due to the accumulation of nonvolatile compounds in the analyte-containing solutions, such as buffer salts or organic materials [1]. Therefore, modified designs for ESI sources were developed (shown in Figure 1.4). The simplest method to eliminate unwanted compounds was to arrange the spray capillary off-axis or at an angle to the MS inlet. The idea of such arrangements is that charged droplets bend their trajectory towards the MS inlet due to the electrostatic field. However, in practice, non-charged components can also enter the system due to fluid dynamics caused by the pressure difference between the spray chamber at atmospheric pressure and the first vacuum stage. As illustrated in Figure 1.4, manufacturers have used more complex structures, such as the crossflow or z-spray, introduced by Micromass [1]. Some of these designs are still in use. These advanced designs indicate an awareness of the notion that not only bare ions are generated during the desolvation process. However, almost no publications since Fenn's early concerns about dry-freezing droplets have mentioned aspirated droplets entering the high-vacuum stages of mass spectrometers, even though effects such as "baseline increases" at high *m/z* are widely known in some fields of ESI mass spectrometry. Moreover, contamination of electrode surfaces, which occurs far beyond the desolvation unit (see section 2.3.1), is common and must be handled by technicians worldwide every day.

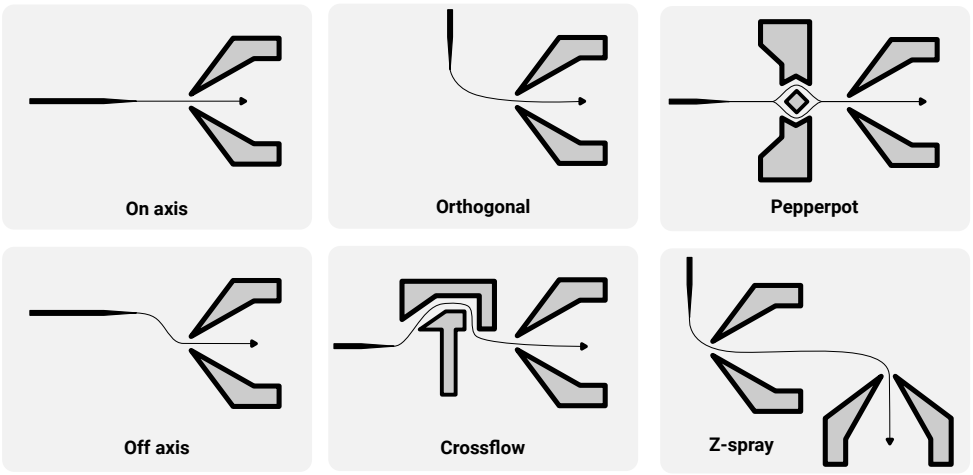

Fig. 1.4: Some common designs of spray chambers to enhance system robustness and reduce droplet-induced issues such as clogged capillaries and skimmers [1].

References

[1] J. Abian. „The coupling of gas and liquid chromatography with mass spectrometry“. In: *Journal of Mass Spectrometry* 34 (3 Mar. 1999), pp. 157–168 (cit. on pp. 13, 14).

[2] Gary J. Van Berkel. „Electrolytic deposition of metals on to the high-voltage contact in an electrospray emitter: implications for gas-phase ion formation“. In: *Journal of Mass Spectrometry* 35 (7 July 2000), pp. 773–783 (cit. on p. 9).

[3] Arthur T. Blades, Michael G. Ikonomou, and Paul. Kebarle. „Mechanism of electrospray mass spectrometry. Electrospray as an electrolysis cell“. In: *Analytical Chemistry* 63 (19 Oct. 1991), pp. 2109–2114 (cit. on p. 10).

[4] Andries P. Bruins. „Mechanistic aspects of electrospray ionization“. In: *Journal of Chromatography A* 794 (1998), pp. 345–357 (cit. on p. 3).

[5] Andries P. Bruins, Thomas R. Covey, and Jack D. Henion. „Ion spray interface for combined liquid chromatography/atmospheric pressure ionization mass spectrometry“. In: *Analytical Chemistry* 59 (22 Nov. 1987), pp. 2642–2646 (cit. on p. 12).

[6] Nadja B. Cech and C. G. Enke. „Practical implications of some recent studies in electrospray ionization fundamentals“. In: *Mass Spectrometry Reviews* 20 (6 2001), pp. 362–387 (cit. on p. 3).

[7] Richard B. Cole. *Electrospray and MALDI Mass Spectrometry*. Ed. by Richard B. Cole. John Wiley & Sons, Inc., Apr. 2010 (cit. on pp. 3, 10–12).

[8] T. R. Covey, A. P. Bruins, and J. D. Henion. „Comparison of thermospray and ion spray mass spectrometry in an atmospheric pressure ion source“. In: *Organic Mass Spectrometry* 23 (3 Mar. 1988), pp. 178–186 (cit. on p. 12).

[9] E. J. Davis and M. A. Bridges. „The rayleigh limit of charge revisited: light scattering from exploding droplets“. In: *Journal of Aerosol Science* 25 (6 Sept. 1994), pp. 1179–1199 (cit. on p. 10).

[10] Malcolm Dole, L. L. Mack, R. L. Hines, et al. „Molecular beams of macroions“. In: *The Journal of Chemical Physics* 49 (5 1968), pp. 2240–2249 (cit. on pp. 11, 12).

[11] Denis Duft, Tobias Achtzehn, Rene Müller, Bernd A. Huber, and Thomas Leisner. „Rayleigh jets from levitated microdroplets“. In: *Nature* 421 (6919 Jan. 2003), pp. 128–128 (cit. on pp. 10, 11).

[12] C. A. Evans and C. D. Hendricks. „An Electrohydrodynamic Ion Source for the Mass Spectrometry of Liquids“. In: *Review of Scientific Instruments* 43 (10 Oct. 1972), pp. 1527–1530 (cit. on p. 11).

[13] John B. Fenn, Matthias Mann, Chin Kai Meng, Shek Fu Wong, and Craig M. Whitehouse. „Electrospray Ionization for Mass Spectrometry of Large Biomolecules“. In: *Science* 246.4926 (1989), pp. 64–71. eprint: `https://www.science.org/doi/pdf/10.1126/science.2675315` (cit. on p. 12).

[14] Alessandro Gomez and Keqi Tang. „Charge and fission of droplets in electrostatic sprays“. In: *Physics of Fluids* 6 (1 1994), pp. 404–414 (cit. on p. 10).

[15] Ronald L. Grimm and J. L. Beauchamp. „Evaporation and discharge dynamics of highly charged droplets of heptane, octane, and p-xylene generated by electrospray ionization“. In: *Analytical Chemistry* 74 (24 Dec. 2002), pp. 6291–6297 (cit. on pp. 10, 11).

[16] Jürgen H. Gross. *Mass Spectrometry*. Springer International Publishing, 2017 (cit. on pp. 3, 7, 9–13).

[17] Chris Heintz, Hendrik Kersten, Thorsten Benter, and Walter Wißdorf. „Signatures of Charged Droplets from ESI: A Statistical Analysis of Non-summed Mass Spectra Compared to APCI“. In: *Journal of the American Society for Mass Spectrometry* 36 (4 Apr. 2025), pp. 839–849 (cit. on p. 3).

[18] Chris Heintz, Lisa Schnödewind, Oliver Braubach, et al. „Influence of polarity mode switching and standby times on signal stability and detection of aspirated droplet signatures in electrospray mass spectrometry“. In: *International Journal of Mass Spectrometry* 499 (May 2024), p. 117232 (cit. on p. 3).

[19] Chris Heintz, Lisa Schnödewind, Oliver Braubach, et al. „Observation of Large, Charged Droplet Signatures within the High-Vacuum Region of a Commercial Electrospray TOF-MS“. In: *Journal of the American Society for Mass Spectrometry* (Feb. 2024) (cit. on p. 3).

[20] Edmond de Hoffmann and Vincent Strootbant. *Mass Spectrometry: Principles and Applications*. 3rd ed. John Wiley & Sons, 2007 (cit. on p. 3).

[21] Michael G. Ikonomou, Arthur T. Blades, and Paul. Kebarle. „Electrospray-ion spray: a comparison of mechanisms and performance“. In: *Analytical Chemistry* 63 (18 Sept. 1991), pp. 1989–1998 (cit. on pp. 9, 10, 13).

[22] Patricia Itzenhäuser, Ferdinand Max Wachter, Laura Lehmann, et al. „Dynamics of the Aspiration of Charged Droplets into a LC-ESI-MS System“. In: *Journal of the American Society for Mass Spectrometry* (Sept. 2024) (cit. on pp. 3, 5).

[23] Yang Kang, Bradley B. Schneider, and Thomas R. Covey. „On the Nature of Mass Spectrometer Analyzer Contamination“. In: *Journal of the American Society for Mass Spectrometry* 28 (11 Nov. 2017), pp. 2384–2392 (cit. on p. 3).

[24] P. Kebarle and M. Peschke. „On the mechanisms by which the charged droplets produced by electrospray lead to gas phase ions“. In: *Analytica Chimica Acta* 406 (2000), pp. 11–35 (cit. on p. 3).

[25] Paul Kebarle and Liang Tang. „From ions in solution to ions in the gas phase - the mechanism of electrospray mass spectrometry“. In: *Analytical Chemistry* 65.22 (1993). PMID: 22881012, 972A–986A (cit. on pp. 3, 7, 9, 10).

[26] Sarah R. Mabbett, Lloyd W. Zilch, Joshua T. Maze, John W. Smith, and Martin F. Jarrold. „Pulsed Acceleration Charge Detection Mass Spectrometry: Application to Weighing Electrosprayed Droplets“. In: *Analytical Chemistry* 79 (22 Nov. 2007), pp. 8431–8439 (cit. on p. 10).

[27] Ioan Marginean, Peter Nemes, Lida Parvin, and Akos Vertes. „How much charge is there on a pulsating Taylor cone?“ In: *Applied Physics Letters* 89 (6 Aug. 2006) (cit. on p. 9).

[28] Clara Markert, Marco Thinius, Laura Lehmann, et al. „Observation of charged droplets from electrospray ionization (ESI) plumes in API mass spectrometers“. In: *Analytical and Bioanalytical Chemistry* 413 (22 Sept. 2021), pp. 5587–5600 (cit. on pp. 3–5, 11).

[29] Juan Fernandez de la Mora, Gary J. Van Berkel, Christie G. Enke, et al. „Electrochemical processes in electrospray ionization mass spectrometry“. In: *Journal of Mass Spectrometry* 35 (8 Aug. 2000), pp. 939–952 (cit. on p. 9).

[30] Peter Nemes, Ioan Marginean, and Akos Vertes. „Spraying Mode Effect on Droplet Formation and Ion Chemistry in Electrosprays“. In: *Analytical Chemistry* 79 (8 Apr. 2007), pp. 3105–3116 (cit. on p. 9).

[31] Nobel Prize Outreach. *The Nobel Prize in Chemistry 2002*. Accessed 29 Jan. 2025. 2025 (cit. on p. 13).

[32] Michelle Rajkovic, Thorsten Benter, and Walter Wißdorf. „Investigation of Surface-Induced Dissociation Processes via Molecular Dynamics Simulations of Wall Collisions of Large Droplets Produced by Electrospray Ionization“. In: *Journal of the American Society for Mass Spectrometry* 36 (4 Apr. 2025), pp. 760–770 (cit. on pp. 3, 5).

[33] Lord Rayleigh. „XX. On the equilibrium of liquid conducting masses charged with electricity“. In: *The London, Edinburgh, and Dublin Philosophical Magazine and Journal of Science* 14 (87 Sept. 1882), pp. 184–186 (cit. on pp. 10, 12).

[34] John W. Schweizer and D. N. Hanson. „Stability limit of charged drops“. In: *Journal of Colloid and Interface Science* 35 (3 Mar. 1971), pp. 417–423 (cit. on p. 10).

[35] James N. Smith, Richard C. Flagan, and J. L. Beauchamp. „Droplet evaporation and discharge dynamics in electrospray ionization“. In: *Journal of Physical Chemistry A* 106 (42 Oct. 2002), pp. 9957–9967 (cit. on p. 10).

[36] William R. Smythe. *Static and Dynamic Electricity*. 3rd. New York: McGraw-Hill, 1968 (cit. on p. 7).

[37] Daniel C. Taflin, Timothy L. Ward, and E. James Davis. „Electrified droplet fission and the Rayleigh limit“. In: *Langmuir* 5.2 (1989), pp. 376–384 (cit. on p. 10).

[38] Geoffrey Ingram Taylor. „Disintegration of water drops in an electric field“. In: *Proceedings of the Royal Society of London. Series A. Mathematical and Physical Sciences* 280 (1382 July 1964), pp. 383–397 (cit. on pp. 9, 11).

[39] Wei Wang, Steve Bajic, Benzi John, and David R. Emerson. „Numerical Simulation of Ion Transport in a Nano-Electrospray Ion Source at Atmospheric Pressure“. In: *Journal of the American Society for Mass Spectrometry* 29 (3 Mar. 2018), pp. 600–612 (cit. on p. 11).

[40] Craig M. Whitehouse, Robert N. Dreyer, Masamichi. Yamashita, and John B. Fenn. „Electrospray interface for liquid chromatographs and mass spectrometers“. In: *Analytical Chemistry* 57 (3 Mar. 1985), pp. 675–679 (cit. on p. 12).

[41] Matthias S. Wilm and Matthias Mann. „Electrospray and Taylor-Cone theory, Dole's beam of macromolecules at last?“ In: *International Journal of Mass Spectrometry and Ion Processes* 136 (2-3 Sept. 1994), pp. 167–180 (cit. on p. 9).

[42] Masamichi Yamashita and John B. Fenn. „Electrospray ion source. Another variation on the free-jet theme“. In: *The Journal of Physical Chemistry* 88 (20 Sept. 1984), pp. 4451–4459 (cit. on p. 12).

[43] John Zeleny. „Instability of Electrified Liquid Surfaces“. In: *Physical Review* 10 (1 July 1917), pp. 1–6 (cit. on p. 11).

2 Bruker micrOTOF and Experimental Setup

2.1 Configuration Bruker MicrOTOF

All experiments were conducted using a customized Bruker micrOTOF 1.0 (Bruker Corporation, Bremen, Germany). The general configuration of the instrument is illustrated in Figure 2.1. The electrospray is generated in the source chamber, which is depicted in more detail in Figure 2.2.

Ions and charged droplets generated from the electrospray pass through an inlet capillary into the first vacuum stage. The inlet capillary is typically made of glass or lead glass, which provides higher electrical conductivity in the glass material. The first (rough) vacuum stage is pumped to approximately $4\,\mathrm{mbar}$ [2]. Upon leaving the capillary exit, the ions are guided through a first skimmer into the second vacuum stage and the first of two RF-only hexapoles, known as the "pre-hexapole" [2]. The second vacuum stage operates at a pressure of around $0.5\,\mathrm{mbar}$ [2]. Matrix gases are further evacuated. The third vacuum stage is similar to the second but operates at an even lower pressure of about $5 \cdot 10^{-4}\,\mathrm{mbar}$. Ions pass through a second skimmer and are guided into the second RF-only hexapole, referred to as the "main-hexapole" [2]. Both hexapoles are held at a suitable offset voltage to create a dragging force for the ion transport along the transfer system. The main-hexapole focuses the ion beam, guiding it into a stack of focusing lenses.

The ion beam then enters the orthogonal acceleration stage (oa-stage) of the time-of-flight tube. A set of electrostatic lenses divides the ion beam into packets, which are pushed into the tube toward the reflector and eventually the TOF detector.

The instrument can operate in negative and positive ion modes by inverting all polarities at the electrostatic lenses.

The Bruker micrOTOF has several advantages for observing droplets or droplet debris. First, the instrument control software, "micrOTOFcontrol", provides a service mode that enables access to many critical instrument parameters, such as digitizer settings and potentials of electrostatic lenses. Second, the instrument is treated as

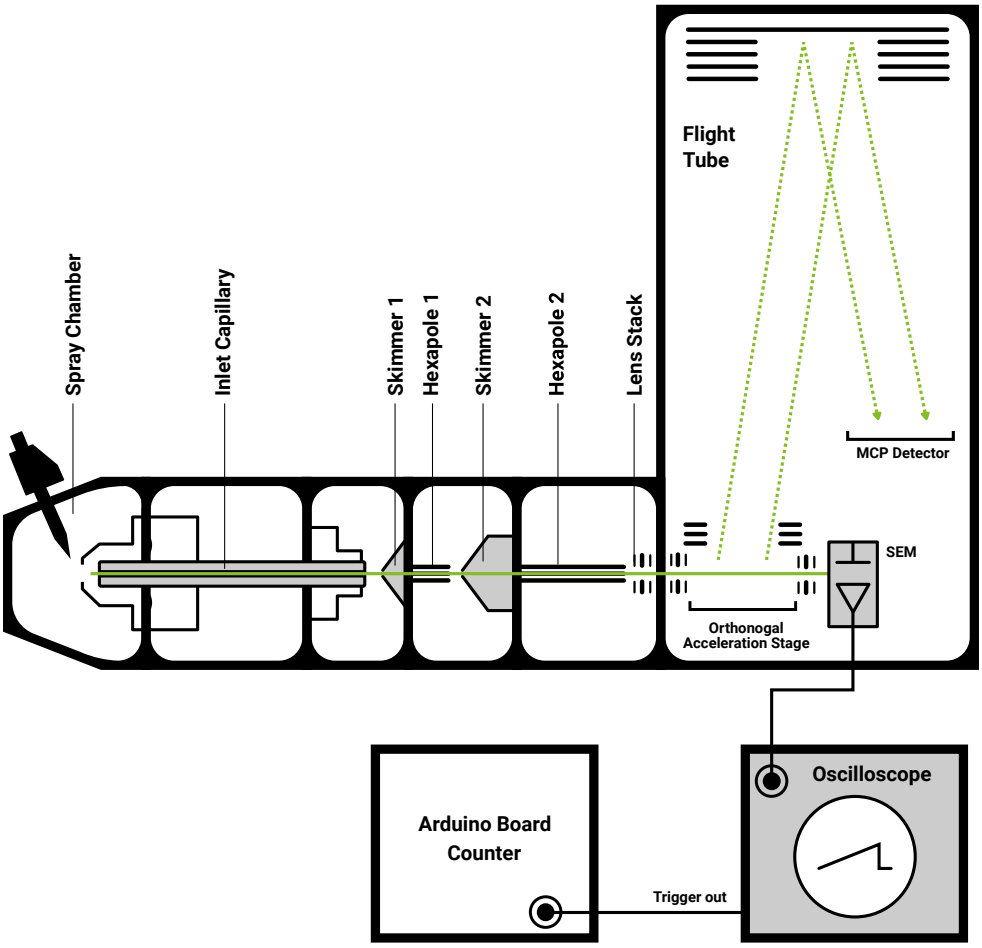

Fig. 2.1: Simplified scheme of the Bruker micrOTOF.

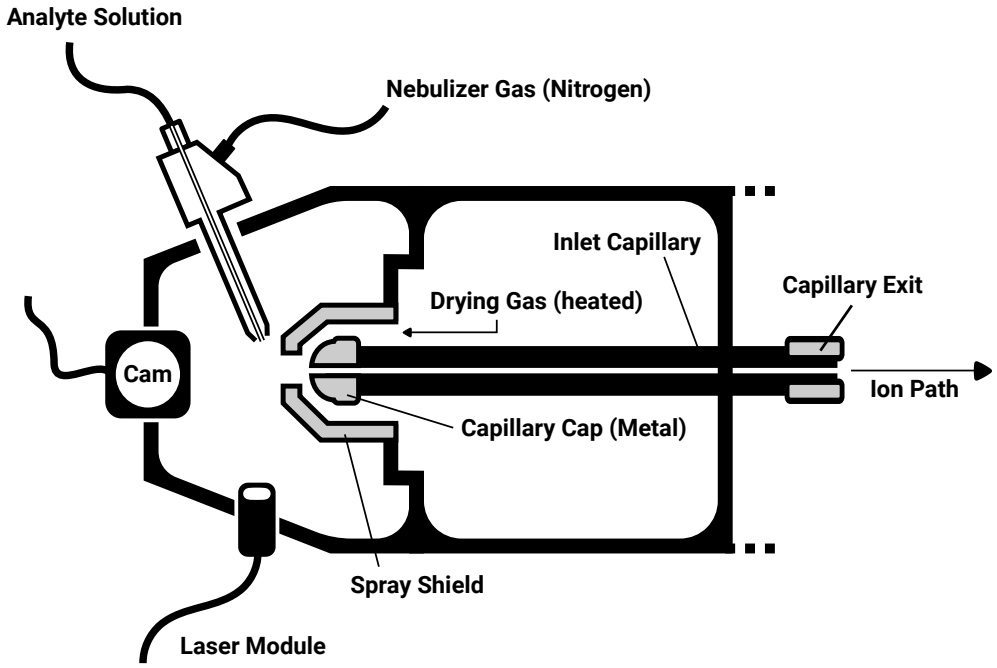

Fig. 2.2: Detailed scheme of the ion source and transfer stage front-end.

a purely fundamental research instrument. This means outer covers are removed and most instrument areas are accessible through maintenance hatches. This allows external devices and electronics to be connected to the components of the micrOTOF. The third advantage is the existence of an auxiliary detector downstream of the oa-stage, which is a secondary electron multiplier (SEM). Its primary use is to monitor the ion beam for correct alignment within the oa-stage. The SEM was disconnected from an internal electrometer and connected to an oscilloscope, enabling the direct observation of the time-resolved ion current.

2.2 Atmospheric Pressure Ionization Interfaces

2.2.1 ESI-Source

The standard Bruker Apollo ESI source was used for most experiments. A scheme of the ion source is shown in Figure 2.2. The Apollo source operates according to the same principles outlined in section 1.3.1 and further illustrated in Figure 1.3. In the present case, the nebulizer and drying gas consisted of nitrogen. The temperature of the drying gas and all gas flows are detailed in section 2.9.

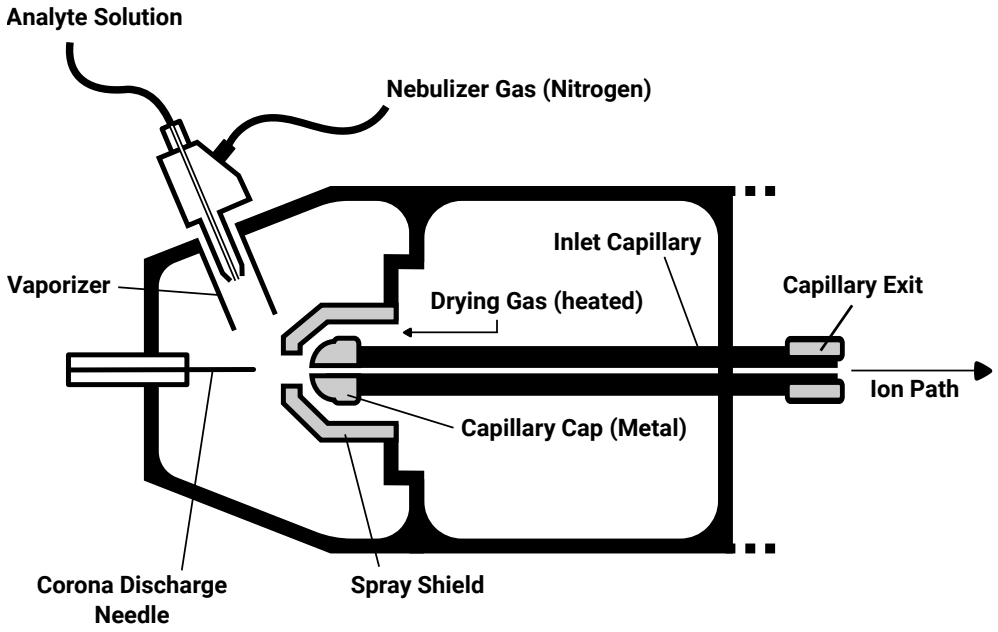

Fig. 2.3: Schematic of the Bruker ion source in APCI configuration.

The ion source was adjusted for some experiments as shown in Figure 2.2. A series of experiments focused on the spray's appearance, for which a camera was installed inside the chamber to observe the spray's behavior under various conditions. The spray was illuminated by a laser module positioned beneath the source chamber. The light was directed through a small opening typically used for exhaust gases to leave. The laser beam passed through a cylindrical glass lens to spread the beam and illuminate the entire spray cross-section.

2.2.2 APCI-Source

In this work, other ionization methods in addition to ESI were employed. In atmospheric pressure chemical ionization (APCI), a corona discharge is used to ionize a reagent gas, which in turn ionizes the vaporized analyte through gas-phase reactions [5]. The nebulization process in the APCI source is similar to that of the ESI source. However, the solution is sprayed into a vaporizer tube with temperatures ranging from $250\,^{\circ}\mathrm{C}$ to $400\,^{\circ}\mathrm{C}$, as shown in Figure 2.3 [2]. Despite the required vaporization, the heat can damage thermolabile analytes and degrade biomolecules, such as proteins and peptides. Upon exiting the vaporizer tube, solvent molecules are ionized by a current-regulated discharge from a corona needle [2]. Typically, the corona needle operates at a voltage between $1\,\mathrm{kV}$ to $4\,\mathrm{kV}$ [2]. The generated primary ions transfer their charge to the analyte molecules via chemical reactions. Similar to ESI, APCI utilizes a heated counterflow of nitrogen gas.

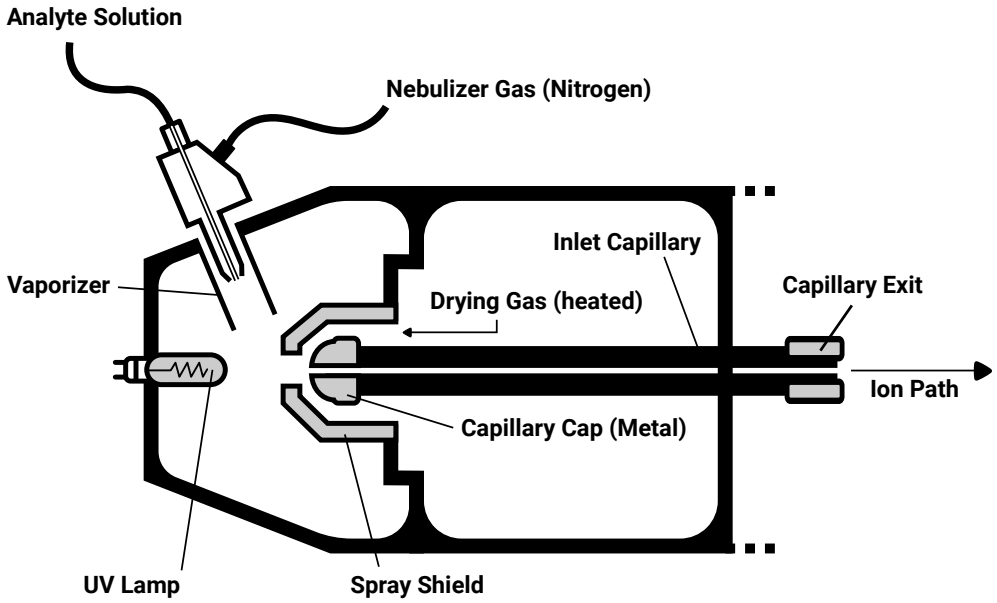

Fig. 2.4: Schematic of the Bruker ion source in APPI configuration.

APCI is particularly effective for liquid chromatography-mass spectrometry (LC-MS) applications of less polar compounds, which are present in neutral form in the liquid, offering high sensitivity and minimal fragmentation for low to medium molecular weight analytes [5].

2.2.3 APPI-Source

Atmospheric pressure photoionization (APPI) is a technique similar to ESI and APCI that uses ultraviolet (UV) photons to ionize analyte molecules in the gas phase.

The APPI source illustrated in Figure 2.4 is primarily utilized when the analyte is not effectively ionized by either ESI or APCI [2]. The underlying mechanism is similar to that of APCI. However, the vaporized solvent molecules are ionized not by a corona discharge but by a UV lamp. High-energy radiation primarily ionizes solvent molecules, transferring their charge to the analyte molecules, transforming them into sample ions [2].

This mechanism enables efficient ionization of nonpolar and moderately polar compounds, especially those not readily ionized by electrospray ionization (ESI) or APCI.

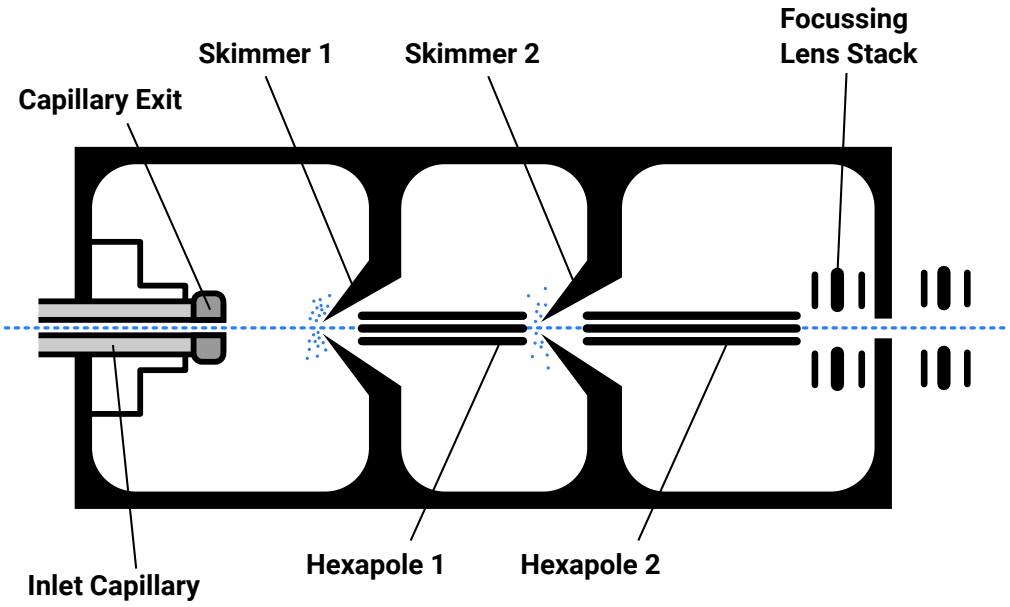

Fig. 2.5: Schematic of the transfer optics in the Bruker micrOTOF

2.3 Transfer Unit

2.3.1 Desolvation Unit

The so-called *desolvation unit* contains primarily the glass inlet capillary, which transfers ions from the ionization chamber to the first vacuum stage. The capillary tip at the front is covered with a metal cap and encircled by a metal spray shield, which acts as the counter electrode to the ESI spray needle. The drying gas heater is an integral part of the desolvation unit. As described in section 1.3.1, the heated dry gas flow is directed towards the solvent stream from the spray needle. It also heats the front section of the inlet capillary to prevent condensation and clogging. The end of the inlet capillary is also covered in metal so that a potential difference of a few thousand volts can be applied between the capillary entrance and exit. However, the pressure difference is the primary cause that draws the ion flux into the first vacuum stage [2].

2.3.2 Ion Transmission Module

After leaving the inlet capillary, the ions enter the first of three vacuum stages in the so-called ion transmission module. All vacuum stages are separated by skimmers,

consisting of a metal cone with an orifice that is small enough to act as a flow restriction. This allows the pressure differences between the stages to be maintained, yet is large enough to permit the ions to pass. The first vacuum stage operates at a pressure of about $4\,\mathrm{mbar}$ and is connected to a rough pump [2]. The metal-covered capillary exit has a potential of about $200\,\mathrm{V}$. In conjunction with the inner diameter of the capillary and the grounded first skimmer, the gas flow, containing the analyte ions, transitions from a steady stream to a subsonic jet [2]. In addition to the potential differences, the ions' motion is also governed by the flow of the neutral background gas through the pressure stages. Stray ions will not pass the skimmers and will therefore not enter the second or third vacuum stage. After passing through the first skimmer, the ions will enter the first of two hexapoles, followed by a second skimmer and the second hexapole. Before entering the orthogonal acceleration stage, a stack of lenses further focuses the ion beam.

2.4 Orthonogal Acceleration Stage

The orthogonal acceleration stage (oa-stage) deflects and transfers incoming ions from the transfer unit into the time-of-flight mass analyzer. The oa-stage comprises a system of stacked electrodes. It includes one base electrode and six round-shaped electrode plates with slits in the center. It was shown [9] that stepwise acceleration using two or more lens stacks enhances the extraction and quality of the ion beam, which is implemented in the Bruker instrument. The deflection process can be divided into three steps:

1. The ion beam from the ion transfer system fills the oa-stage and is guided straight ahead through the oa-stage while the acceleration electrodes remain at ground potential (pulser off time). The ion beam impacts the opposite side, striking the conversion dynode of the auxiliary secondary electron multiplier (SEM) [2]. The SEM serves only as an auxiliary detector for monitoring ions, such as troubleshooting or tuning, and is not involved in the recording of mass spectra [2]. Hence, all ions that hit the dynode are lost for mass analysis.

2. When a suitable acceleration potential is applied to the ground electrode, a packet from the ion beam is forced through the slots in the lens stack toward the TOF analyzer flight tube [2].

3. The push creates a blank region in the ion beam, which is observable when recording the ion current hitting the SEM. After returning all electrodes to ground potential, the ion beam refills the oa-stage.

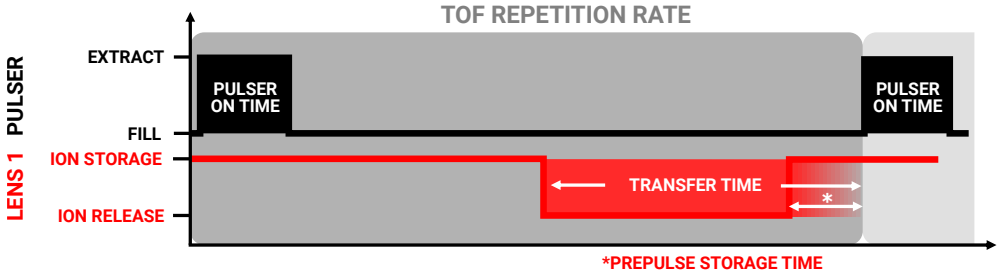

Fig. 2.6: Timing diagram in the orthogonal acceleration stage illustrates the pulser's on and off time with the black graph, while the red plot depicts the ion storage and release applied by lens 1 (see Figure 2.7). The transfer and prepulse storage times can be manually set in the instrument's software, and the high-mass cut-off can be defined.

This process of filling, cut-off, acceleration, and re-filling can be repeated with a frequency of $20\,\mathrm{kHz}$, which is referred to as the *TOF repetition rate* [2]. Figure 2.6 provides an overview of the detailed relationship between the TOF repetition rate and the parameters of ion storage and ion transfer time, leading to ion extraction. Figure 2.7 illustrates details of the lens arrangement within the oa-stage.

The transfer time in Figure 2.6 is related to lens 1 in Figure 2.7: Lens 1 allows ions to enter the oa-stage only during the transfer time. The longer the transfer time, the higher the upper limit of the transferred m/z. This is due to the slower movement of particles with higher m/z. Hence, they need a certain time to enter the oa-stage before lens 1 closes. A short transfer time will exclude particles with higher masses. Therefore, the transfer time limits the high mass and acts as a high-mass filter. Adjusting the time between the transfer time and the pulse-on time can lower the mass limit. This delay is referred to as the prepulse storage time. If this time is set correctly, particles with lower m/z and higher velocities will have crossed the oa-stage before the push. Considering this, a lower TOF repetition rate allows for longer transfer times and thus enables the analysis of higher m/z values. Conversely, higher TOF repetition rates diminish the possible m/z window.

2.5 time-of-flight Analyzer

The time-of-flight analyzer (TOF) determines the mass-to-charge ratio (m/z) of incoming ions. As the name suggests, these analyzers measure the time required for ions with different m/z to pass a field-free drift tube of known length. The time is measured with great accuracy between the acceleration in the oa-stage and the ion's impact on the detector unit. A fundamental requirement for this is a small

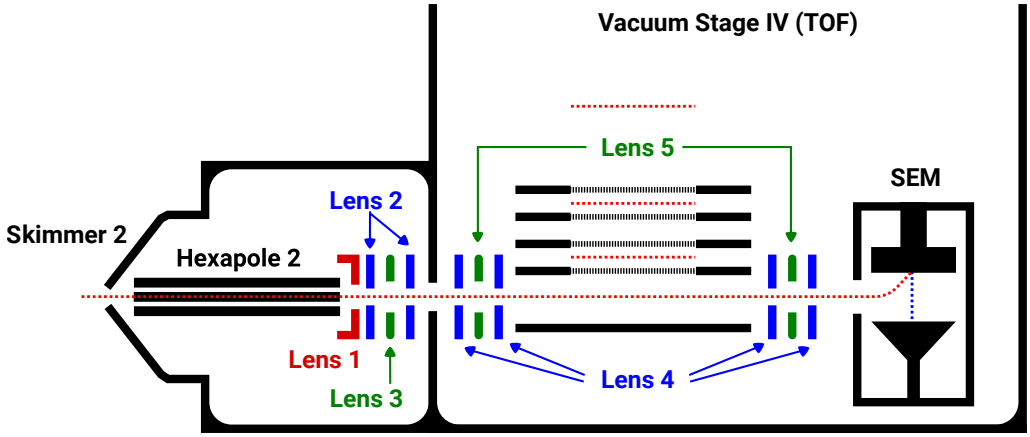

Fig. 2.7: Scheme of the Bruker micrOTOF's orthogonal acceleration stage.

kinetic energy spread ΔE_{kin} between the ions compared to the total kinetic energy, $\Delta E_{kin} << E_{kin}$, allowing the particles to be considered essentially monoenergetic in the direction of the flight tube (y-axis). The kinetic energy in the direction of the focused ion beam before acceleration into the flight tube (toward the SEM) is unaffected by the oa-stage. The kinetic energy of a classical (non-relativistic) particle is:

$$E_{kin} = \frac{1}{2}mv^2 \tag{2.1}$$

If the equation is rearranged to solve for the velocity v, the result is:

$$v = \sqrt{\frac{2E_{kin}}{m}} \tag{2.2}$$

As Equation 2.2 shows, ions with higher mass m have a lower velocity. Consequently, lighter ions will reach the detector in less time than the heavier ones. Theoretically, the m/z range of TOF instruments is unlimited. In practice, the upper limit is determined by the repetition rate. The ions must arrive at the detector before the next batch of ions is introduced into the drift tube within a defined time frame. As mentioned in section 2.4, the repetition rate of the Bruker micrOTOF is around $20\,\mathrm{kHz}$.

The kinetic energy in Equation 2.2 is gained from an electric acceleration E_{el}, which is the product of the acceleration voltage U and the electric charge q. The charge can be expressed as the product of z and the elementary charge e, resulting in $q = ze$. Therefore,

$$E_{el} = qU = zeU = E_{kin} \tag{2.3}$$

which results in

$$v = \sqrt{\frac{2zeU}{m}} \tag{2.4}$$

for the ion's velocity based on its charge and mass. Ions with the same kinetic energy but different masses or charges might have different velocities. Since velocity is the quotient of distance s and time t, Equation 2.3 can be rewritten as

$$t = \frac{s}{\sqrt{\frac{2zeU}{m}}} \tag{2.5}$$

for the flight time through a field-free space. To calculate the *m/z* ratio, Equation 2.5 can be rearranged to

$$\frac{m}{z} = \frac{2eUt^2}{s^2}\,. \tag{2.6}$$

Equation 2.5 shows a proportionality between time and the square root of *m/z*, resulting in the time difference Δt to decrease with a given $\Delta(m/z)$ for increasing *m/z* [6]. The measurement of these small time intervals necessitates fast electronic components [4].

A longer flight path increases the temporal dispersion, as seen in Equation 2.5. For this reason, the Bruker micrOTOF and many other TOF mass spectrometers utilize a reflector acting as an ion mirror, effectively doubling the flight path. This reflector is located on the opposite side of the oa-stage and consists of a set of ring-shaped electrodes with increasing potential, creating a retarding electrical field. The reflection voltage U_r is usually set to about 1.05 to 1.10 times the acceleration voltage U [5]. The accelerated ions enter the retarding electrical field until their kinetic energy reaches zero. At this point, they are reflected, leaving the reflector with the same kinetic energy as when they entered. In addition to the longer flight path, the reflector provides another significant advantage over linear TOF instruments. When two ions of the same *m/z* but with slightly different initial kinetic energy enter the reflector, the more energetic ion penetrates further into the retarding field, allowing the reflector to normalize minor initial differences in kinetic energy [2]. Furthermore, the reflector slightly focuses the ions and corrects minor deviations in the spatial distribution, ultimately enhancing the instrument's resolution and extending the flight path without additional costs [5, 2].

The *duty cycle* refers to the efficiency of the fraction of available ions entering the instrument used for mass analysis. Scanning devices such as quadrupole analyzers exhibit intrinsically low duty cycles of approximately $1 \cdot 10^{-3}\,\%$, allowing only ions with a specific *m/z* to pass. In contrast, others are filtered out and thus unavailable for mass analysis [5]. The duty cycle of TOF instruments is optimized when the ion's time-of-flight through the drift tube is slightly longer than the time required for incoming ions to refill the oa-stage. Orthogonal TOF instruments can achieve a duty cycle of around $3\,\%$ to $30\,\%$ [5], resulting in $2 \cdot 10^4$ spectra per second [2]. The collected *single spectra* resulting from individual "pushes" into the flight tube are summed during the acquisition process and subsequently transmitted to the

data acquisition computer to reduce data volume and enhance the signal-to-noise ratio. For instance, if the operator adjusts the *recording frequency* to $0.5\,\mathrm{Hz}$, a total of $4 \cdot 10^4$ single spectra are combined, providing the operator with one combined spectrum every two seconds. The Bruker micrOTOF allows for manual adjustment of the single-spectrum summation, which occurs in specialized electronic components of the instrument (transient recorder). The minimum number of summed spectra is 2, resulting in a recording frequency of $4 \cdot 10^4\,\mathrm{Hz}$. Nevertheless, the electronics of the instrument are limited to effective recording frequencies of about $25\,\mathrm{Hz}$. As a result, the acquisition process only transmits approximately $0.1\,\%$ of the total number of single spectra to the computer.

The reflected ions will eventually strike the detector, which is a multi-channel plate detector (MCP) in the micrOTOF.

2.6 Detectors

The primary function of a detector is to convert the rate of ions reaching the detector into an electrical signal. The micrOTOF is equipped with a built-in auxiliary detector located downstream of the oa-stage, as well as a main detector positioned at the end of the drift tube. The auxiliary detector is a secondary electron multiplier dynode (SEM), which can monitor the ion beam for tuning issues and troubleshooting [2]. The main detector is a multi-channel plate detector (MCP).

2.6.1 Secondary Electron Multiplier Dynode (SEM)

When energetic particles such as fast ions strike the surface of a metal or semi-conductive material, secondary electrons are emitted from that surface [5]. The number of emitted electrons depends on two factors: First, the energy of the impacting particle; faster particles generate more secondary electrons [8]. Secondly, surface material with a low electron work function will release more electrons. The current induced by the emitted secondary electrons directly is generally too small to be effortlessly detected, as it is in the picoampere range [1]. Therefore, ion detectors commonly employ a physical amplification method: the initially generated electrons are accelerated towards an electrode, known as a *dynode*, with a strong dragging electric field opposite the emission location. Each electron that hits this electrode causes the emission of new secondary electrons. Repeating this process 12-18 times with a stacked array of dynodes, each with a potential difference of $100\,\mathrm{V}$ [5], produces an avalanche of electrons large enough to be easily detected. The first emitted secondary electrons from the impact of ions are thus multiplied, which is why such a detector is called a *secondary electron multiplier* (SEM) [1]. Finally,

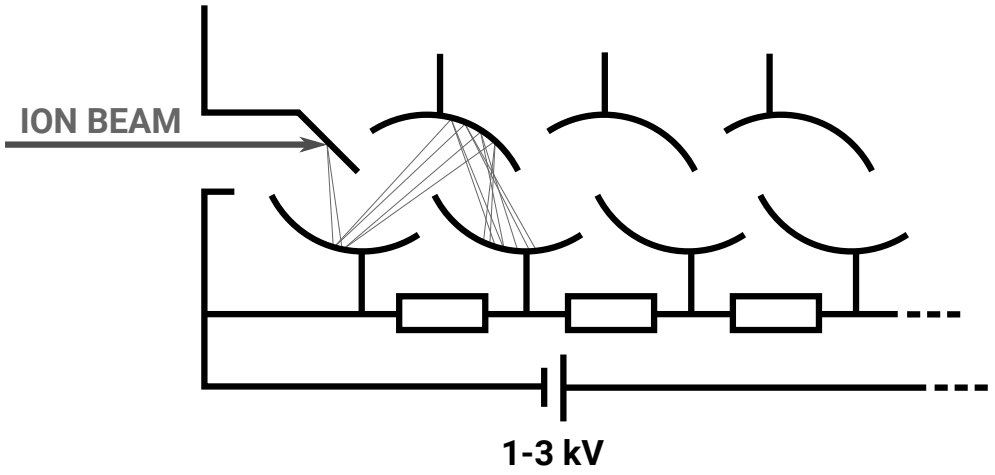

Fig. 2.8: Schematic of a secondary electron multiplier.

the output current can be converted to a voltage, which can then be converted to a digital signal by an analog-to-digital converter (ADC) [5]. Figure 2.8 shows a schematic of a SEM.

2.6.2 Multi-Channel-Plate Detector (MCP)

A channel electron multiplier (CEM), often referred to as a channeltron, operates on the same principle as a secondary electron multiplier (SEM), except that the multiplication of secondary electrons occurs within a continuous tube rather than a stack of discrete dynodes. The tube is composed of a semi-conductive material that can withstand a high voltage of approximately $2\,\mathrm{kV}$. Due to the comparably low conductivity of the material, the high voltage drops from the ion entrance to the tube's exit. Ions entering the tube collide with the inner wall, resulting in the emission of secondary electrons. These secondary electrons then collide with the wall until a measurable current is produced at the end of the tube.

A micro-channel plate detector (MCP) operates on a microscopic scale using the same mechanism. Millions of micrometer-sized holes are distributed on a round plate with diameters ranging from $2\,\mathrm{cm}$ to $5\,\mathrm{cm}$. MCPs are often tilted at a slight angle relative to the orthogonal alignment to prevent direct trajectories of incoming ions from reaching the bottom of the channels. Since the gain of a single plate is much lower (on the order of $1 \cdot 10^3$) than that of an SEM or CEM, two or even three MCPs are typically stacked together to achieve greater signal amplification [10].

2.6.3 Transient Recorder

The transient recorder of the Bruker micrOTOF is a key component for digitizing and transmitting the analog signals generated by the MCP detector. The recorder is often referred to as *digitizer*, emphasizing its role as an analog-to-digital converter with high time accuracy. The recorded transients are the basis for the later time-of-flight-based mass determination.

The transient recorder is a PCI expansion card installed in the instrument's control computer. This physical integration enables direct communication with the control software, which manages the real-time data recording and analysis. All incoming and outgoing connections from the transient recorder are displayed in Figure 2.9. The following section 2.7 describes how the communication between the digitizer and the instrument works.

2.7 Electronic Communication

To customize the Bruker micrOTOF, a basic understanding of the instrument's electronic communication is essential. First, section 2.7.1 provides insights into how the mass spectrometer communicates with the controlling computer. Second, section 2.7.2 explains how these communication paths were utilized and modified to perform the experiments.

2.7.1 Internal Communication micrOTOF

Figure 2.9 illustrates the signal connections between the micrOTOF and the controlling computer. Understanding the communication between the transient recorder card and the actual instrument is crucial for implementing the uncommon instrument operation mode required for the experiments described in this work. Therefore, the exact timing of the trigger signals between the transient recorder card and the instrument was investigated.

The oscillogram in Figure 2.10 displays the connections labeled I (green trace) and II (yellow trace) in Figure 2.9. Connection I is labeled "Trigger In" at the TOF instrument, and Connection II is labeled "Trigger Out." The signal received from the SEM, shown as a blue trace, indicates the activation and deactivation of the pusher. The Trigger In signal (I) occurs slightly before the Trigger Out signal (II). Since signal I originates from the computer, it appears that the PC's transient recorder card provides the initial trigger to commence the measurement cycle with a $5\,\mu$s

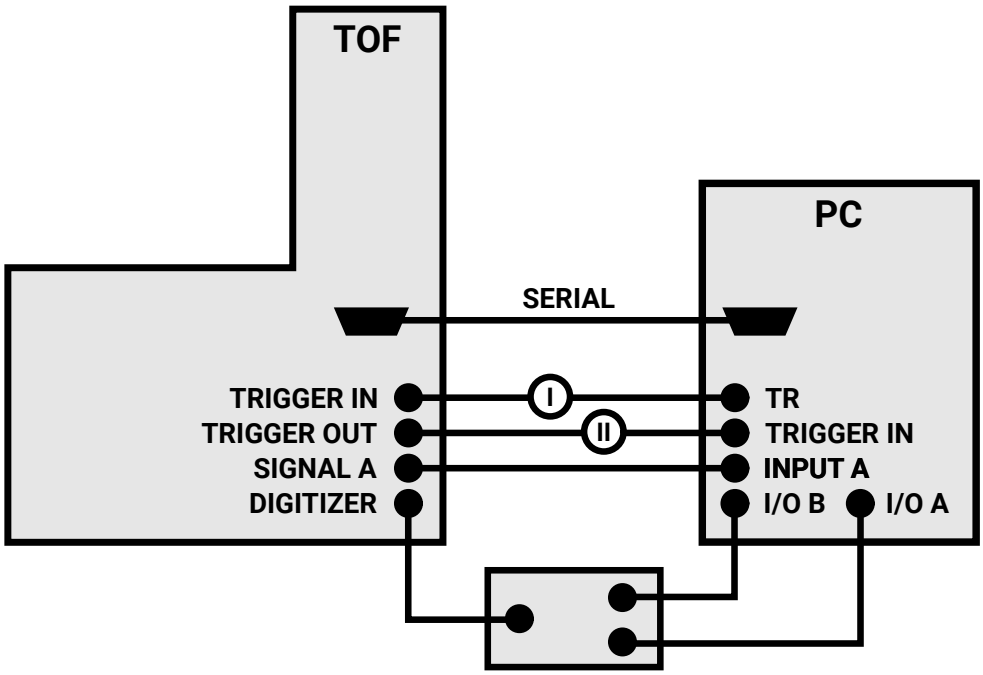

Fig. 2.9: Overview drawing of the cable connections between micrOTOF and computer

pulse. Trigger Out (II) responds to the initial trigger with a $200\,\mathrm{ns}$ signal, which subsequently activates the pusher on the falling slope of the trigger pulse. After $5\,\mu\mathrm{s}$, the initial signal from I terminates, leading to the deactivation of the pusher. The information about the signals was used to attempt the introduction of an external pusher trigger (see section 2.12).

In addition to the trigger signal connections between the computer and the transient recorder card, the instrument communicates with the computer via a serial interface. The transferred data was monitored on the control computer by rerouting the traffic through virtual serial ports. The data traffic was redirected and split into two virtual serial ports using the Null-modem emulator com0com [3]. The exit of the first virtual port served as an interface for the acquisition software, and the other virtual port was utilized to monitor the data traffic. Direct monitoring of the data traffic on the original serial port was not feasible since the acquisition software could not operate in this scenario.

2.7.2 Intercepting and Adjusting the Electronic Traffic

Listening to serial communications allows for the control of external processes when a specific activity of the TOF instrument occurs. For instance, when a data acquisition method is executed, the computer informs the TOF instrument when a particular parameter (e.g., capillary voltage, switching polarity) needs to be changed. It is also

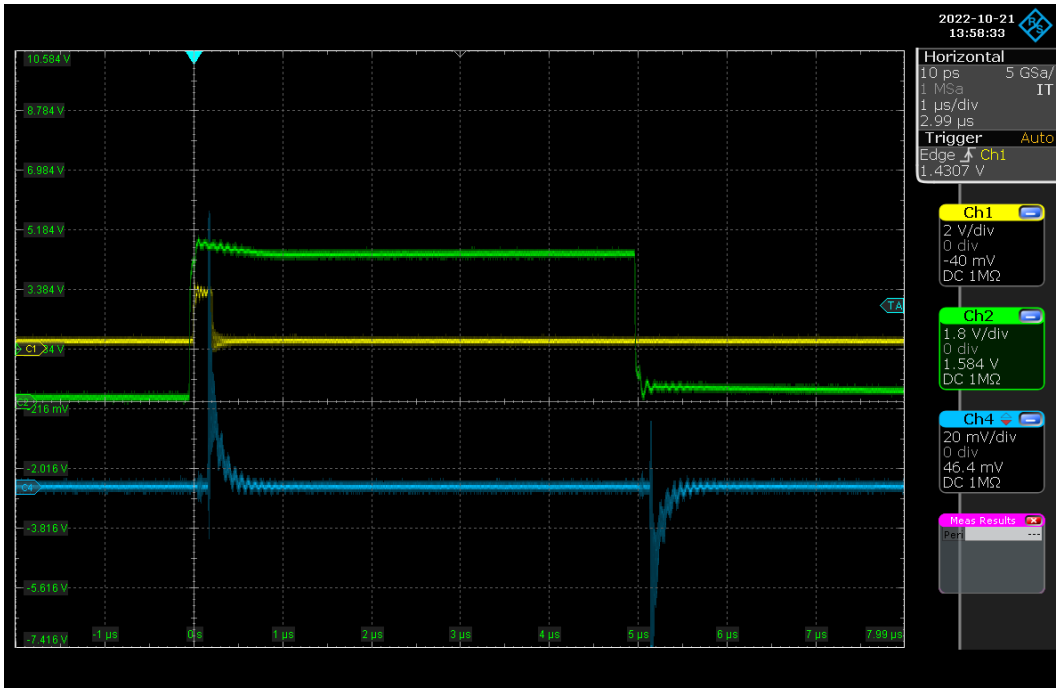

Fig. 2.10: Oscillogram of the trigger signals between the TOF instrument and the transient recorder card (digitizer)

possible to adjust parameters unused in a particular operation mode, such as the corona needle voltage during an ESI experiment. Nonetheless, the corona needle voltage change is still transmitted to the instrument and can be used as a control signal for other purposes.

An Arduino microcontroller (Arduino Due R3, Arduino, Ivrea, Turin, Italy) running a custom program was used to monitor the data traffic and to wait for changes in the control parameter. If such a situation arises, the microcontroller can send control signals to other hardware components. In this case, the microcontroller was used to control an external HPLC pump (L-6000A Pump, HITACHI, Ltd. Tokyo, Japan) that was incompatible with the MS data acquisition software for direct control.

2.8 Oscilloscope and Arduino Settings

As described in section 2.1 and illustrated in Figure 2.1, an oscilloscope (RTE 1054, Rhode & Schwarz, Munich, Germany) was connected to the auxiliary SEM detector located downstream of the oa-stage to display the electrical signals as a function of time graphically. The voltage is plotted on the Y-axis, and the time is plotted on the X-axis, as depicted in Figure 2.11.

An oscilloscope trigger stabilizes the waveform display by starting the sweep at a consistent point of a periodic signal. In this case, the only periodic signals are the push signals as shown in Figure 2.11. However, here, the areas between the pusher peaks are interesting since droplet signatures will appear randomly. Thus, a trigger mask was used to combine different interdependent trigger events, in that the activation of the first trigger is required to enable the second trigger. Simply triggering on the falling edge of a droplet signature signal would not work due to the very sharp pusher peaks, which would also activate the trigger multiple times in every measurement cycle. To circumvent this issue, the trigger sequence utilizes the "Trigger In" signal, described in section 2.7, as inhibition signal: If a rising edge in this channel is detected, the trigger sequence pauses for the duration of the push and then resumes listening for a falling edge in the actual SEM signal until the sequence resets at the end of the measurement cycle. Consequently, this sequence masks the pulses produced by the pusher. Additionally, there is a trigger threshold setting ("trigger level") that affects when the trigger will activate in response to the level of rising or falling signal edge or slope. This level was individually adjusted to prevent triggering on noise while ensuring no ion bursts were missed. However, due to the varying intensity of the ion bursts, very low intensity bursts are regularly missed.

The oscilloscope was configured to send a $5\,\mathrm{V}$ signal with a duration of $1\,\mu\mathrm{s}$ to an Arduino microcontroller (Arduino DUE R3, Arduino, Ivrea, Turin, Italy) when the oscilloscope trigger was activated. The microcontroller counts the incoming signals within time intervals of $5\,\mathrm{s}$ or $10\,\mathrm{s}$ from which the signal burst occurrence frequency was calculated.

The employed oscilloscope has two input impedance settings, both unsuitable for accurately recording the ion current in this instance. The $50\,\Omega$ impedance setting provides a time resolution that causes the oscilloscope to capture every single hit from a charged particle. However, the oscilloscope's digital electronics cannot transform the resulting rapid pulses into a pulse rate. The input port of the oscilloscope can also be switched to high impedance of $1\,\mathrm{M}\Omega$. In this mode, the signal fall time becomes so slow due to the impedance mismatch that a feasible time resolution is essentially lost. As a compromise, a $1\,\mathrm{k}\Omega$ resistor was connected in parallel with the $1\,\mathrm{M}\Omega$ internal impedance, resulting in a total impedance of approximately $1\,\mathrm{k}\Omega$.

The oscilloscope was usually connected to the SEM of the micrOTOF to display and record the time-resolved ion current. Figure 2.11 shows a typical result.

The distance between the pulser on time pulses corresponds to the TOF repetition rate (see Figure 2.6). The pulse itself has a fixed duration of $5\,\mu\mathrm{s}$. In Figure 2.11, these pulses appear as two sharp peaks with a $5\,\mu\mathrm{s}$ interval due to crosstalk from the pusher electrode (marked with (A) in the figure). Between the pushes, the

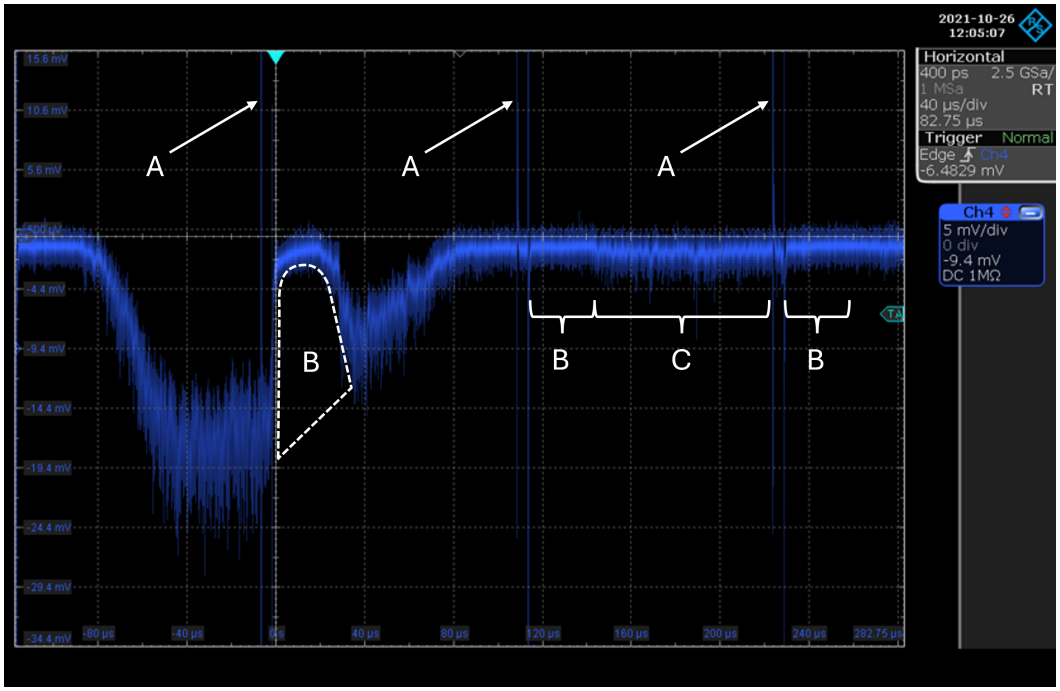

Fig. 2.11: Exemplary oscillogram showing a wide ion burst signal interrupted by a push into the TOF flight tube. (A) are the $5\,\mu s$ pushes, (B) are the blank regions after the push, where the current ion beam has been pushed into the flight tube. The typical ion current is evident in the third measurement cycle, annotated with (C).

ion current striking the SEM is observable. Right after each push, a blank region of approximately $40\,\mu s$ is apparent (marked with (B) in the figure). This period represents the time required to refill the oa-stage with new ions after a TOF push accelerates all ions from the stage to the TOF flight tube. After approximately $40\,\mu s$, the new ions reach the SEM, appearing as a negative signal in the oscillogram until the next push occurs.

Within ESI experiments, very intense ion signal bursts occur, which are attributed to aspirated droplets or at least the "debris" of aspirated droplets. These structures are unique to ESI and do not appear to be employed by APCI or APPI. This work investigates the occurrence of these bursts under various conditions. One basic interesting parameter is the frequency of their appearance.

2.9 Experiment Automation

The Bruker acquisition software enables the creation of so-called method files. These files encompass all variable parameters for each defined segment in a measurement. The method files are encoded in XML (Extensible Markup Language), facilitating automated editing and generation. A Python script was developed to automate the creation of method files with a high number of individual segments.

Tab. 2.1: Operating parameters used for ESI and APCI experiments if not declared otherwise.

Parameter	ESI (pos.)	ESI (neg.)	APCI (pos.)	APCI (neg.)
Source Parameter				
Liquid Flow in $\mu\mathrm{L\,min^{-1}}$	10	10	10	10
Inlet capillary voltage in V	-4000	4200	-4200	4200
Nebulizer pressure in bar	0.4	0.4	0.4	0.4
Dry gas flow in $\mathrm{L/min}$	4	4	5	5
Dry gas temperature in $^\circ\mathrm{C}$	180	180	200	200
Vaporizer temperature $^\circ\mathrm{C}$	-	-	430	430
End Plate Offset in V	-439	439	-500	500
Transfer Parameter				
Hexapole AC in V	150			
Lens 1 Transfer Time in μs	108			
Lens 1 Pre-Pulse Storage Time in μs	5			
Lens Storage in V	25	-25	25	-25
Lens Extraction in V	18.9	-19.3	18.9	-19.3
Lens 2 in V	7.1	3.2	7.1	3.2
Lens 3 in V	-30	93.7	-30	93.7
Lens 4 in V	-7.8	11.1	-7.8	11.1
Lens 5 in V	11.0	26.2	11.0	26.2
Skimmer 2 in V	23.9	-24.0	23.9	-24.0
Hexapole DC 1 in V	28.5	-21.5	28.5	-21.5
Hexapole DC 2 in V	17.9	-17.5	17.9	-17.5
TOF Parameter				
SEV Detector in V	2000			
MCP Detector in V	2097			
Pulsar Push in V	396	860	396	860
Pulsar Pull in V	0	0	0	0
Corrector Fill in V	60	25	60	25
Corrector Extract in V	419	810	419	810
Flight Tube in V	8500	9000	8500	9000
Decelerator in V	0	0	0	0
Reflector in V	1714	2043	1714	2043

A different set of parameter values was applied for each experiment, as described in the respective sections. In general, the in Table 2.1 depicted parameter values were applied if not declared otherwise.

2.10 Chemicals

All described experiments were performed using a solution of Reserpine (crystalline, $\geq 99.0\,\%$ HPLC grade from Sigma Aldrich). Reserpine is a well-known calibrant standard for LC-MS systems [7]. The solid was dissolved in a 1:1 solution of acetonitrile (HPLC-grade, obtained from VWR chemicals) and water with $0.1\,\%$ formic acid ($\geq 98\,\%$ purity, obtained from Sigma-Aldrich). The resulting stock solution had a concentration of $8\,\mu\mathrm{mol\,L^{-1}}$.

Extended storage durations in glass containers resulted in sodium ions dissolving and combining with Reserpine to form the Na-adduct.

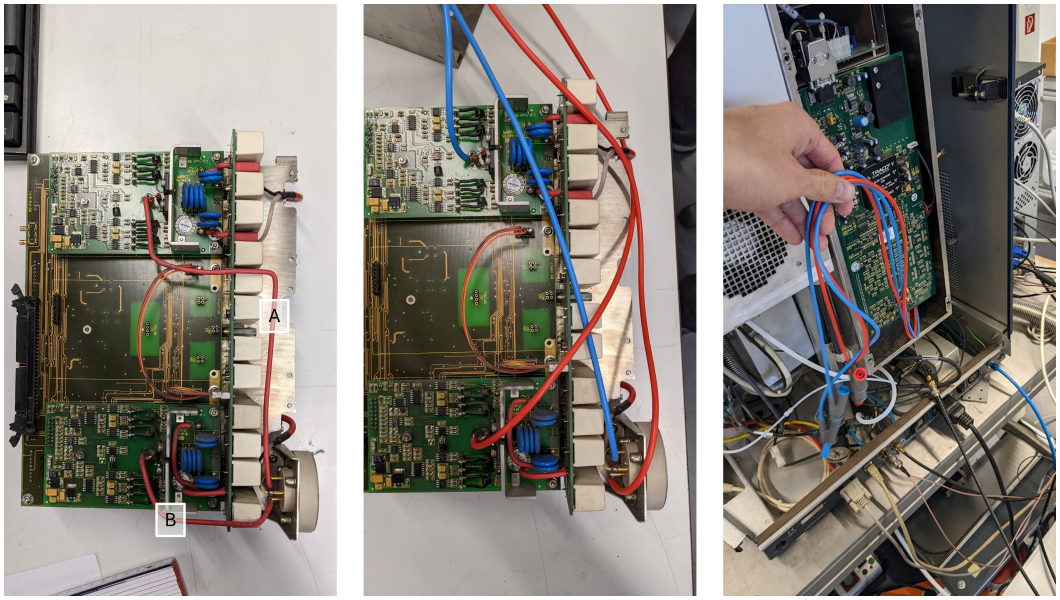

Fig. 2.12: Photography of the HV-module of the used micrOTOF. The left panel shows the original module with the two cables A and B. Both cables were replaced with plug connections, which were easily accessible.

2.11 Injection System

The analyte-containing solution was injected in two ways: first, through a Fusion 100T syringe pump (Chemyx In, Thermo Fisher Scientific, Waltham, Massachusetts, USA) and a 2.5-mL Hamilton Syringe (Reno, Nevada, USA) with a liquid flow rate set to $7\,\mu\mathrm{L\,min^{-1}}$, and later, through an HPLC system (L-6000A, Hitachi, Ltd., Tokyo, Japan) with a liquid flow rate between $7\,\mu\mathrm{L\,min^{-1}}$ to $10\,\mu\mathrm{L\,min^{-1}}$.

2.12 Attempting to Use a Custom HV Switch

Section 6 indicates a connection between high-intensity single non-summed spectra and ion bursts. One promising idea was to activate the TOF pusher only when an ion burst starts to be registered on the SEM. Since the ion bursts can last up to a few $100\,\mu\mathrm{s}$ and the electronics within the oscilloscope are fast with short latency, this approach appeared to be feasible. However, the internal electronics of the TOF instrument allow only for periodic pusher activation triggered by the computer, as described in section 2.7.1.

In an initial attempt, the connection to the high-voltage (HV) module was identified and replaced with two easy-to-reach plug connections, enabling manual control of the module, as depicted in Figure 2.12.

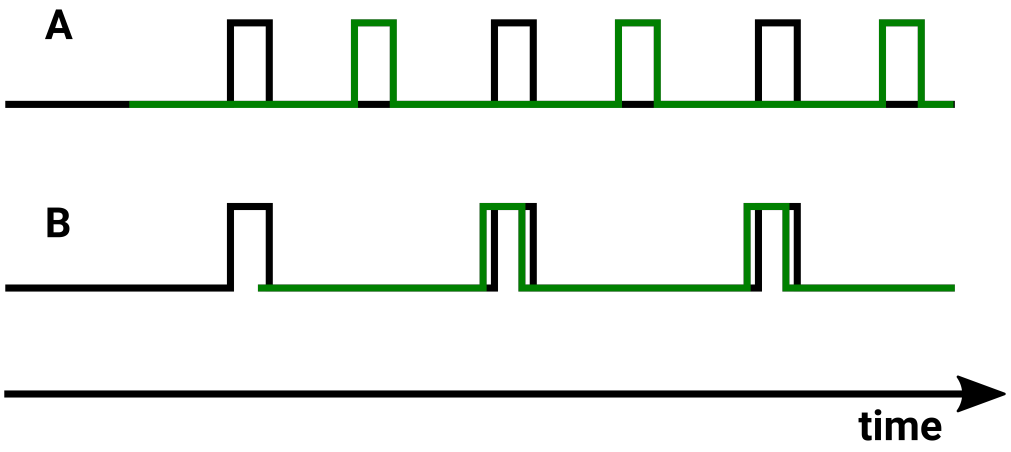

Fig. 2.13: Timing diagram of the original pusher trigger in black. This signal was not sent to the HV module but was used to create a similar, but delayed, push trigger signal (green). The delay depicted in (A) resulted in no mass spectra. After adjusting the delay to the situation depicted in (B), mass spectra arose.

The modified HV-module works as before with the original Bruker cabling. In addition, the plug connections enable manual triggering of the HV pulses generated by the HV-module.

At first, the oscilloscope uses the original pusher trigger signal from the transient recorder card to be triggered, sending a delayed external trigger signal to the HV-module, to verify the overall functionality of manually triggering the HV pulses. The created external trigger signal is identical to the original pusher trigger signal from the transient recorder, but with a delay as depicted in Figure 2.13. Initially, no mass spectra were observed, but after adjusting the delay time of the oscilloscope's trigger output, mass signals appeared. It was observed that the peaks in the mass spectra correspond to the delay time, as they shift in their m/z position. However, the mass spectra received contained unidentifiable peaks, with parts of the peaks mirrored in higher m/z ranges. Since the original pusher is a periodic signal, it is very likely that the adjustment has phase-shifted the delayed trigger signal by an integer multiple of the period, as shown in panel B in Figure 2.13.

Hence, pushing appears to be possible within a limited range (within the range of the original push); if the manual trigger signal does not appear in this range, activating the pusher is not feasible. However, determining the cause of this pusher activation range proved challenging.

Manual, non-periodic triggering of the pusher, which would be necessary when triggering on ion bursts, did not yield any mass spectra. It is likely that the chance

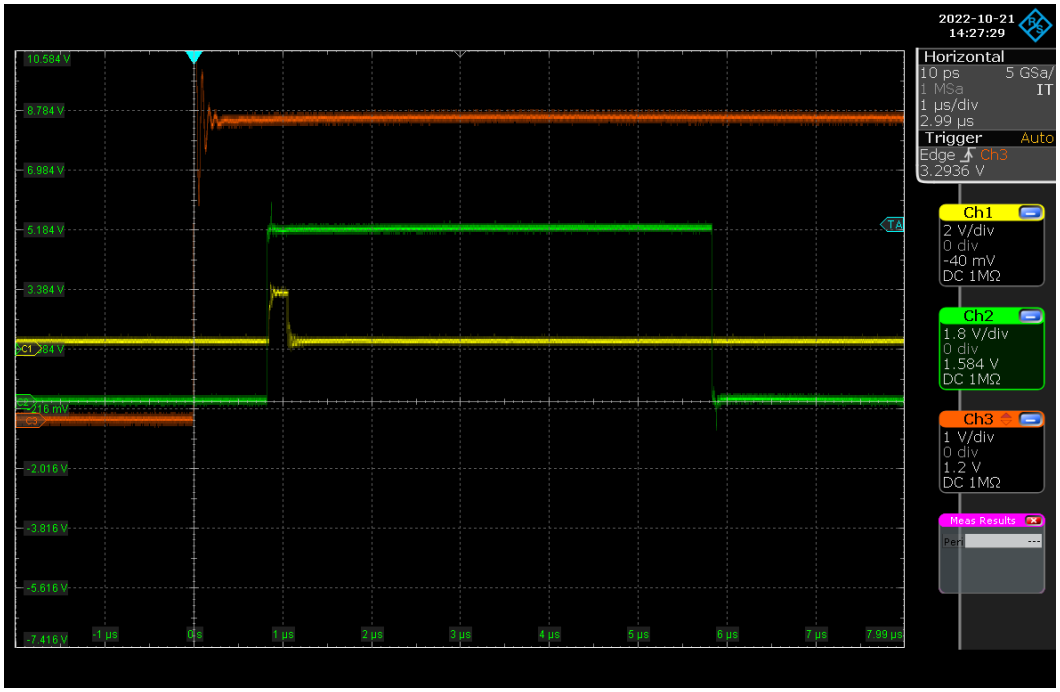

Fig. 2.14: Screenshot of an oscillogram while trying to implement an external trigger for the instrument's pusher

of unintentionally hitting the activation window is too low, and/or other unknown parameters affect the activation of the pusher.

A second attempt involved manually triggering the pusher in the same periodic pattern as the transient recorder card does while monitoring it with an oscilloscope. Figure 2.14 presents an oscillogram with an externally generated signal from an Arduino board (orange). The oscilloscope is configured to trigger on the orange channel and simulates the Trigger In signal from Figure 2.9 on the green channel. This procedure successfully induces a proper Trigger Out signal (yellow) and enables the pusher. The next approach was to use the original push trigger as a reference for the pusher activation window. When an ion burst is detected, the oscilloscope should wait until the subsequent pusher activation window and then manually trigger the pusher. Unfortunately, no mass spectra were obtained using this method, which reinforces the earlier assumption that further unknown parameters hinder the manual triggering of the pusher.

The third attempt involves an external HV switch, as using the internal HV module was not feasible. The external switch should be activated by a Transistor-Transistor-Logic (TTL) signal when an ion burst strikes the SEM and creates a push, just like the internal HV-module does. Unfortunately, this attempt had to be aborted due to an insufficient understanding of the internal logic of the push process within the micrOTOF.

References

[1] Francois Joseph Gerard V. Bosch. „Electron multiplier“. 2408709. Oct. 1946 (cit. on p. 29).

[2] Bruker Daltonik GmbH. *micrOTOF - micrOTOFcontrol 1.1 - Operator Manual*. May 2005 (cit. on pp. 19, 22–26, 28, 29).

[3] com0com Project. *com0com - A Null-modem emulator*. `https://sourceforge.net/projects/com0com/`. Accessed: 2025-04-09. 2022 (cit. on p. 32).

[4] Robert J. Cotter. „Time-of-flight mass spectrometry“. In: Wiley, Sept. 2005 (cit. on p. 28).

[5] Jürgen H. Gross. *Mass Spectrometry*. Springer International Publishing, 2017 (cit. on pp. 22, 23, 28–30).

[6] Michael Guilhaus. „Principles and instrumentation in time-of-flight mass spectrometry. Physical and instrumental concepts“. In: *Journal of Mass Spectrometry* 30 (11 Nov. 1995), pp. 1519–1532 (cit. on p. 28).

[7] Sunil Kumar, Awantika Singh, Vikas Bajpai, et al. „Structural characterization of monoterpene indole alkaloids in ethanolic extracts of Rauwolfia species by liquid chromatography with quadrupole time-of-flight mass spectrometry“. In: *Journal of Pharmaceutical Analysis* 6 (6 Dec. 2016), pp. 363–373 (cit. on p. 36).

[8] Henry E. Stanton, William A. Chupka, and Mark G. Inghram. „Electron Multipliers in Mass Spectrometry; Effect of Molecular Structure“. In: *Review of Scientific Instruments* 27 (2 Feb. 1956), pp. 109–109 (cit. on p. 29).

[9] W. C. Wiley and I. H. McLaren. „Time-of-Flight Mass Spectrometer with Improved Resolution“. In: *Review of Scientific Instruments* 26 (12 Dec. 1955), pp. 1150–1157 (cit. on p. 25).

[10] Joseph Ladislas Wiza. „Microchannel plate detectors“. In: *Nuclear Instruments and Methods* 162 (1-3 June 1979), pp. 587–601 (cit. on p. 30).

3 Introduction to the Cumulative Part

The publications presented below were composed between 2022 and 2024 and demonstrate the progress of research into various areas related to droplet observations using ESI-MS.

The first publication titled "**Observation of Large, Charged Droplet Signatures within the High-Vacuum Region of a Commercial Electrospray TOF-MS**" was published on **February 26, 2024**, in the *Journal of the American Society for Mass Spectrometry*.

This publication summarizes the knowledge gained to date about charged droplet fragmentation and ion burst generation in electrospray ionization, using the experimental configurations and methods described in section 2. Time-resolved ion current measurements using the auxiliary SEM detector located downstream of the oa-stage revealed intense ion bursts, suggesting the presence of charged droplet debris containing thousands of ions. Analysis of pulse widths and ion source parameters (e.g., capillary voltage, drying gas flow, and nebulizer gas flow) indicated no consistent effect on droplet fission location, with fission events occurring randomly within the ion transfer stage.

The work highlights the variability in droplet size and charges as key contributors to the observed phenomena, emphasizing the need for further investigation of droplet aspiration and fragmentation mechanisms. The findings indicate a longer lifetime of generated droplets than generally expected in the ESI literature, resulting in large aggregates that penetrate the high-vacuum region of ESI-MS. This work establishes a foundation for a better understanding and modeling of ESI dynamics, which is crucial for optimizing the performance of mass spectrometers utilizing ESI sources.

The second work, "**Influence of Polarity Mode Switching and Standby Times on Signal Stability and Detection of Aspirated Droplet Signatures in Electrospray Mass Spectrometry**," was published in the *International Journal of Mass Spectrometry* in **May 2024**.

This study investigates signal stability and droplet signature appearance in TOF-MS systems, with a focus on the effects of polarity mode switching and instrument standby time. It was found that the signal intensity recorded with the Bruker micrOTOF decreased within the first hour of operation. However, the work revealed that prolonged standby periods, exceeding one day, result in almost complete recovery of the signal intensity. Polarity mode switching provides a quicker recovery method, with a 5-minute switch restoring up to $80\,\%$ of the original signal intensity, while shorter switches result in less favorable recovery. The rapid alternation between positive and negative polarity every two minutes stabilizes analyte signals and droplet signature frequencies over long-term measurements. Signal instability was associated with the probable charging of instrument components, such as the glass inlet capillary, and the presence of droplet signatures, particularly in ESI. These irregularities cause fluctuating ion currents, contributing to both short-term signal variance and long-term drift. Intense ion bursts linked to droplet signatures are believed to enhance signal fluctuations and charge buildup. By employing strategies such as polarity mode switching and effective standby time management, the study demonstrates the significant impact that droplet signatures can have on the analytical performance of the instrument.

The third publication is titled "**Signatures of Charged Droplets from ESI: A Statistical Analysis of Non-Summed Mass Spectra Compared to APCI**" and was published on **May 25, 2025**, in the *Journal of the American Society for Mass Spectrometry*.

This publication investigates the differences between individual (non-summed) mass spectra using APCI and ESI. APCI spectra consistently fall into low-intensity categories with small variations, contributing uniformly to the total intensity. In contrast, ESI spectra exhibit a stark intensity disparity: a small subset of high-intensity single spectra dominates the overall signal, while most individual spectra remain completely empty. Droplet signatures, unique to ESI, are thought to contribute to these high-intensity spectra, with their occurrence significantly influenced by source parameters such as capillary voltage, nebulizer pressure, and dry gas flow. ESI spectra display a broad intensity range, while APCI spectra show comparably small change except at very low nebulizer pressures ($<2\,\mathrm{bar}$), where nebulizing performance becomes poor. Similarly, variations of the dry gas flow have a more pronounced effect on ESI; higher flow rates result in higher intensity and more frequent droplet signatures. Summed spectra analyses reveal that high-intensity ESI spectra — representing only $3\,\%$ of the total number of recorded spectra — contribute to the total signal. This contrasts with APCI, where the intensity remains consistent. In addition, no droplet signatures are observed at all. The work also employs optical monitoring to confirm that droplet signatures are intrinsic to ESI dynamics and not artifacts of spray instability.

4

Observation of Large, Charged Droplet Signatures within the High-Vacuum Region of a Commercial Electrospray TOF-MS

Reproduced with permission from: Chris Heintz, Lisa Schnödewind, Oliver Braubach, et al. Observation of Large, Charged Droplet Signatures within the High-Vacuum Region of a Commercial Electrospray TOF-MS. Journal of the American Society for Mass Spectrometry, 2024, 35(3), https://doi.org/10.1021/jasms.3c00383.

4.1 Abstract

Electrospray ionization (ESI) is one of the most prominent atmospheric pressure ionization techniques in modern mass spectrometry. It generates charged droplets from an analyte-containing solution as an initial step in the ionization process. Textbooks and the majority of the articles assume the entire droplet evaporation and release of bare analyte ions within the ionization chamber. However, non-mass-spectrometry-related literature and recent reports related to mass spectrometry demonstrate droplet observation in regions of the vacuum systems of a variety of mass spectrometers. In this work, we report on the observation of large droplet fragments within the orthogonal acceleration stage of a Bruker micrOTOF by connecting an oscilloscope to an auxiliary ion current detector downstream of the acceleration stage. Moreover, we detected fragment debris even with the MCP TOF detector by evaluating individual TOF spectra. Droplet fragments appear as pronounced and intensive pulses of the ion current. This observation is clearly connected to ESI, as other atmospheric pressure ionization methods do not show this behavior. The recorded droplet signatures show clear dependencies on the ion source and transfer stage parameters. The existence of large and highly charged droplets may adversely affect or at least impact the analytical performance of the instrument due to space charge or complex heterogeneous chemical reactions. Furthermore, the penetration

of large charged aggregates into the vacuum system explains the reported surface contamination after multipole stages. This contamination of critical components leads to substantially higher maintenance efforts.

4.2 Introduction

The first reported application of an electrospray ionization measuring device was by Malcolm Dole in 1968 [8]. In the later 1980s, John Bennett Fenn et al. developed and improved the ESI technique [9, 25], which became one of the most frequently used atmospheric pressure ionization (API) methods in modern mass spectrometry [9, 7, 17, 4, 12, 25] for which Fenn was awarded a Nobel Prize in 2002. The main reason for its wide use is the ability to produce large intact ions in the gas phase from a liquid solution [9, 25].

A typical ESI source consists of a thin metal needle creating a strong electrical field gradient (point-plane electrode geometry). The inlet into the vacuum system of a mass spectrometer (MS) is commonly the counterpoint for the electric potential on the ESI needle. This inlet stage is realized by a glass or metal capillary surrounded by a spray shield or a system of skimmers acting as plane electrode. A liquid solution containing the analyte is pumped through the needle. By applying a potential of some kV between the needle and counter electrode, electrochemical and electrodynamical processes in the analyte solution lead to charge separation in the liquid. This leads to the formation of a so-called *Taylor-Cone* at the tip of the needle [17, 23, 34, 5]. In the ideal case, the distance between the mobile charge carriers becomes smaller with decreasing liquid cone diameter until the Coulomb forces overcome the surface tension due to the increased charge density [17, 23, 34, 5]. The cone tip breaks down into a fine spray of charged droplets [7, 17, 23, 29, 5, 30]. The formed droplets shrink in size by evaporation of solvent molecules [9, 7, 23]. Since the number of charges within the droplet remains constant, its charge density increases until the Coulomb forces overcome the surface tension, similar to the process leading to the Taylor cone until droplet fission occurs. [9, 7, 5]. This critical point is often referred to as the *Rayleigh limit*, and the fission/fragmentation event is often denoted as *Coulomb explosion* or *Coulomb fission*. The number of elementary charges in the droplet z_R in dependence on its radius R and the surface tension is given by the following equation [32, 34, 5]:

$$z_R = \frac{8\pi}{e}\sqrt{\epsilon_0 \gamma R^3} \tag{4.1}$$

where e is the elementary charge, γ is the surface tension and ϵ_0 is the vacuum permittivity. Initially, it has been assumed that the Coulomb fission of droplets takes

Tab. 4.1: Experimentally Observed Droplet Sizes under Various Conditions

analyte/solvent	**observed droplet size**	**reference**
Pure solvents (water, acetonitrile, **n**-heptane, **n**-octane, **p**-xylene)	$25\,\mu\mathrm{m}$ to $35\,\mu\mathrm{m}$ with an observed droplet lifetime of $200\,\mathrm{ms}$ to $400\,\mathrm{ms}$	Smith et al. [33], Grimm et al. [16]
Heptane	Up to $100\,\mu\mathrm{m}$ with $466\,\mu\mathrm{L\,min^{-1}}$ liquid flow rate, $5\,\mu\mathrm{m}$ with $4\,\mu\mathrm{L\,min^{-1}}$ liquid flow rate	Gomez and Tang [14]
Fluorescent dyes in acetonitrile	$6\,\mu\mathrm{m}$ in positive mode, $20\,\mu\mathrm{m}$ in negative mode	Wortmann et al. [36]
Water/methanol solution with desorption electrospray ionization (DESI) emitter	Up to $10\,\mu\mathrm{m}$ with $2\,\mu\mathrm{L\,min^{-1}}$ liquid flow rate	Venter et al. [35]
Fluorescent dye in 20% methanol/water mixture	$2\,\mu\mathrm{m}$ with $50\,\mu\mathrm{L\,min^{-1}}$ liquid flow rate	Girod et al. [13]
Glycerol seeded with 3.8% weight NaI	In the range of $0.1\,\mu\mathrm{m}$	de la Mora et al. [30]

place multiple times until droplet sizes of a few nanometers are reached. However, some more recent work has shown that droplet fission can occur before reaching the Rayleigh limit. Due to their dynamic behavior, droplets often appear in oblate or prolate shapes with an elongated end caused by shear forces [17, 34, 5]. Taflin et. al. [34] demonstrated the ejection of a series of much smaller droplets from the elongated end of such a droplet. Interestingly, they report a mass loss between 1-2% but a 10-18% charge loss, due to the fact that the charge density on the surface is inhomogeneous but elevated in the elongated end caused by its stronger curvature [17, 34].

However, the exact mechanism of the final step of ESI, the release of single ions from the charged droplets, is still under discussion. There are currently multiple proposed mechanisms found in the literature for this process [26, 1, 7, 21, 28]. However, the exact mechanism of single ion release most likely depends strongly on the individual analyte and solvent system [26].

The size of the initial droplets ejected from the Taylor cone is extensively discussed in the literature [33, 16, 35, 36, 13]. Textbooks [17, 20, 4] and early review papers [23, 24] estimate the initial droplet size to be around 1-2 μm. This is in stark contrast to reported experimental observations made by different groups and with different analyte and solvent systems. Markert et al.[27] and Cole [4] give an overview of some of these experimentally determined droplet sizes. The reported sizes vary in a surprisingly large range between 2 and 100 μm. Most droplets were directly observed via optical methods such as phase Doppler anemometry. Table 4.1 gives an overview of different observed droplet sizes under various conditions and with different analyte and solvent systems.

This diverse list of largely different droplet sizes is not surprising considering the complex formation mechanism of the droplets, which is highly affected by various

spray parameters [29, 25] as for example liquid flow rate, liquid conductivity, gas flow rates, analyte and solvent system, and the potential difference between ESI emitter/needle and counter electrode. Fernadez De la Mora et. al. [30] discovered that the initial droplet radius a is approximately proportional to the liquid density ρ and its surface tension γ and most importantly to the liquid flow rate Q, as given by Equation 4.2.

$$a \sim \left[\frac{pQ^2}{2\gamma\pi^2} \right]^{\frac{1}{2}} \tag{4.2}$$

This is in rough accordance with the experimental results from Table 4.1. Results suitable for meaningful comparisons are from Gomez and Tang [14] as they employed the same analyte in their experiments but different flow rates. Assuming a droplet diameter of $100\,\mu\mathrm{m}$ and $466\,\mu\mathrm{L\,min^{-1}}$ liquid flow rate, the diameter for a flow of $4\,\mu\mathrm{L\,min^{-1}}$ should be around $8\,\mu\mathrm{m}$ according to Equation 4.2. Gomez and Tang report $5\,\mu\mathrm{m}$, which is a good agreement considering the experimental uncertainty and the approximate correlation function.

However, Fernadez de la Mora et. al. [30] used a simple spray needle without the added complexity of pneumatically assisted ESI emitters, which are very common in modern instruments [17, 6]. Our own experimental observations strongly suggest that also the positioning of the spray capillary inside the outer nebulizer tube as well as the nebulizer gas flow affects the spray evolution. An electrospray can operate in a multitude of spray modes, some of them with pulsed flow conditions, multiple liquid jets, or similar complex flow patterns [18, 15, 3]. However, there is currently no published fundamental model that describes a spray mode other than the classical cone jet mode. The latter, however, is described repeatedly in the literature [10, 11, 19, 31, 12].

Based on the work of Kang et. al. [22], Markert et. al. [27] demonstrate that large amounts of charged droplets penetrate the high vacuum region of different mass spectrometers (SCIEX triple quadrupole with Q-Jet interface, Bruker amaZon QIT, and Agilent Q-ToF). It was shown that droplet presence in the analyzer region of mass spectrometers is most likely not an edge case of some instruments under special conditions but a general phenomenon. Deeply penetrating droplets can lead to contamination of ion optical elements as Kang et. al. have demonstrated [22] which leads to higher maintenance efforts and a potentially diminished analytical performance. This work builds upon these two publications and reports the direct observation of charged droplet signatures in the orthogonal acceleration stage of

a commercial TOF-MS equipped with a commercial, unmodified electrospray ion source.

4.3 Methods

4.3.1 Instruments

Two micrOTOF (Bruker Daltonik GmbH, Bremen, Germany) API-TOF-MS with a similar setup were employed. The instruments differ in the detailed setup of the orthogonal acceleration stage since they are from different instrument generations. The main differences are the shape of the used pushing and accelerating electrodes and the acceleration mechanism due to the different wiring of the electrodes. The second instrument was used to verify that the observed effects are no artifact of this specific instrument. In both cases, we used an Apollo ESI source, which is the default electrospray source for the Bruker micrOTOFs. The analyte solution was directly infused with a Fusion 100T syringe pump (Chemyx In, Thermo Fisher Scientific, Waltham, Massachusetts, USA) and used a 2.5-mL Hamilton Syringe (Reno, Nevada, USA). The liquid flow rate was set to $7\,\mu\mathrm{L\,min^{-1}}$ if not mentioned otherwise.

Figure 4.1 shows a schematic of the ion path and system components of both instruments. The differences in the electrode setup of the orthogonal acceleration stages are not depicted in this simplified scheme. All operational parameters were set to default values, which are described in the following, if not mentioned otherwise. The *nebulizer gas* flows through the outer tube of the ESI needle and pneumatically assists the formation of the electrospray. Nitrogen is used as the nebulizer gas. The default nebulizer gas pressure (given as relative pressure in reference to the ambient pressure) was set to 0.4 bar. The potential difference between the inlet capillary, which is the entrance to the vacuum system of the MS, and the ESI needle was set to $4\,\mathrm{kV}$. Additionally, a *spray shield* having an electrical offset with a default value of $500\,\mathrm{V}$ is located in front of the inlet capillary. Essentially, this setup forms an electrostatic lens towards the entrance of the inlet capillary channel. Notably, the ESI needle is on ground potential in the Apollo ion source, which simplifies the electrical safety handling of the ESI needle. Therefore, the MS inlet system, inlet capillary tip, and spray shield have to be kept on a strong attractive potential. The default electric voltage on the inlet capillary tip is $-4\,\mathrm{kV}$ in positive ion mode. To support the droplet evaporation the instruments use a heated dry gas stream also consisting of nitrogen gas with a default temperature of $180\,^{\circ}\mathrm{C}$. This gas stream counters the ion motion into the ion source chamber between the spray shield and the inlet capillary (cf. Figure 4.1). The dry gas flow was set to $4.0\,\mathrm{L\,min^{-1}}$ as the default value.

The ions reach the tip region of the inlet capillary through the dry-gas counter gas flow due to the attractive electric field. Since the inlet capillary is made of glass and therefore electrically insulating, its terminals are metal plated. This allows setting

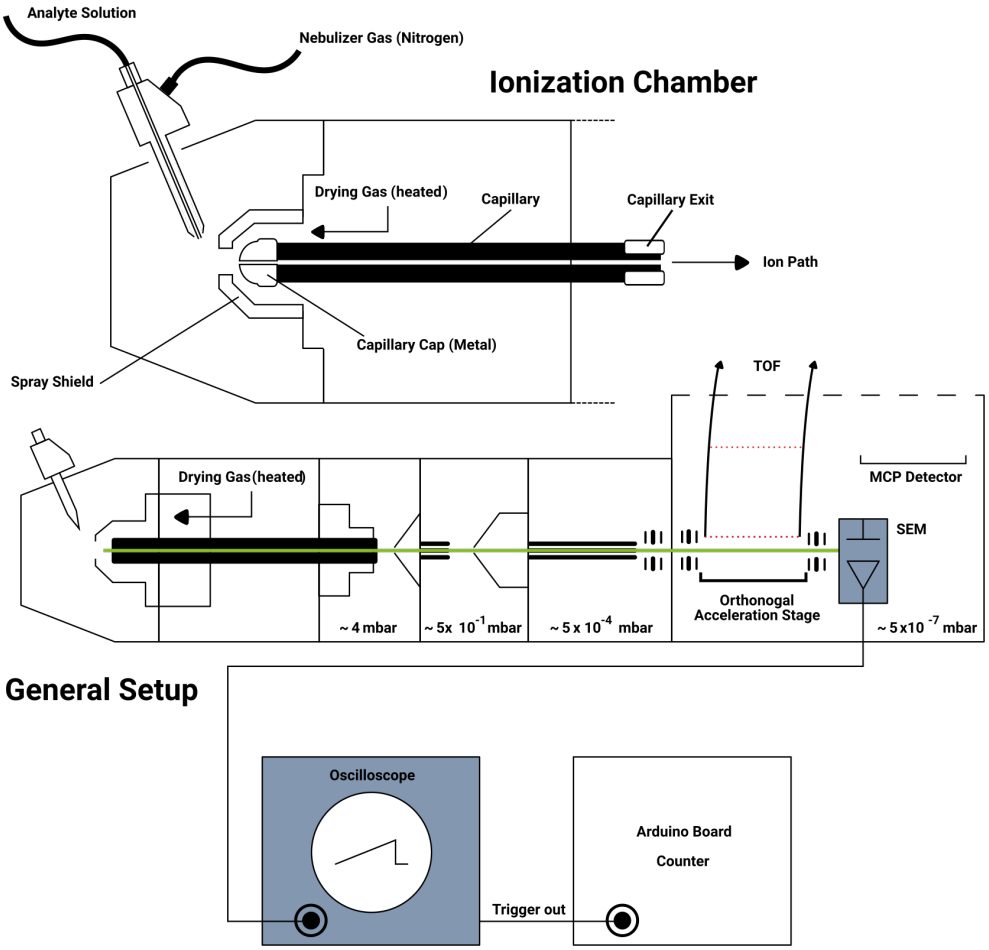

Fig. 4.1: Schematic of both Bruker micrOTOFs which were used in this work. The instruments used differ in the electrode setup of the orthogonal acceleration stage, which is not depicted in detail. The secondary electron multiplier (SEM) is originally intended to operate as an auxiliary detector to assist the tuning of the ion transfer optics. In this work, the SEM is connected to an oscilloscope to directly observe the time-resolved ion current and droplet signatures within the ion beam. The Arduino microcontroller board acts as a counter for recorded droplet signatures.

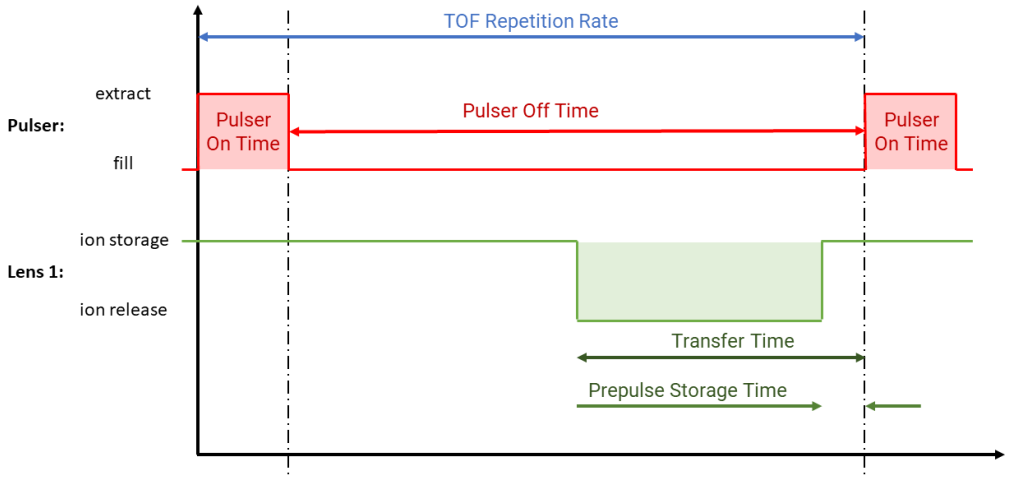

Fig. 4.2: Timing diagram for lens 1 and pulser [2]

the downstream end of the capillary (the *capillary exit*) to a convenient starting potential for the ion optical elements of the transfer stage further downstream, which is typically a slightly accelerating potential of $170\,\mathrm{V}$ in positive ion mode. Transport into and through the capillary channel itself, against the huge repulsive voltage gradient along the capillary (recall that the capillary entrance potential is $-4\,\mathrm{kV}$), is driven by viscous drag from the fast gas flow through the capillary acting on the charged particles (ions and droplets). The first element of the ion transfer system downstream of the capillary exit is a skimmer, followed by a hexapole, a second skimmer, and another hexapole. Both hexapoles are rf-only devices and act as ion guides. However, as with every multipole rf-ion guide, they have a low mass cut-off and thus essentially represent a high pass filter. The second hexapole is followed by a system of electrostatic lenses which act also as ion gate, which is synchronized with the orthogonal acceleration (oa) stage in the TOF analyzer region. Figure 4.2 shows a diagram of the timing of the ion gate and the TOF pulse sequence. The transfer time defines a time slot in which ions can pass the lens system toward the oa-stage prior to issuing the push/pull pulse. This sequence establishes a high mass limit: The longer the transfer time, the higher the upper **m/z** limit for transferred ions. The minimum value is $10\,\mu\mathrm{s}$ and the maximum value is $10\,\mu\mathrm{s}$ lower than the TOF repetition time. The prepulse storage is defined as the delay between the transfer time and the onset of the push/pull pulse. This sequence leads to a low mass limit: The higher the pre-pulse storage the higher the low mass limit. The minimum value is $1\,\mu\mathrm{s}$ and the maximum value is $10\,\mu\mathrm{s}$ lower than the transfer time. In the present experiments, the prepulse storage time was set to $1\,\mu\mathrm{s}$ and the transfer time to $50\,\mu\mathrm{s}$.

An oscilloscope (RTE 1054, Rhode & Schwarz, Munich, Germany) was connected to the secondary electron multiplier (SEM) located downstream of the oa-stage to directly observe the ion current. The SEM is originally intended to record the ion current entering the oa-stage for transfer optics tuning. The oscilloscope entrance impedance was set to $1\,\mathrm{k}\Omega$. The trigger mechanism of the oscilloscope is used to count the incoming large bursts of ion signal. Unfortunately, significant interferences occur, induced by the rising and falling electrical high-voltage pulses generated in the TOF oa-stage, visible as very sharp and intense signal peaks. To avoid triggering on these peaks, we use a more complex trigger sequence, using the internal low-voltage TTL signal of the mass spectrometer, which in turn drives the high-voltage switches of the oa-stage, on a second oscilloscope channel. The rate of detected ion burst signals is counted by an Arduino microcontroller board (Arduino DUE R3, Arduino, Ivrea, Turin, Italy) connected to the oscilloscope's trigger return port.

4.3.2 Chemicals

All experiments were done with an analyte solution containing reserpine ($\geq 99\,\%$ purity, obtained from Sigma-Aldrich) in a 1:1 mixture of water and acetonitrile (HPLC-gradient grade, obtained from VWR chemicals) and added $0.1\,\%$ formic acid ($\geq 98\,\%$ purity, obtained from Sigma-Aldrich). The solution had a concentration of $8\,\mu\mathrm{mol\,L^{-1}}$.

4.4 Results and Discussion

4.4.1 Observation of Droplet Signatures in the Time-Resolved Ion Signal

As outlined above, the stream of ions hitting the SEM downstream of the oa-stage was detected time-resolved. The oscillogram in Figure 4.3A shows the ion current which is periodically interrupted by two sharp transients, induced by electrical crosstalk from the high-voltage oa-stage ion extraction pulse. Immediately after the extraction pulse, only background noise and no ion signal are observed for a short time frame of about $40\,\mu\mathrm{s}$. This is the time required for the ions to refill the pusher region after one extraction. This time of signal absence at the SEM is called the *blank region* throughout this manuscript. The "bare" ions reaching the SEM are visible as a stream of individual pulses in Figure 4.3A, which resemble the continuous unresolved ion signal background. Within this background signal, we observe remarkably strong and wide signal bursts with an occurrence frequency of several hertz. Figure 4.3B shows an example of these ion bursts. They are orders of

magnitude larger in signal strength than the bare ion signal and generally feature a comparable width, typically up to $100\,\mu$s long.

We did not observe such ion bursts at all with API methods not using electrospraying, namely atmospheric pressure chemical ionization (APCI) and atmospheric pressure photo ionization (APPI). Furthermore, as described further down, we observe correlations between the occurrence frequency of the burst signals and ion source/ESI spray parameters. Therefore, we assign these extraordinary signals to charged droplets containing at least thousands of analyte ions and charges, which are aspirated into the vacuum system of the TOF instruments from the ESI ion source. However, the observation of pusher blank regions within the ion burst signal, as depicted in Figure 4.3C, provides clear evidence that not a highly charged closely confined particle is hitting the detector, but rather a burst of many small droplet fragments or ions, similar to a shotgun shot. A well confined particle would either be deflected by the oa-stage pulse into the TOF flight tube or travel unaffected in a straight line through the oa-stage, ultimately striking the SEM. It should be noted here, that our results do not exclude that highly charged large confined particles could indeed reach the SEM. Such a particle would create a highly transient and not extraordinarily large signal, which would probably not be distinguishable from the pulse background generated by the bare ions with the current detection electronics.

The detection of the ion bursts in the observed form strongly suggests that aspirated droplets can disintegrate into a highly correlated cloud of fragment ions. Currently, it is not entirely clear how a droplet disintegrates to form the observed ion bursts. Possible mechanisms for the decomposition and the location of fragmentation will be discussed in the following sections.

Disconnection of the internal trigger cable for the high-voltage oa-stage circuit and thus inhibiting this stage from operating lead to oscillograms as shown in Figure 4.4. No sharp oa-stage interference signals and no punched areas are occurring. This allows the analysis of ion burst signal shapes but comes at the cost of not being able to simultaneously determine mass spectra. The observed undisturbed droplet signatures show a wide variation in signal widths, shapes and intensities. Figure 4.4 shows an overview of the observed different signal shapes. The next section provides a detailed analysis of the varying widths.

4.4.2 Temporal signal width

In a highly correlated, shotgun-like ion burst generated upon the disintegration of an aspirated charged droplet, the ions are expected to disperse immediately after the initial fragmentation event that generated the burst. Subsequently, the ion

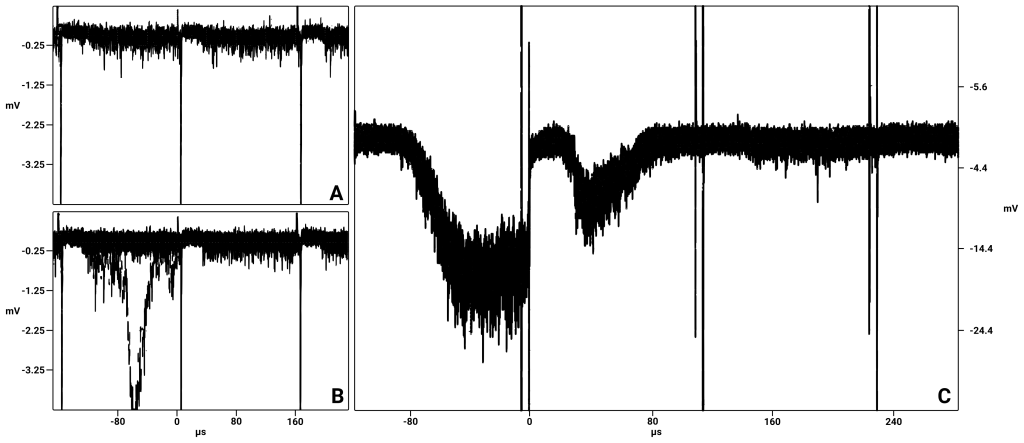

Fig. 4.3: Oscillograms within one measurement. (A) displays the regular ion current hitting the SEM which is periodically interrupted by the oa-stage ion acceleration pulse, which empties the oa-region. The time to refill the oa-region and thus recover the ion current signal on the SEM takes about $40\,\mu$s. (B, C) Examples of the observed very intense ion signal bursts. (C) Punching out a section of the ion burst and directing it into the flight tube. Hence, an observed ion burst is not generated by a single, large confined charged particle but by a large, partly stratified but still temporally highly correlated cloud of ions. We attribute the observed signal bursts to the fragments of highly charged liquid droplets, aspirated into the vacuum system of the instrument from the ESI ion source.

transfer region of the mass spectrometer essentially acts as a (crude) upstream TOF analyzer since the fragments produced by the initial droplet disintegration event have different charges and masses. Therefore, small fragments with higher charges will experience stronger electrical acceleration from potential gradients along their flight path within the transfer region and move faster than larger less-charged fragments. Furthermore, the ion cloud is further stratified due to Coulomb interactions between charged particles, also known as *space-charge*, and diffusion resulting from the collisions of the droplet fragments with the neutral background gas. Consequently, if the initial fragmentation event occurs far away from the oa-stage region (i.e., far upstream in the ion path through the MS transfer stage), the resulting ion burst signal will be much broader. In contrast, if the fragmentation occurs in closer vicinity to the oa-stage and thus SEM, the signal will be sharper due to the limited time available for dispersion. To quantify the distribution of ion burst pulse widths, we recorded numerous individual oscillograms within one measurement cycle, where all operational parameters were kept constant. The double-peak structure in the bottom panel of Figure 4.4 is not a random coincidence of two ion bursts. Rather, such complex signals with two maxima are systematically observed under defined experimental conditions. Currently, we have no detailed model that explains the formation of such double-peak signals. However, it is reasonable to assume that this signal shape is generated by the interaction of the ion cloud with elements of the ion transfer stage of the instrument.

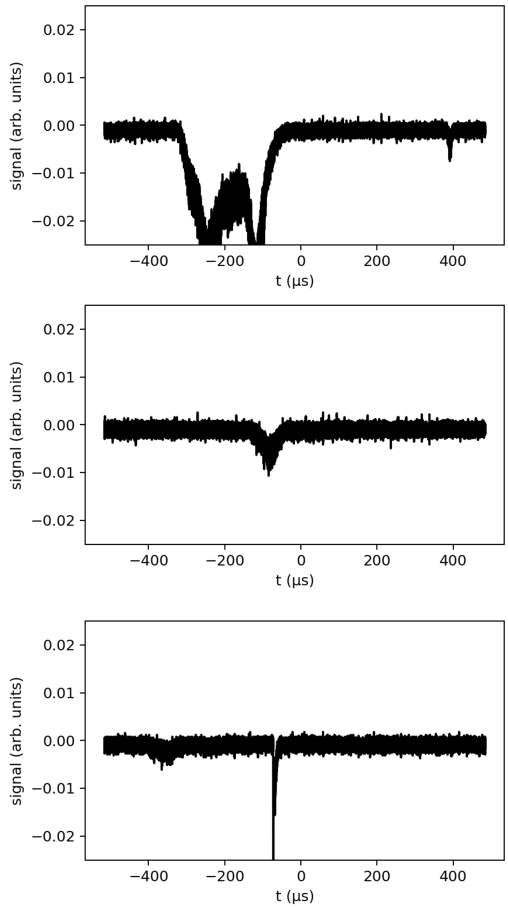

Fig. 4.4: Compilation of different droplet burst shapes, recorded within the same measurement and with an inhibited pusher, to observe the unobstructed signal shapes. The **x**-axis shows the time scale of the oscillogram. The ion bursts last for up to $200\,\mu$s.

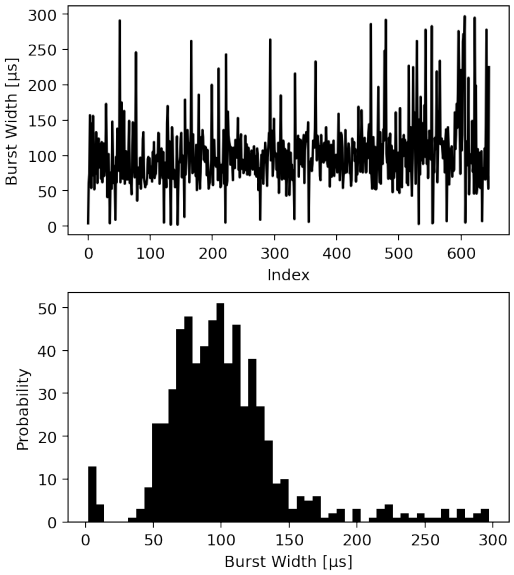

Fig. 4.5: (A, top) Chronological sequence of ion burst widths. There is no obvious trend recognizable; the different widths seem to occur randomly. (B, bottom) Ion burst pulse width distribution for the data in (A). The majority of the droplet bursts have a width between 50 and $150\,\mu$s, while a small secondary signal with pulse widths below $25\,\mu$s and a low-intensity tail above $150\,\mu$s is visible.

The top panel in Figure 4.5 depicts the chronological variation of ion burst signal widths within one measurement cycle upon changing some of the key parameters like capillary voltage, nebulizer flow, and drying gas flow within the analytically reasonable range for droplet observation. The bottom panel displays the distribution of ion burst signal widths, indicating that the most frequently occurring signal width is around 50 and $150\,\mu$s, with a notable asymmetrical tail towards broader widths.

The obtained results suggest that the changed parameters have no obvious effect on the ion burst pulse width and thus the average location of droplet fission. The high variability of the ion burst pulse width renders it difficult to locate the droplet fission region within the MS transfer system. Estimation of the droplet fission location is getting even more complex when considering that the initial droplets most probably largely vary in size and contain different numbers of charge carriers. A larger droplet certainly leads to a broader signal than a smaller droplet, assuming the same location of fission. Further knowledge about the size of the initial droplets leading to the ion bursts and a detailed modeling of the ion transfer stage is underway and will allow estimating the region where the fragmentation takes place. There is also a second group of ion bursts with a different distribution and significantly smaller mean widths.

4.4.3 Analysis of single mass spectra

Commonly, a TOF mass spectrum from a typical API-MS instrument consists of thousands of summed single spectra recorded within a defined period of time, since the rate of the oa-stage pulse is in the kHz range and the total ion number in a single ion injection is comparably low. However, with the observation of the pusher blank regions within the ion burst signals, there must be intense *single* mass spectra in the data set, since a significantly higher number of ions is injected into the flight tube when an ion burst resides within the oa-stage at that time. Figure 4.6A shows that there are indeed single ESI spectra with a significantly higher total intensity (throughout this work referred to as "superintense spectra") than the average of the recorded single spectra, which appear to be similar to the exemplary spectrum displayed in Figure 4.6B.

In the present sets of experiments, a typical *single* mass spectrum is shown in Figure 4.6B; it has a typical average total intensity of 450 counts. The highest superintense single mass spectrum has a total intensity of approximately $110\,000$ counts. In "normal" acquisition mode, around 1000 to 10000 single mass spectra are summed and then transferred as one data set to the host computer for further treatment. Assuming there is one superintense mass spectrum in a set of 1000 low-intensity single spectra, the summed spectrum will be up to $50\,\%$ higher total intensity than without containing a superintense spectrum. This means that the superintense spectra are contributing a significant fraction to the observed total intensity, even though they are comparably rare; in this example, 1 in 1000.

This is a feasible rationale for the relatively unstable ESI TIC signal intensity in comparison to APCI and APPI TICs, respectively. The latter are naturally operated without an electrospray but rather thermally generated sprays and thus with no *charged* droplets present in the mass spectrometer, as very low charge or neutral droplets are effectively filtered out/blocked by the inlet stage of the mass spectrometer or off-axis ion optical elements. Furthermore, we observed significant variability in the droplet/ion burst occurrence frequency within the first $30\,\mathrm{min}$ run time of an experiment. The TIC signal is remarkably unstable in this period, which is probably the reason why manufacturers generally advise a "warm-up" time of about $30\,\mathrm{min}$ when employing ESI.

Figure 4.7 shows the distribution of total intensities of the recorded single-spectra. This intensity histogram gives an impression of the occurrence frequency and intensity distribution of the superintense spectra.

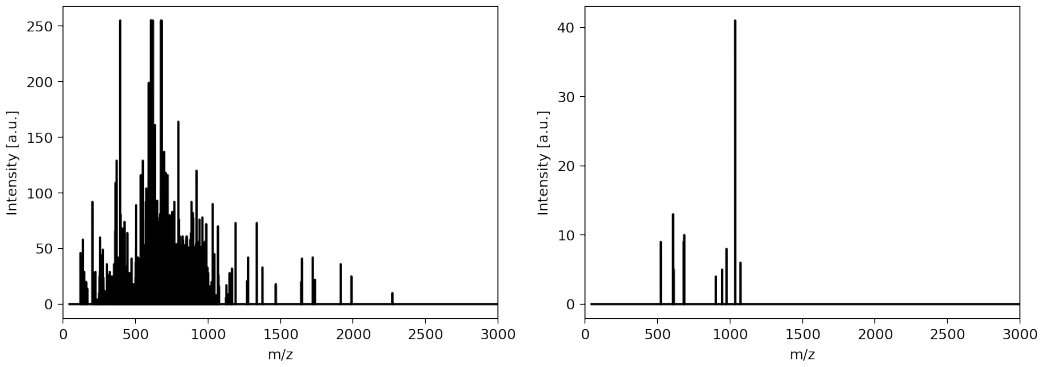

Fig. 4.6: Comparison between an example from an extraordinarily intense *single* spectrum ("superintense spectrum") (A, left) exclusively observed with ESI ionization, and an example of a regular *single* low-intensity spectrum that is typical for both ESI and other API methods (B, right).

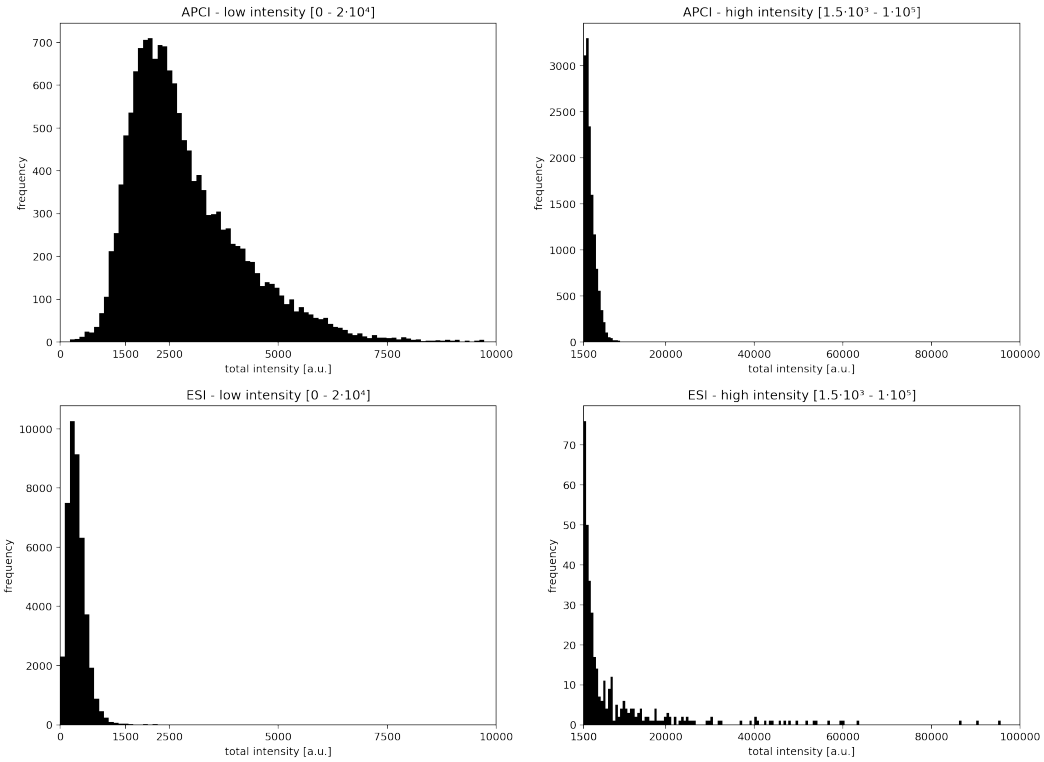

Fig. 4.7: Total intensity distribution of recorded single (non-summed) TOF spectra with APCI (upper row) and ESI (lower row). The left column shows the low-intensity area with intensities between 0 and $20\,000$, and the right column shows the high-intensity spectra with total intensities between $15\,000$ and $100\,000$. In contrast to other ionization methods, e.g., APCI, a group of extraordinarily intense spectra are visible with ESI while simultaneously the most probable intensities are significantly lower than with APCI.

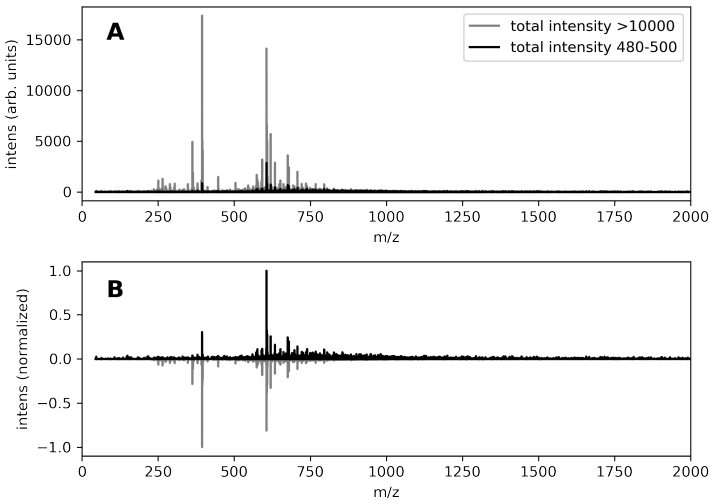

Fig. 4.8: (A) Mass spectra of summed single spectra with TICs above $1 \cdot 10^4$ (grey) and TICs between 480 and 500 (black), which is the most frequently observed TIC range (cf. Figure 4.7). The spectrum resulting from summing superintense spectra only shows a significantly higher TIC, even though far fewer single spectra were summed. (B) Normalized mass spectra for both cases. The resulting spectra are qualitatively similar but differ significantly in their signal distribution.

As discussed, the sum of all recorded single ESI mass spectra of the presented ESI experiment leads to a typical ESI mass spectrum, as expected. In a further analysis, we summed up all single-spectra with low and high intensities separately. In both cases, the resulting summed mass spectra exhibit defined signals as Figure 4.8 shows. Interestingly, the mass spectra differ in the location of their base peaks: The summed mass spectra with low total intensity show the highest intensities between m/z 500 and 750 while the summed superintense spectra exhibit a second maximum between m/z 250 and 500.

4.4.4 Dependence on source and ion transfer stage parameters

Variations of ion source and ion transfer stage parameters were performed to determine the dependency of the appearance frequency and signal shape of the observed ion bursts on these parameters. As described in the methods section, a microcontroller was connected to the oscilloscope output, recording the frequency of the ion bursts hitting the SEM. This number is referred to as “burst frequency” in the context of this manuscript. It is obviously dependent on the oscilloscope trigger configuration, which had to be changed from time to time to match the individual experimental conditions. Therefore, the absolute burst frequencies are not, in all cases, quantitatively comparable. However, *within* one experimental run, the burst frequencies are consistent and therefore comparable, since the trigger configuration

was not changed. Figure 4.9 shows results from ion source parameter variations with activated oa-stage and ion burst detection on the SEM. Generally, the TIC recorded with the TOF mass analyzer and the burst frequency are mostly not directly correlated.

In the first series of experiments, the effect of analyte solution constitution, nebulizer, and drying gas flow rate, and the capillary potential, respectively, were investigated. The capillary potential has a noticeable effect on the ion burst frequency: Each voltage step seems to change the burst frequency, but a simple dependence is not apparent. There is a maximum burst frequency at a capillary voltage of $2500\,\mathrm{V}$ and the highest TIC with simultaneously lowest burst frequency at $4000\,\mathrm{V}$. It is not surprising that the capillary voltage has a significant effect on the generation of droplets since it is essentially the ESI spray voltage in the Bruker Apollo source setup, which strongly affects the spray dynamics and the droplet transport to the mass spectrometer inlet. It is well-known that the spray mode is dependent on the capillary voltage [17]. A strong electrical field can lead to a multijet mode, for example, where not only one but multiple ion jets produce the spray. It is likely that the spray is generated via different spray modes, resulting in different droplet generation dynamics during the variation of the capillary voltage between 1000 and $4000\,\mathrm{V}$.

Variation of the "dry gas" reveals also a significant effect on the appearance of droplet signatures, as expected: Generally, a high dry gas flow with a gas temperature of $180\,^\circ\,^\circ\mathrm{C}$ reduces the number of detected ion bursts. It is striking that in this experiment a low ion burst frequency appears to be correlated with high TIC and vice versa. The results demonstrate once again that a noticeable superimposed signal drift is occurring: The experiment begins with a dry gas flow of $4.0\,\mathrm{L\,min^{-1}}$ with high TIC intensity while having a low droplet count. At the end of the run, approximately $20\,\mathrm{min}$ later and upon returning to $4.0\,\mathrm{L\,min^{-1}}$, a significantly lower TIC and a higher droplet frequency is recorded. However, there are clearly individual steps in the ion burst frequency, which are correlated with the dry gas flow *changes*. It is thus concluded that the dry gas flow has a pronounced effect on the TIC and ion burst frequency. Even within the limitations of the current experimental setup regarding the long-term stability, a significant ion burst frequency and thus count of droplet signatures, never vanishes, not even with high dry gas flows.

4.5 Conclusions

Time-resolved ion current measurements at the output of the auxiliary SEM detector located downstream of the oa-stage of a Bruker micrOTOF mass spectrometer

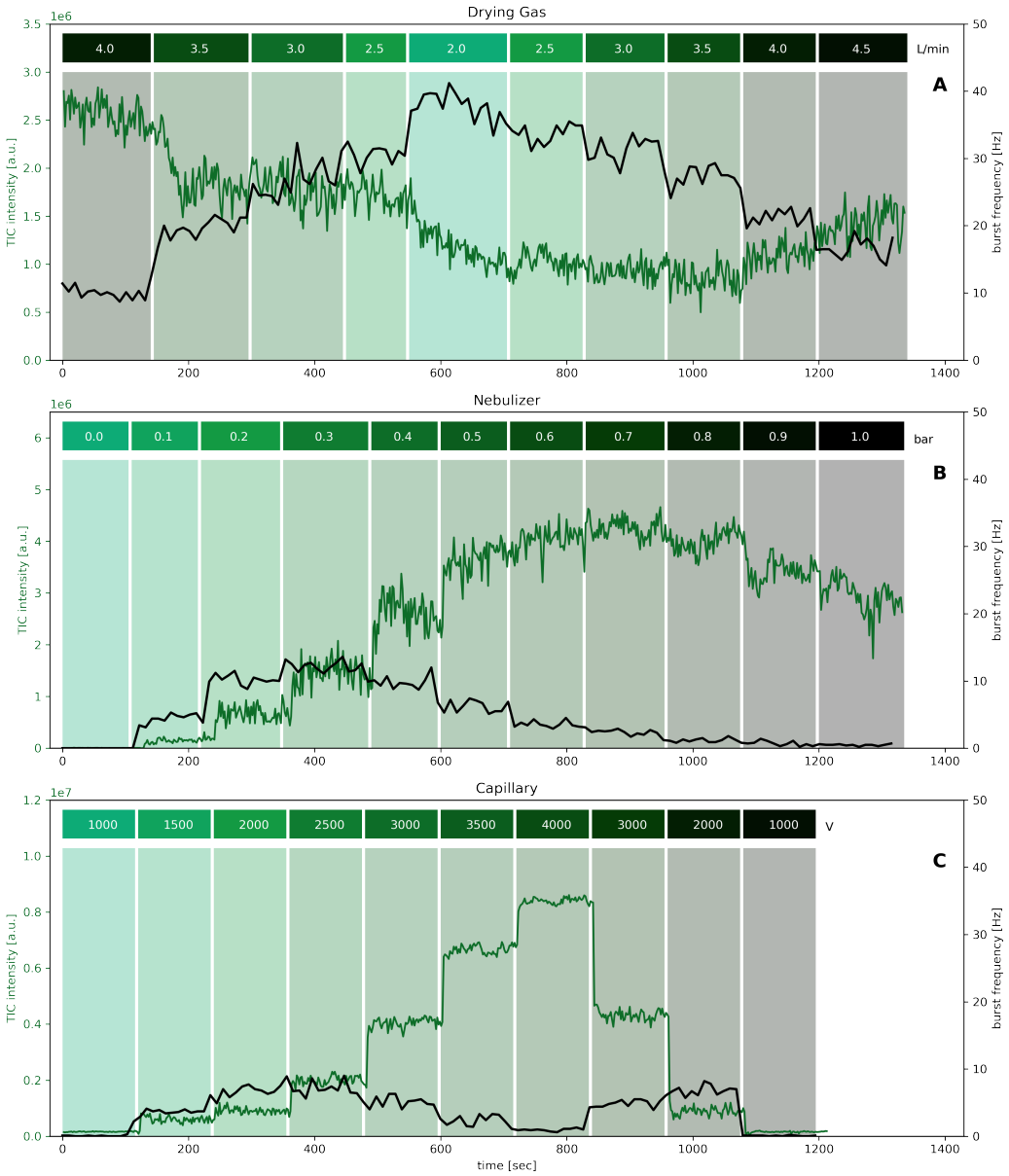

Fig. 4.9: Dependency of ion burst frequency and TIC on variations of (A) the drying gas flow with a dry gas temperature of $180\,^{\circ}\mathrm{C}$, (B) the nebulizer pressure, and (C) the capillary (i.e., spray) voltage. The ion burst frequency shows clear dependence of the varied parameters. However, there is a noticeable shift in the burst frequency when comparing the same frequencies within one measurement. This indicates that there could be an overlaying effect which also influences the burst frequency on a longer time scale.

allowed the direct observation of the stream of charged particles. The observation of ion bursts with orders of magnitude higher intensities than the regular average ion signals suggests the presence of charged droplets containing thousands of analyte ions and charges originating from the electrospray, present in the high-vacuum region of the instrument. However, the observation of pusher blank regions in the ion burst signals indicates that these bursts are not caused by large geometrically confined charged particles, but rather large, partly stratified but still temporally highly correlated clouds of ions. Analysis of the burst pulse widths suggests that the droplet fission event locations vary statistically within the length of the ion transfer stage and that the varied ion source parameters (capillary voltage, drying gas flow, nebulizer gas flow) have no significant effect on the locations of fission.

An unstable electrospray as a possible alternative interpretation of the observed data was also taken into serious consideration. However, the recorded ion bursts are magnitudes larger than the stable background ion current observed with ESI or APCI. This would mean that the electrospray emitter is able to produce signal fluctuations that are also many orders of magnitude larger than the base ion current emitted from the ESI needle. It appears unlikely that such dynamics of the spray are not apparent in the observed ESI current measured by the instrument in the ion source.

Furthermore, the temporal dynamics are in contradiction to the notion that the ion pulses are generated in the atmospheric pressure ion source region: As presented in Figure 4.4 and Figure 4.5, the observed ion burst pulse width distribution reaches from few μs to a few hundred μs. Even if a very intensive ion burst of a few μs width would be generated at the ESI emitter at atmospheric pressure, it should be stratified severely by the interaction with the background gas by diffusion, turbulent mixing due to the gas flow dynamics, and potentially by space charge effects. Thus, we assume that particularly the very sharp transient ion pulses have to be generated at low-pressure conditions with short transfer times to the ion detector.

The spray stability probably has a very strong effect on the size spectrum and generation rate of charged droplets in the atmospheric pressure ion source and is therefore an important parameter to consider in further experiments. However, considering the aspects mentioned above, we conclude that the observed ion bursts most likely originate from aspirated droplets fragmenting in the MS transfer stage.

The presented results strongly motivate further investigation into the charged droplet aspiration dynamics, the mechanism(s) responsible for their fragmentation, and ion burst generation during electrospray ionization. Such efforts are underway using experimental as well as complex modeling approaches.

References

[1] Elias Ahadi and Lars Konermann. „Ejection of solvated ions from electrosprayed methanol/water nanodroplets studied by molecular dynamics simulations“. In: *Journal of the American Chemical Society* 133 (24 June 2011), pp. 9354–9363 (cit. on p. 45).

[2] Bruker Daltonik GmbH. *micrOTOF - micrOTOFcontrol 1.1 - Operator Manual*. May 2005 (cit. on p. 50).

[3] Michel Cloupeau and Bernard Prunet-Foch. „Electrohydrodynamic spraying functioning modes: a critical review“. In: *Journal of Aerosol Science* 25 (6 Sept. 1994), pp. 1021–1036 (cit. on p. 46).

[4] Richard B. Cole. *Electrospray and MALDI Mass Spectrometry*. Ed. by Richard B. Cole. John Wiley & Sons, Inc., Apr. 2010 (cit. on pp. 44, 45).

[5] Richard B. Cole. „Some tenets pertaining to electrospray ionization mass spectrometry“. In: *JOURNAL OF MASS SPECTROMETRY J. Mass Spectrom* 35 (2000), pp. 763–772 (cit. on pp. 44, 45).

[6] Thomas R. Covey, Bruce A. Thomson, and Bradley B. Schneider. „Atmospheric pressure ion sources“. In: *Mass spectrometry reviews* 28.6 (2009), pp. 870–897 (cit. on p. 46).

[7] Christopher D. Daub and Natalie M. Cann. „How are completely desolvated ions produced in electrospray ionization: Insights from molecular dynamics simulations“. In: *Analytical Chemistry* 83 (22 Nov. 2011), pp. 8372–8376 (cit. on pp. 44, 45).

[8] Malcolm Dole, L. L. Mack, R. L. Hines, et al. „Molecular beams of macroions“. In: *The Journal of Chemical Physics* 49 (5 1968), pp. 2240–2249 (cit. on p. 44).

[9] John B. Fenn, Matthias Mann, Chin Kai Meng, Shek Fu Wong, and Craig M. Whitehouse. „Electrospray Ionization for Mass Spectrometry of Large Biomolecules“. In: *Science* 246.4926 (1989), pp. 64–71. eprint: `https://www.science.org/doi/pdf/10.1126/science.2675315` (cit. on p. 44).

[10] M. Gamero-Castaño and J. Fernández De La Mora. „Direct measurement of ion evaporation kinetics from electrified liquid surfaces“. In: *Journal of Chemical Physics* 113 (2 July 2000), pp. 815–832 (cit. on p. 46).

[11] Alfonso M. Ganán-Calvo. „On the general scaling theory for electrospraying“. In: *Journal of Fluid Mechanics* 507 (May 2004), pp. 203–212 (cit. on p. 46).

[12] Alfonso M. Gañán-Calvo, José M. López-Herrera, Miguel A. Herrada, Antonio Ramos, and José M. Montanero. „Review on the physics of electrospray: From electrokinetics to the operating conditions of single and coaxial Taylor cone-jets, and AC electrospray“. In: *Journal of Aerosol Science* 125 (Nov. 2018), pp. 32–56 (cit. on pp. 44, 46).

[13] Marion Girod, Xavier Dagany, Véronique Boutou, et al. „Profiling an electrospray plume by laser-induced fluorescence and Fraunhofer diffraction combined to mass spectrometry: Influence of size and composition of droplets on charge-state distributions of electrosprayed proteins“. In: *Physical Chemistry Chemical Physics* 14 (26 July 2012), pp. 9389–9396 (cit. on p. 45).

[14] Alessandro Gomez and Keqi Tang. „Charge and fission of droplets in electrostatic sprays“. In: *Physics of Fluids* 6 (1 1994), pp. 404–414 (cit. on pp. 45, 46).

[15] J. M. Grace and J. C. M. Marijnissen. „A review of liquid atomization by electrical means“. In: *Journal of Aerosol Science* 25 (6 Sept. 1994), pp. 1005–1019 (cit. on p. 46).

[16] Ronald L. Grimm and J. L. Beauchamp. „Evaporation and discharge dynamics of highly charged droplets of heptane, octane, and p-xylene generated by electrospray ionization“. In: *Analytical Chemistry* 74 (24 Dec. 2002), pp. 6291–6297 (cit. on p. 45).

[17] Jürgen H. Gross. *Mass Spectrometry*. Springer International Publishing, 2017 (cit. on pp. 44–46, 59).

[18] I. Hayati, A. I. Bailey, and Th. F. Tadros. „Investigations into the mechanisms of electrohydrodynamic spraying of liquids“. In: *Journal of Colloid and Interface Science* 117 (1 May 1987), pp. 205–221 (cit. on p. 46).

[19] F. J. Higuera. „Current/flow-rate characteristic of an electrospray with a small meniscus“. In: *Journal of Fluid Mechanics* 513 (Aug. 2004), pp. 239–246 (cit. on p. 46).

[20] Edmond de Hoffmann and Vincent Strootbant. *Mass Spectrometry: Principles and Applications*. 3rd ed. John Wiley & Sons, 2007 (cit. on p. 45).

[21] J. V. Iribarne and B. A. Thomson. „On the evaporation of small ions from charged droplets“. In: *The Journal of Chemical Physics* 64 (6 1976), pp. 2287–2294 (cit. on p. 45).

[22] Yang Kang, Bradley B. Schneider, and Thomas R. Covey. „On the Nature of Mass Spectrometer Analyzer Contamination“. In: *Journal of the American Society for Mass Spectrometry* 28 (11 Nov. 2017), pp. 2384–2392 (cit. on p. 46).

[23] P. Kebarle. *A brief overview of the present status of the mechanisms involved in electrospray mass spectrometry*. 2000 (cit. on pp. 44, 45).

[24] P. Kebarle and M. Peschke. „On the mechanisms by which the charged droplets produced by electrospray lead to gas phase ions“. In: *Analytica Chimica Acta* 406 (2000), pp. 11–35 (cit. on p. 45).

[25] Paul Kebarle and Liang Tang. „From ions in solution to ions in the gas phase - the mechanism of electrospray mass spectrometry“. In: *Analytical Chemistry* 65.22 (1993). PMID: 22881012, 972A–986A (cit. on pp. 44, 46).

[26] Lars Konermann, Elias Ahadi, Antony D. Rodriguez, and Siavash Vahidi. „Unraveling the Mechanism of Electrospray Ionization“. In: *Analytical Chemistry* 85 (1 Jan. 2013). Positioning of charges within droplets, pp. 2–9 (cit. on p. 45).

[27] Clara Markert, Marco Thinius, Laura Lehmann, et al. „Observation of charged droplets from electrospray ionization (ESI) plumes in API mass spectrometers“. In: *Analytical and Bioanalytical Chemistry* 413 (22 Sept. 2021), pp. 5587–5600 (cit. on pp. 45, 46).

[28] J. Fernandez De La Mora. *Electrospray ionization of large multiply charged species proceeds via Dole's charged residue mechanism*. 2000 (cit. on p. 45).

[29] J. Fernandez De La Mora and I G Loscertales. „The current emitted by highly conducting Taylor cones“. In: *J. Fluid Mech* 260 (1994), pp. 155–184 (cit. on pp. 44, 46).

[30] J. Fernandez De La Mora, J Navascues, F Fernandez, and J Rosell-Llompart. „Generation of submicron monodisperse aerosols in electrosprays“. In: *Journal of Aerosol Science* 21 (1990), pp. 673–676 (cit. on pp. 44–46).

[31] Juan Fernández de la Mora. *The fluid dynamics of Taylor Cones*. 2007 (cit. on p. 46).

[32] Lord Rayleigh. „XX. On the equilibrium of liquid conducting masses charged with electricity“. In: *The London, Edinburgh, and Dublin Philosophical Magazine and Journal of Science* 14 (87 Sept. 1882), pp. 184–186 (cit. on p. 44).

[33] James N. Smith, Richard C. Flagan, and J. L. Beauchamp. „Droplet evaporation and discharge dynamics in electrospray ionization“. In: *Journal of Physical Chemistry A* 106 (42 Oct. 2002), pp. 9957–9967 (cit. on p. 45).

[34] Daniel C. Taflin, Timothy L. Ward, and E. James Davis. „Electrified droplet fission and the Rayleigh limit“. In: *Langmuir* 5.2 (1989), pp. 376–384 (cit. on pp. 44, 45).

[35] Andre Venter, Paul E. Sojka, and R. Graham Cooks. „Droplet dynamics and ionization mechanisms in desorption electrospray ionization mass spectrometry“. In: *Analytical Chemistry* 78 (24 Dec. 2006), pp. 8549–8555 (cit. on p. 45).

[36] Arno Wortmann, Anna Kistler-Momotova, Renato Zenobi, et al. „Shrinking Droplets in Electrospray Ionization and Their Influence on Chemical Equilibria“. In: *Journal of the American Society for Mass Spectrometry* 18 (3 Mar. 2007), pp. 385–393 (cit. on p. 45).

5

Influence of Polarity Mode Switching and Standby Times on Signal Stability and Detection of Aspirated Droplet Signatures in Electrospray Mass Spectrometry

Reproduced with permission from: Chris Heintz, Lisa Schnödewind, Oliver Braubach, Hendrik Kersten, Thorsten Benter, Walter Wißdorf. Influence of polarity mode switching and standby times on signal stability and detection of aspirated droplet signatures in electrospray mass spectrometry. International Journal of Mass Spectrometry, Vol. 499, 2024, 117232. https://doi.org/10.1016/j.ijms.2024.117232

5.1 Abstract

Electrospray ionization plays a central role in modern analytical chemistry. It is often used in combination with an HPLC system and is able to transfer large molecules, such as proteins and complexes, into the gas phase. A liquid solution containing the analyte is sprayed in a strong electric field. Charged droplets generated by this process release the analyte molecules which can ultimately be analyzed by the mass spectrometer system. However, the exact mechanisms of droplet generation and ion release are still not fully understood and are under investigation. Recent literature puts the focus on droplet disintegration and shows that the analyte ions are not exclusively released from the droplets within the ionization chamber but rather in the whole mass spectrometer system. Previous experiments allow the direct observation of the signatures of fragmented droplets within the analyzer region of a time-of-flight mass spectrometer: An oscilloscope was connected to a secondary electron multiplier which serves as an auxiliary ion detector, located downstream of the orthogonal acceleration stage of a time-of-flight mass spectrometer. The oscilloscope is thus able to monitor the time-resolved ion current in the mass analyzer region. Pulses of extraordinarily high ion currents are observable here which are attributed to aspirated charged droplets. This work provides insights into long-term experiments

with this experimental setup. There is a focus on signal stability, in the presence of such droplet signatures. It is apparent that the standby time of the instrument between individual measurements and the time since a switch of the polarity mode, has a significant influence on the signal stability. There are also indications that the observations of droplet signatures and the MS signal stability are correlated.

5.2 Introduction

Electrospray Ionization (ESI) has become one of the most frequently used atmospheric pressure ionization (API) techniques in the field of modern mass spectrometry [9, 3, 6, 10, 15, 23]. It is often used in combination with liquid chromatography (LC) systems because of its advantage of being able to transfer relatively large liquid flows to the gas phase and its ability to ionize even large biomolecules [9, 23].

Dole et al. described the first electrospray ionization ion detecting device in 1968 [7]. In the 1980s, Fenn et al. improved the technique and showed the need and the advantages for ESI in such a way, that he was awarded a Nobel Prize in 2002 [9, 8]. Today's general working mechanism of ESI does not differ from the one Dole et al. described in the late 1960s: An analyte-containing solution is being pumped through a thin metal capillary, the so-called *ESI needle*. This needle is a counter electrode to the MS inlet system (e.g. an inlet capillary). Applying a voltage difference of kilovolts to these electrodes leads to a charge separation within the liquid located in the ESI needle which results in the attraction of charges within the liquid towards the inlet system and ultimately in the formation of a so-called *Taylor cone* [15, 21, 30, 4]. The charges at the tip of that cone get closer and coulomb forces increase until they overcome the liquid surface tension. As a result, a spray containing thousands of small charged droplets is released into the ESI source chamber [15, 21, 30, 4].

The initial droplet size for ESI systems is described in the literature for various analyte systems under different conditions [29, 14, 31, 32, 11, 27]. The initial droplet size varies in these measurements between $0.1\,\mu\mathrm{m}$ and up to $100\,\mu\mathrm{m}$ depending on the analyte, the solvent system, the liquid flow rate [27, 26, 23] and other conditions that are difficult to compare like the exact positioning of the ESI needle [5] or other minor factors. It is important to note, that also the inner diameter of the used ESI needle has a strong impact on the initial droplet size and the usage of a nano-ESI source would lead to smaller initial droplets [19]. However, the presented experiments use regular (non nano) ESI. De la Mora et. al. [27] expressed their experimental observation of the dependence of the initial droplet radius a on the experimental parameters liquid flow rate Q, liquid density ρ and its surface tension γ. They discovered an approximate proportionality between the droplet radius and

the mentioned parameters, given by Equation 5.1. It is to be noted that De la Mora et. al. used a simplified setup without a pneumatic-assisted ESI needle, which is in strong contrast to most modern ESI sources.

$$a \sim \left[\frac{\rho Q^2}{2\gamma\pi^2} \right]^{\frac{1}{2}} \tag{5.1}$$

The process of the release of ions from the droplets is intensely discussed in the literature and different models describe how the ions can leave the droplet's surface [24]. Generally, the ion has to overcome the surface tension and adhesive forces of the droplet to leave the surface. This could be the case when solvent molecules evaporate and as a result, the Coulomb forces between the ions overcome the surface tension. This critical limit is often referred to as *Rayleigh limit* and the resultant scenario is called *Coulomb fission* [15, 12, 22, 28]. There is wide consent that the exact mechanism of ion release depends on circumstances like the analyte and solvent system [24, 21, 22]. However, the majority of textbooks and older review articles assume a droplet lifetime of under $1\,\mathrm{ms}$ [17, 3, 15, 1, 22] which means that the majority of ions would be released within the ESI source chamber (as it is depicted in almost every schematic [2, 15, 23]) or in the first elements in the transfer stage leading to bare ions, entering the MS system. Kang et. al. [20] reported in 2017 about accumulated debris on high-vacuum ion optics which can lead to the charging of electrode surfaces and a degradation in the instrument's performance. As a consequence of this, frequent ion path cleaning is unavoidable. Based on this work, we showed earlier [25, 16] that there are large, highly charged droplets containing thousands of analyte molecules that appear to enter the vacuum system of different MS systems: It is possible to directly observe droplet signatures (described in the following) within the mass spectra for example by the examination of non-summed single mass spectra of a TOF instrument[16] or by choosing a suitable m/z scan region for trap devices[25]. This work ties in directly with the work of Heintz et al. [16].

In the previous studies [16], we connected an oscilloscope to an auxiliary secondary electron multiplier (SEM) located downstream of the orthogonal acceleration stage (oa-stage) of a TOF instrument to measure and observe the incoming ion current between the TOF pushes. Figure 5.1 pictures two recorded oscillograms. The sharp peaks occur approximately every $120\,\mu\mathrm{s}$ indicating the TOFs pusher voltage turning on and off again $5\,\mu\mathrm{s}$ later. Panel A shows a typical oscillogram for APCI or APPI with a constant ion current, except for the systematic blank region of $30\,\mu\mathrm{s}$ after the push. In ESI measurements (panel B) occasionally ion bursts occur with orders of magnitudes higher intensity. These bursts are assigned to a very dense cloud of many

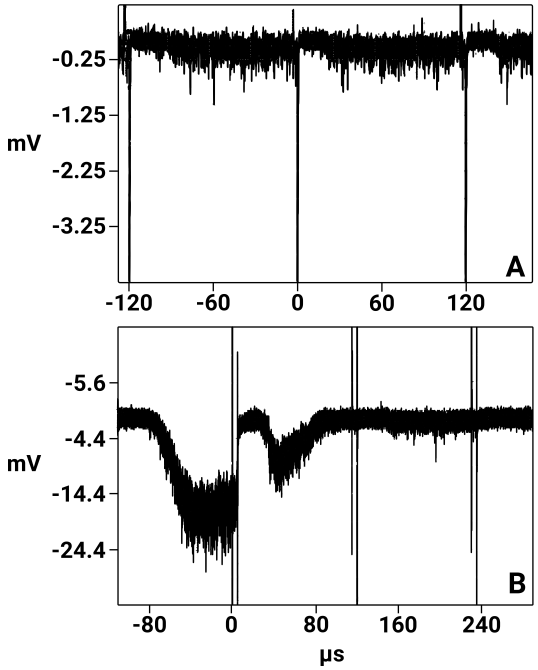

Fig. 5.1: Recorded oscillograms of the auxiliary SEM detector signal. The sharp peaks occurring every $120\,\mu$s show the TOF pusher turning on and $5\,\mu$s later off. After the push, there is a blank region of about $30\,\mu$s while waiting for the ion current to re-arrive at the SEM. Panel A shows a typical oscillogram for APCI or APPI measurements, whereas panel B shows an ion burst, which occurs exclusively in ESI.

charges hitting the SEM. Throughout this manuscript, these ion bursts are called *droplet signatures* due to their assumed origin from a monolithic droplet. Note, that ion burst and droplet signature are handled as synonyms in this article. Moreover, it was observed, that the frequency of droplet signatures occurrence depends, among other things, on the measurement conditions, like gas- and liquid flows, the potential between the ESI needle and inlet system, or the drying gas temperature [16].

Despite the dominance of electrospray as an ionization technique, the exact ion generation mechanism in ESI is still not fully understood and is described as a "black box" and "source of instability" [2, 18]. A stable electrospray is achieved when the Taylor cone is shaped evenly releasing a steady stream of droplets into the ion source chamber [13, 2]. There are different spray modes, described in the literature [13, 15, 18, 2] depending on the electric potential applied to the ESI needle, the solution surface tension, flow rates and conductivity. In general, they can be divided into those with a continuous flow and those with pulsed liquid ejections.

Generating a stable electrospray can be quite challenging keeping in mind, that the variation of one parameter (e.g. voltage between inlet system and ESI needle) forces the change of other parameters (e.g. gas flows) to obtain a stable spray [2].

5.3 Methods

5.3.1 Instrument

A micrOTOF (Bruker Daltonik GmbH, Bremen, Germany) API-TOF-MS with the default Apollo ESI source was used for the experiments. The analyte solution was directly infused mainly via an HPLC pump with a speed of $7\,\mu\mathrm{L\,min^{-1}}$. First experiments were performed with a Fusion 100T syringe pump (Chemyx In, Thermo Fisher Scientific, Waltham, Massachusetts, USA) and a 2.5-mL Hamilton Syringe (Reno, Nevada, USA), also with a direct infusion with a speed of $7\,\mu\mathrm{L\,min^{-1}}$.

Figure 5.2 shows the schematic of the used instrument with its ion path. The operational parameters are described in the following and were set to their default values if not mentioned otherwise. The *nebulizer gas flow* controls the pressure of the used nitrogen gas which flows through the outer hull capillary around the ESI needle and is supposed to support the spray generation. The default value is $0.4\,\mathrm{bar}$ (given as relative excess pressure in reference to the ambient pressure). The potential between the inlet capillary (the MS vacuum inlet) and the ESI needle was set to $-4\,\mathrm{kV}$ in positive ion mode and $4\,\mathrm{kV}$ in negative ion mode. Note that the ESI needle is set to ground in this setup, which allows a simplified safety handling while the measurements. Additionally, there is a *spray shield* which is located in front of the inlet capillary. An electrical offset of $500\,\mathrm{V}$ relative to the capillary tip is applied to this electrode. This results in the formation of an electrostatic lens guiding the ions into the MS system.

To support the evaporation of solvent in the droplets, the instrument uses a stream of heated so-called *drying gas* which counters the flow of ions and charged droplets in the ESI source. The *drying gas temperature* was set to $180\,^{\circ}\mathrm{C}$ and the *drying gas flow* to $4\,\mathrm{L\,min^{-1}}$.

The MS inlet capillary is made of glass while the tips are metal plated. The ions are guided through the inlet capillary by very strong fluid dynamic forces and overcome a repulsive potential applied at the *capillary exit* of $170\,\mathrm{V}$. The transfer stage of the Bruker micrOTOF starts with a skimmer, followed by a hexapole, a second skimmer, and a second hexapole. Both hexapoles are operated in rf-only mode to make them act as focusing ion guides. However, as with every rf-only multipole, both hexapoles have a low-mass cutoff and act like high-pass filters in the setup. The following orthogonal acceleration stage deflects the ion beam into the mass analyzer flight tube in periodic pulses. Between the pulses, the ion current is not deflected and hits the secondary electron multiplier (SEM) which is located downstream of the acceleration stage. Its original purpose is the tuning of transfer parameters. However,

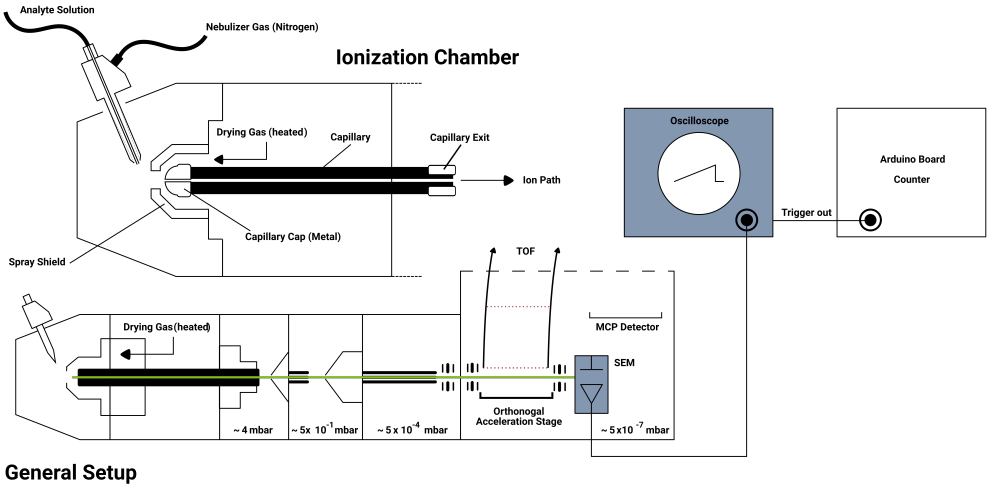

Fig. 5.2: Schematic of the used Bruker micrOTOF. The secondary electron multiplayer is originally intended for transfer stage tuning. However, here it is attached to an oscilloscope to monitor incoming droplet signatures and observe the time-resolved ion current. An Arduino microcontroller is used to count the occurrence of intensive ion pulses generated by aspirated charged droplets.

we attached the SEM to an oscilloscope (RTE 1054, Rhode & Schwarz, Munich, Germany) to observe the time-resolved ion current.

5.3.2 Automation

To perform long-term measurements we wrote pre-defined measurement segments into the XML-based Bruker method files. This makes it possible to conveniently schedule measurement series running for hours and even days. It is possible to set all the software-accessible parameters of the instrument within the segments in the method file. In this work, the polarity was switched alternatingly in the segments. Moreover, the segment duration was varied in different ways.

5.3.3 Chemicals

All measurements were performed with an analyte solution containing reserpine ($\geq 99\,\%$ purity, obtained from Sigma-Aldrich) in a 1:1 mixture of acetonitrile (HPLC-gradient grade, obtained from VWR chemicals) and water with $0.1\,\%$ formic acid ($\geq 98\,\%$ purity, obtained from Sigma-Aldrich). The solution had a concentration of $8\,\mu\mathrm{mol\,L^{-1}}$.

5.4 Results and discussion

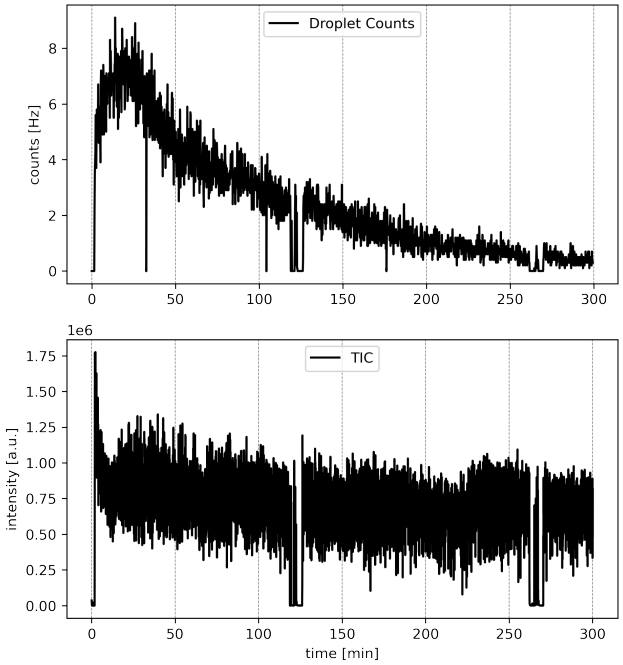

Fig. 5.3: Example of a long-term experiment with approximately $5\,\mathrm{h}$ of runtime, performed with direct infusion of analyte solution via a syringe pump. Dropouts at approximately 2 and 4 hours are the result of refilling the syringe.

5.4.1 Recovery of Total Ion Count as a Function of Instrument Standby Time

Previous experiments [16] with a shorter runtime and variation of some source parameters show, that even when returning to the start parameters within an hour, the measurements show a slightly different total intensity count (TIC), droplet signature occurrence frequency, and specific ion intensity. Figure 5.3 shows the first long-term experiment performed with approximately five hours of runtime. The plot shows a decreasing total signal intensity within the first $30\,\mathrm{min}$ and at the same time an increasing droplet signature occurrence frequency. The latter has its maximum of $8\,\mathrm{Hz}$ at approximately $30\,\mathrm{min}$ and is then decreasing slowly to $0.2\,\mathrm{Hz}$ at the end of the measurement. In contrast to other atmospheric pressure ionization methods, like atmospheric pressure photoionization (APPI) or atmospheric pressure chemical ionization (APCI), the total intensity signal is significantly less stable [16]. There is a significant level of noise in the TIC intensity. The signal drops entirely at approximately 2 and $4\,\mathrm{h}$ are due to the refilling of the used syringe. Later, the setup was changed so that an HPLC system was used instead of a syringe pump to avoid refilling and slight irregularities in the liquid flow.

Figure 5.3 is one example of a couple of similar experiments performed with the same setup. The results were highly reproducible under similar conditions. Inter-

estingly, there is a dependence on the time between the measurements: A second measurement executed shortly after a measurement run would continue the trend of the first measurement and will start with a droplet signature occurrence frequency of around $0.2\,\mathrm{Hz}$. However, an instrument rest/standby time of more than one day or switching the polarity mode recovers the signals to their original state as shown in Figure 5.4.

The TIC intensity is highly influenced by the instrument's standby time, which means the time between two measurements when all ion optic potentials are shut off. As shown in the top panel of Figure 5.4 the TIC intensities behave similarly to the measurement depicted in Figure 5.3 with a syringe refilling after $150\,\mathrm{min}$ and a syringe pump caused baseline shift after $260\,\mathrm{min}$. The central panel shows a measurement on the next day under the same conditions as in the measurement before. Interestingly, there is almost no rise and fall of the TIC intensity but almost immediately a constant intensity. After one week of standby time, the TIC signal is completely recovered as shown in the bottom panel of Figure 5.4.

The following section will go more into detail about a possible mechanism of signal recovery when switching the polarity mode.

5.4.2 Signal recovery after switching the polarity mode

As mentioned above, the total intensity and the droplet signature occurrence frequency intensity recover after more than one day after a measurement. There is also the possibility of a faster recovery by switching the polarity from positive to negative mode and after a few minutes back to positive mode. Similar to the previous experiments, the recovery depends on the duration of being in the switched polarity.

Figure 5.5 shows the dependence of the signal recovery on the duration of switching the polarity. Staying approximately $5\,\mathrm{min}$ in the switched polarity mode leads to a signal recovery of around $80\,\%$, while $1\,\mathrm{min}$ recovers only $50\,\%$ of the original signal intensity.

In the following experiments, the measurement time in the switched polarity mode was systematically reduced from $1\,\mathrm{h}$ to $1\,\mathrm{min}$. Like in the previous measurements, TIC and droplet signature occurrence frequency and the signal of reserpine mono- and dimer were recorded.

Figure 5.6 shows that a longer time in negative measurement mode leads to a more complete recovery of the TIC intensity and a higher droplet signature occurrence

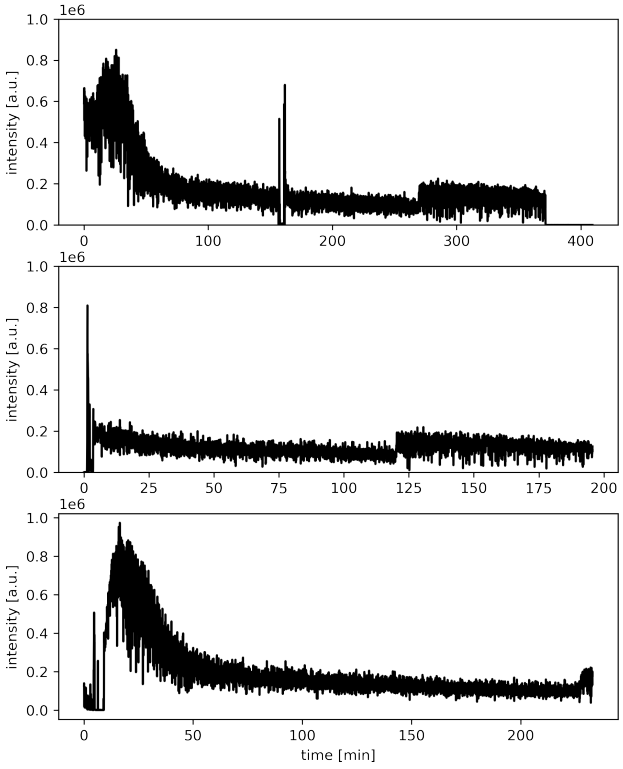

Fig. 5.4: The Standby time of the instrument shows a significant influence on the TIC within a measurement. The top panel shows a long-term measurement over approximately $6\,\mathrm{h}$. The central panel depicts a second measurement under the same conditions as the measurement in the top panel but one day later with no other usage of the instrument in the meantime. A standby time of more than a day recovers the TIC signal completely as shown in the bottom panel. The baseline shift after $260\,\mathrm{min}$ in the top panel, $120\,\mathrm{min}$ in the middle panel, and $230\,\mathrm{min}$ in the bottom panel is caused by the used syringe pump. There is a syringe refilling after $150\,\mathrm{min}$ in the top panel.

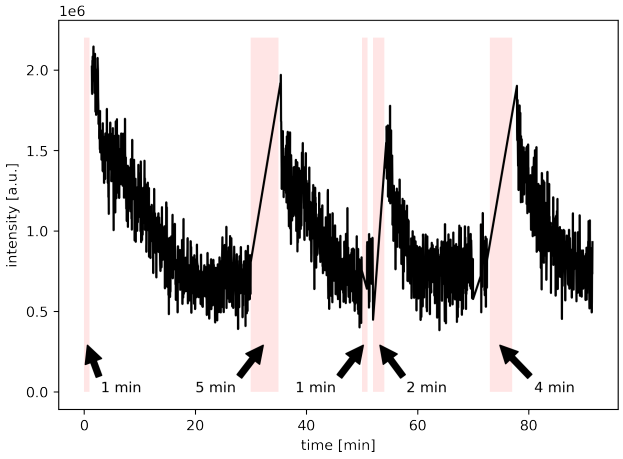

Fig. 5.5: Switching the polarity mode within the measurement to negative mode for different periods shows, that the signal discovery is influenced by the duration of staying in the switched polarity. Negative ion mode is marked as red areas in the plot and the time length of the negative polarity switch is displayed.

Fig. 5.6: Influence of switching the polarity into the negative mode during a measurement with a systematic reduction of the duration in negative mode. The time in negative measurement mode is marked as red areas within the plot. Recorded were the TIC intensity, the droplet signature occurrence frequency and the extracted ion chromatogram (EIC) for reserpine monomer and dimer.

frequency, respectively. The latter is primarily high while the polarity mode is switched, but falls back to its original level after a few minutes. A shorter stay in negative mode cannot compensate for the effect of a decreasing TIC and analyte signal. Interestingly, the signal for the reserpine dimer (bottom panel in Figure 5.6) shows a stronger instability than the monomer signal. However, it is two orders of magnitude less intensive. Even after the first switch to negative ion mode, the signal intensity drops nearly immediately. The signal recovers after a polarity switch, but the shorter the switching time the more incomplete is the signal recovery.

This measurement was repeated several times, also with reversed and random polarity switch times, with almost similar results.

Figure 5.4 and Figure 5.6 show that there must be one unknown factor within the instrument or ESI source that leads to changing conditions for the analyte ions. As a result, there are large fluctuations in the number of analyte ions that reach the detector. In general, the analyte abundance increases within the first $30\,\mathrm{min}$ and then falls off monotonically. Since it is possible to restore the original state by switching the polarity mode or just waiting for a long time it appears likely, that there must be charging of instrument components or surfaces within the instrument while measuring, influencing the ions on its path.

5.4.3 Fast polarity switching

The used Bruker micrOTOF was able to perform a fast polarity switching of alternating $2\,\mathrm{min}$ of each polarity. Figure 5.7 shows an exemplary measurement. Interestingly the TIC and analyte signal remains constant within the observed measurement period. The droplet signature occurrence frequency remains, with one exception, also constant. The reason for the single outbreak of recorded droplet signatures remains unknown so far.

5.4.4 Impact of droplets on signal instability

As we showed in earlier experiments [16], the size and charge of the particles reaching the high-vacuum area vary and probably reach from single ions to large clouds of ions that were released from a former monolithic droplet. The droplet signature occurrence frequency during the long-term measurements suggests that the ion current in the oa-stage is less constant than in other API methods. This is underlined by our previous experiments were we recorded single, non-summated, spectra of both, ESI and APCI, and saw a broad intensity distribution for ESI with very intensive single spectra orders of magnitude higher than the ordinary single

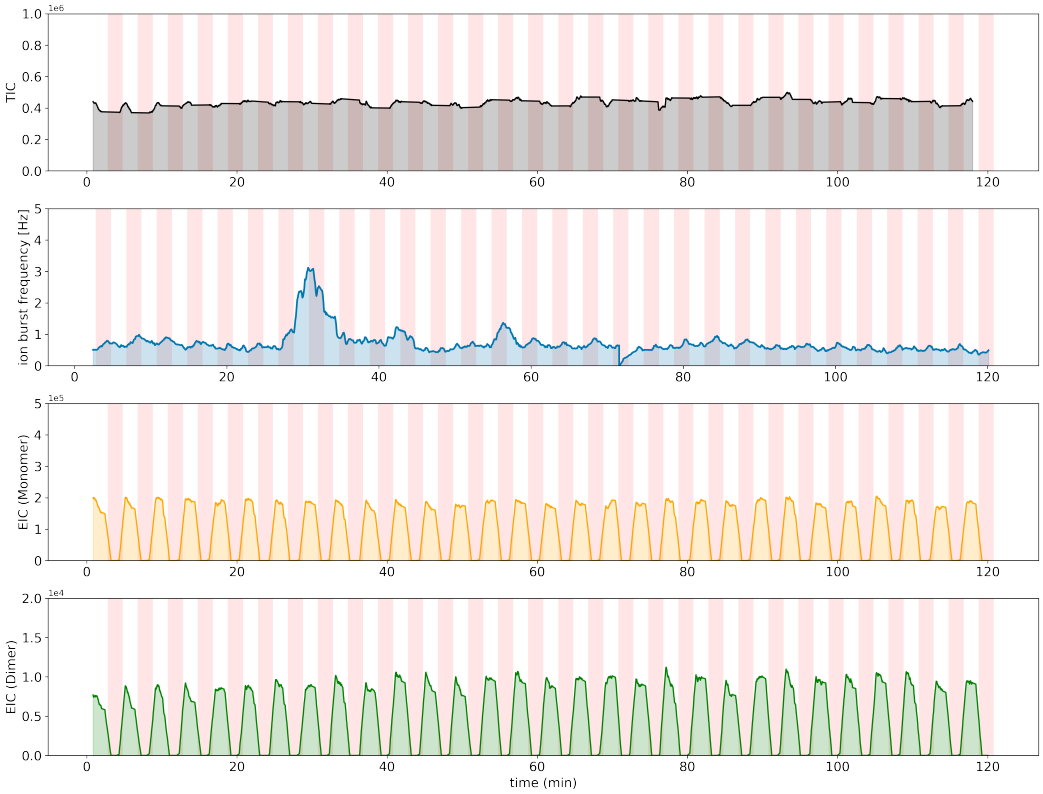

Fig. 5.7: Long-term measurement for two hours with fast polarity mode switching. Every 2 min the polarity mode was switched. The red areas mark negative mode. It was observed that a fast polarity switching results in a more constant analyte signal and droplet signature occurrence frequency.

spectra and a narrower distribution with limited for APCI [16]. Moreover, it is commonly known that the ESI spray tends to have irregularities in its flow, which additionally impacts the occurrence of droplet signatures and ultimately the signal stability [13, 2, 18]. Thus, it is not surprising, that the TIC and analyte signals have more variance in their intensities than in other API ionization methods like APPI or APCI, where the analyte solution is vaporized within the ionization chamber and a more constant flow of ions gets into the MS system.

5.5 Conclusions

This work shows the impact of different sets of parameters on the generation of large, charged droplets penetrating the high-vacuum region of a TOF-MS system and their possible influence on a long-term signal drift. Connecting an oscilloscope to an auxiliary SEM detector downstream of the orthogonal acceleration stage allows direct observation of the time-resolved ion current.

The measurements show that there is a general instability of the analyte signal in the short-term (in contrast to other API methods [16]), which is likely caused by an irregular ion current in the oa-stage due to the occurrence of droplet signatures and an instability in the long-term range in terms of a signal drift. Notably, in the first $30\,\mathrm{min}$ of a new measurement the analyte and droplet signature occurrence frequency is especially unstable. In this context, we noticed a dependence of analyte signal and droplet signature occurrence frequency from the instrument's standby time. The longer the instrument is in standby time, the higher the signal recovery. A standby time of more than one day leads to an almost full signal recovery. This process can be accelerated when switching the polarity mode. We showed, that a polarity switch of approximately $5\,\mathrm{min}$ recovers the signal virtually completely. Thus, fast polarity switching leads to high analyte signal stability and a moderate level of droplet signature appearance.

For this specific type of instrument, all the observed mass signal drifts can be explained by the hypothesis of charging of one or more transfer elements, like the glass inlet capillary. Longer standby periods or switching the polarity mode results in the discharging and the signal recovery. The pivotal observation here is, however, the presence of the observed droplet signatures throughout the long term measurements and their direct dependency on polarity switching. The intensive ion bursts are also believed to be one fundamental reason for an fluctuating analyte signal. Additionally, they potentially also influence the observed charge build-up leading to slow signal drifts, at least with some instrument designs.

References

[1] Andries P. Bruins. „Mechanistic aspects of electrospray ionization“. In: *Journal of Chromatography A* 794 (1998), pp. 345–357 (cit. on p. 67).

[2] Nadja B. Cech and C. G. Enke. „Practical implications of some recent studies in electrospray ionization fundamentals“. In: *Mass Spectrometry Reviews* 20 (6 2001), pp. 362–387 (cit. on pp. 67, 68, 77).

[3] Richard B. Cole. *Electrospray and MALDI Mass Spectrometry*. Ed. by Richard B. Cole. John Wiley & Sons, Inc., Apr. 2010 (cit. on pp. 66, 67).

[4] Richard B. Cole. „Some tenets pertaining to electrospray ionization mass spectrometry“. In: *JOURNAL OF MASS SPECTROMETRY J. Mass Spectrom* 35 (2000), pp. 763–772 (cit. on p. 66).

[5] Terri L. Constantopoulos, George S. Jackson, and Christie G. Enke. „Challenges in achieving a fundamental model for ESI“. In: *Analytica Chimica Acta* 406 (2000) (cit. on p. 66).

[6] Christopher D. Daub and Natalie M. Cann. „How are completely desolvated ions produced in electrospray ionization: Insights from molecular dynamics simulations“. In: *Analytical Chemistry* 83 (22 Nov. 2011), pp. 8372–8376 (cit. on p. 66).

[7] Malcolm Dole, L. L. Mack, R. L. Hines, et al. „Molecular beams of macroions“. In: *The Journal of Chemical Physics* 49 (5 1968), pp. 2240–2249 (cit. on p. 66).

[8] John B. Fenn. „Electrospray Wings for Molecular Elephants (Nobel Lecture)“. In: *Angewandte Chemie International Edition* 42 (33 Aug. 2003), pp. 3871–3894 (cit. on p. 66).

[9] John B. Fenn, Matthias Mann, Chin Kai Meng, Shek Fu Wong, and Craig M. Whitehouse. „Electrospray Ionization for Mass Spectrometry of Large Biomolecules“. In: *Science* 246.4926 (1989), pp. 64–71. eprint: `https://www.science.org/doi/pdf/10.1126/science.2675315` (cit. on p. 66).

[10] Alfonso M. Gañán-Calvo, José M. López-Herrera, Miguel A. Herrada, Antonio Ramos, and José M. Montanero. „Review on the physics of electrospray: From electrokinetics to the operating conditions of single and coaxial Taylor cone-jets, and AC electrospray“. In: *Journal of Aerosol Science* 125 (Nov. 2018), pp. 32–56 (cit. on p. 66).

[11] Marion Girod, Xavier Dagany, Véronique Boutou, et al. „Profiling an electrospray plume by laser-induced fluorescence and Fraunhofer diffraction combined to mass spectrometry: Influence of size and composition of droplets on charge-state distributions of electrosprayed proteins“. In: *Physical Chemistry Chemical Physics* 14 (26 July 2012), pp. 9389–9396 (cit. on p. 66).

[12] Alessandro Gomez and Keqi Tang. „Charge and fission of droplets in electrostatic sprays“. In: *Physics of Fluids* 6 (1 1994), pp. 404–414 (cit. on p. 67).

[13] J. M. Grace and J. C. M. Marijnissen. „A review of liquid atomization by electrical means“. In: *Journal of Aerosol Science* 25 (6 Sept. 1994), pp. 1005–1019 (cit. on pp. 68, 77).

[14] Ronald L. Grimm and J. L. Beauchamp. „Evaporation and discharge dynamics of highly charged droplets of heptane, octane, and p-xylene generated by electrospray ionization“. In: *Analytical Chemistry* 74 (24 Dec. 2002), pp. 6291–6297 (cit. on p. 66).

[15] Jürgen H. Gross. *Mass Spectrometry*. Springer International Publishing, 2017 (cit. on pp. 66–68).

[16] Chris Heintz, Lisa Schnödewind, Oliver Braubach, et al. „Observation of Large, Charged Droplet Signatures within the High-Vacuum Region of a Commercial Electrospray TOF-MS“. In: *Journal of the American Society for Mass Spectrometry* (Feb. 2024) (cit. on pp. 67, 68, 71, 75, 77).

[17] Edmond de Hoffmann and Vincent Strootbant. *Mass Spectrometry: Principles and Applications*. 3rd ed. John Wiley & Sons, 2007 (cit. on p. 67).

[18] R. Juraschek and F.W. Röllgen. „Pulsation phenomena during electrospray ionization“. In: *International Journal of Mass Spectrometry* 177.1 (1998), pp. 1–15 (cit. on pp. 68, 77).

[19] Reinhard Juraschek, Thomas Dülcks, and Michael Karas. „Nanoelectrospray - More than just a minimized-flow electrospray ionization source“. In: *Journal of the American Society for Mass Spectrometry* 10.4 (1999), pp. 300–308. eprint: `https://doi.org/10.1016/S1044-0305(98)00157-3` (cit. on p. 66).

[20] Yang Kang, Bradley B. Schneider, and Thomas R. Covey. „On the Nature of Mass Spectrometer Analyzer Contamination“. In: *Journal of the American Society for Mass Spectrometry* 28 (11 Nov. 2017), pp. 2384–2392 (cit. on p. 67).

[21] P. Kebarle. *A brief overview of the present status of the mechanisms involved in electrospray mass spectrometry*. 2000 (cit. on pp. 66, 67).

[22] P. Kebarle and M. Peschke. „On the mechanisms by which the charged droplets produced by electrospray lead to gas phase ions“. In: *Analytica Chimica Acta* 406 (2000), pp. 11–35 (cit. on p. 67).

[23] Paul Kebarle and Liang Tang. „From ions in solution to ions in the gas phase - the mechanism of electrospray mass spectrometry“. In: *Analytical Chemistry* 65.22 (1993). PMID: 22881012, 972A–986A (cit. on pp. 66, 67).

[24] Lars Konermann, Elias Ahadi, Antony D. Rodriguez, and Siavash Vahidi. „Unraveling the Mechanism of Electrospray Ionization“. In: *Analytical Chemistry* 85 (1 Jan. 2013). Positioning of charges within droplets, pp. 2–9 (cit. on p. 67).

[25] Clara Markert, Marco Thinius, Laura Lehmann, et al. „Observation of charged droplets from electrospray ionization (ESI) plumes in API mass spectrometers“. In: *Analytical and Bioanalytical Chemistry* 413 (22 Sept. 2021), pp. 5587–5600 (cit. on p. 67).

[26] J. Fernandez De La Mora and I G Loscertales. „The current emitted by highly conducting Taylor cones“. In: *J. Fluid Mech* 260 (1994), pp. 155–184 (cit. on p. 66).

[27] J. Fernandez De La Mora, J Navascues, F Fernandez, and J Rosell-Llompart. „Generation of submicron monodisperse aerosols in electrosprays“. In: *Journal of Aerosol Science* 21 (1990), pp. 673–676 (cit. on p. 66).

[28] Lord Rayleigh. „XX. On the equilibrium of liquid conducting masses charged with electricity“. In: *The London, Edinburgh, and Dublin Philosophical Magazine and Journal of Science* 14 (87 Sept. 1882), pp. 184–186 (cit. on p. 67).

[29] James N. Smith, Richard C. Flagan, and J. L. Beauchamp. „Droplet evaporation and discharge dynamics in electrospray ionization“. In: *Journal of Physical Chemistry A* 106 (42 Oct. 2002), pp. 9957–9967 (cit. on p. 66).

[30] Daniel C. Taflin, Timothy L. Ward, and E. James Davis. „Electrified droplet fission and the Rayleigh limit“. In: *Langmuir* 5.2 (1989), pp. 376–384 (cit. on p. 66).

[31] Andre Venter, Paul E. Sojka, and R. Graham Cooks. „Droplet dynamics and ionization mechanisms in desorption electrospray ionization mass spectrometry“. In: *Analytical Chemistry* 78 (24 Dec. 2006), pp. 8549–8555 (cit. on p. 66).

[32] Arno Wortmann, Anna Kistler-Momotova, Renato Zenobi, et al. „Shrinking Droplets in Electrospray Ionization and Their Influence on Chemical Equilibria“. In: *Journal of the American Society for Mass Spectrometry* 18 (3 Mar. 2007), pp. 385–393 (cit. on p. 66).

6

Signatures of Charged Droplets from ESI: A Statistical Analysis of Non-Summed Mass Spectra Compared to APCI

Reproduced with permission from: Chris Heintz, Hendrik Kersten, Thorsten Benter, et al. Signatures of Charged Droplets from ESI: A Statistical Analysis of Non-summed Mass Spectra Compared to APCI. Journal of the American Society for Mass Spectrometry, 2025, 36(4), https://doi.org/10.1021/jasms.4c00508.

6.1 Abstract

Electrospray ionization (ESI) is the most widely used technique for the ionization of liquid samples, for example, from liquid chromatography (LC) coupled to mass spectrometry. Recent experiments demonstrate the penetration of charged droplets or at least large clusters into the high-vacuum region of different ESI mass spectrometers. Using a Bruker micrOTOF equipped with a standard Bruker Apollo ESI source, we demonstrated that time-of-flight (TOF) MS can detect signatures of these droplets by analyzing the statistics of individual TOF spectra, resulting from a single orthogonal acceleration (oa) stage pulse. A custom experimental setup allows additional online monitoring of the ion current in the oa-stage by coupling an oscilloscope to an auxiliary secondary electron multiplier (SEM). The results obtained with ESI are compared to mass spectra recorded under similar conditions using atmospheric pressure chemical ionization (APCI).

Our findings reveal that the observation of droplet signatures is unique to the ESI process, with their frequency and intensity strongly determined by the ion source settings. We also report that the majority of the individual spectra obtained do not contain ion signals. The observed intensity in the summed spectra stems from a few very intense spectra, which result from single droplet fragment bursts. In contrast, APCI provides an almost continuous and stable ion current, without intense signal bursts characteristic for ESI. Additional optical monitoring strongly suggests

that these signatures are not a result of spray instability, but are common even for undisturbed, continuous spray operation. The variation of ion source parameters shows that specific capillary voltages, nebulizer pressures, and dry gas flows lead to an increase in the frequency of droplet occurrence. Since these parameters are fundamental and frequently altered in analytical measurements, the results reported in this contribution underscore the significance of understanding droplet dynamics in ESI-MS and provide insights regarding droplets affecting the ESI signal intensity recorded in analytical runs.

6.2 Introduction

Electrospray ionization (ESI) is the most widely used technique for coupling high-pressure liquid chromatography (HPLC), or analyzing liquid samples in general, with a mass spectrometer (MS) [6, 2, 5, 7, 10, 19]. There are different variations of ESI setups, but all consist essentially of a capillary with a diameter of approximately $0.2\,\mathrm{mm}$ [10] through which the liquid analyte solution is pumped. The liquid flow rate depends on the application and the respective configuration of the ESI source and is mainly in the range of 10 to $200\,\mu\mathrm{L\,min^{-1}}$ for a pneumatically assisted spray source [10]. A potential difference of several thousand volts is applied between the ESI needle and the MS entrance, resulting in a strong electrical field that leads to charge separation within the liquid inducing the ESI current and ultimately to the formation of the so-called Taylor cone [10, 17, 29, 3]. In most cases, including this study, the sprays are pneumatically assisted. Specifically, an outer tube surrounding the ESI capillary directs a gas flow (e.g. nitrogen) around the capillary tip, supporting the generation of a plume of small charged droplets. [10]. The initial size of these droplets is described in the literature for different ESI configurations, experimental conditions, and analyte systems to range between $0.1\,\mu\mathrm{m}$ and up to $100\,\mu\mathrm{m}$ [23, 28, 9, 30, 31, 8, 22]. The inner diameter of the ESI capillary significantly impacts the size of these initial droplets [16]. As a result, nano-ESI causes the initial droplets to be orders of magnitude smaller than for standard ESI [27]. The ESI process comprises three major steps:

1. At the tip of the Taylor cone, Coulomb forces between equally charged ions exceed the liquid surface tension, causing charged droplets to be released from the ESI capillary into the ionization chamber. [13, 26, 10]

2. The droplets shrink in size as the solvent evaporates, leading to an increase in charge density. Eventually, Coulomb forces surpass the droplet's surface tension, triggering a Coulomb explosion that fragments the droplets into smaller offspring droplets.[6, 22, 24, 10]

3. As the process continues, after several cycles, the smaller droplets eventually release bare ions. [10, 32, 17, 29, 3]

This overall process is supported by numerous experimental results and is well established in textbooks. [10, 32, 17, 29, 3, 13, 26, 22, 24] This study focuses primarily on the second and third step of the process. The presence of a droplet shrinkage mechanism and the release of bare ions are supported by their detection in the mass spectra. The question though is **where** and **when** do the final cycles of droplet fragmentation occur, and what are the typical products of such fragmentation?

In previous work [11, 12, 21, 15], we demonstrated the presence of droplets and/or droplets debris in the high-vacuum stage of different mass spectrometers. The results indicate that large clouds of ions and small molecular clusters of unknown composition are present in the vacuum system. We will refer to these as droplet signatures, droplet debris, or ion bursts in the following. There is evidence that initially formed droplets survive the spray chamber having a proposed lifetime of about $1\,\mathrm{ms}$ [14, 2, 10, 1, 18] within the ionization chamber resulting in a droplets' penetration into the vacuum stages. It was shown that source parameters such as the flow rate of the nebulizer gas, drying gas or sprayed liquid, or the capillary voltages influence the frequency of occurrence of droplet debris/ion bursts. [11] Additionally, long-term experiments examine the effects of polarity mode switching during the experiment and its impact on the long-term stability of the analytical signal and the total ion current (TIC). [12] Both works show significant impacts of the investigated parameters on the observation of droplet signatures. Parameters which are particularly crucial for the generation of a stable spray influence the droplet signature occurrence the most (e.g., nebulizer pressure, capillary voltage, dry gas flow, etc.). During long-term experiments, we observed a decrease in the occurrence of the droplet signature, which increases abruptly after the polarity mode is switched and then decreases again. A similar effect is observed after a long instrument's standby time with switched-off high-voltages.

Rajkovic et al. [25] present simulations of fragmentation steps by surface-induced dissociation (SID) of aspirated clusters and small droplets, which provide a rational explanation for the occurrence of droplet debris. This mechanism may also be responsible for the contamination observed on electrodes in the high-vacuum region, as described by Covey et al. [4]. Such contamination results in increased maintenance frequency and thus, higher operational costs.

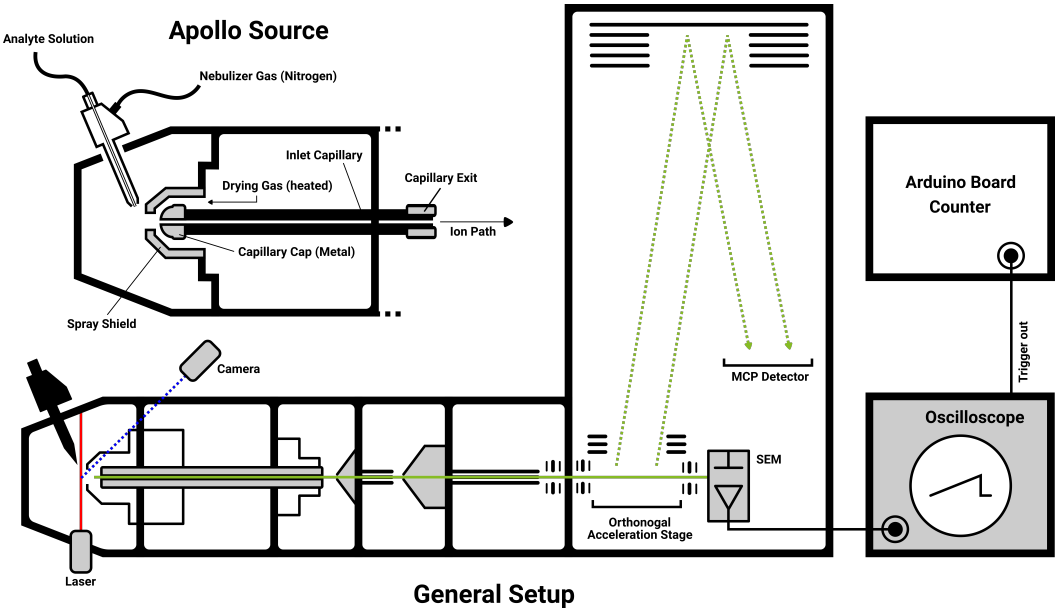

Fig. 6.1: Schematic of the experimental configuration with a detailed drawing of the used Bruker Apollo ionization chamber. The laser module, the USB camera used for the optical spray observation and the oscilloscope connected to the auxiliary SEM detector are also shown.

6.2.1 Individual (raw) mass spectra

A time-of-flight (TOF) instrument typically records 10,000 spectra per second. [10] These single spectra are accumulated before data transfer to the computer resulting in an acquisition frequency of, e.g. 1 Hz significantly reducing the amount of data to be processed and enhancing the signal-to-noise ratio. [10] In our previous work [11], we demonstrated that for certain instruments it is possible to record the non-accumulated mass spectra (resulting from individual orthogonal acceleration stage pulses) which we will hereafter refer to as raw spectra or single spectra.

6.3 Methods

6.3.1 Instrument

All experiments were performed with a Bruker micrOTOF (Bruker Daltonik GmbH, Bremen, Germany). The instrument was equipped with a standard Bruker Apollo ESI source or a standard Bruker Apollo APCI source, respectively. The electrospray was generated using a stainless steel ESI capillary for analyte solution infusion and a surrounding outer tube through which a nebulizer gas (in this case, nitrogen) was passed.

Tab. 6.1: Operating parameters used for ESI and APCI experiments if not declared otherwise

Parameter	ESI (pos.)	ESI (neg.)	APCI (pos.)	APCI (neg.)
Liquid Flow in $\frac{\mu L}{min}$	10	10	10	10
Inlet capillary voltage in V	-4000	+4200	-4200	+4200
Nebulizer pressure in bar	0.4	0.4	0.4	0.4
Dry gas flow in $\frac{L}{min}$	4	4	5	5
Dry gas temperature in $°C$	180	180	200	200
Vaporizer temperature $°C$	-	-	430	430

The inlet capillary has a length of $18\,\mathrm{cm}$ and an inner diameter of $0.5\,\mathrm{mm}$. The operating parameters are displayed in Table 6.1 and were used if not declared otherwise.

As depicted in Figure 6.1, the Bruker micrOTOF features a transfer stage containing a skimmer downstream of the inlet capillary, followed by a transfer hexapole, a second skimmer, an additional hexapole, and a final lens stack before the ions enter the orthogonal acceleration (oa) stage. Both hexapoles are operated in radio frequency (rf) only mode, functioning as high-pass filters in this configuration. The instrument is equipped with a discrete conversion dynode/secondary electron multiplier device (SEM) positioned behind the oa-stage, allowing on-axis charge detection. This SEM, originally implemented for instrument tuning purposes, was connected to an oscilloscope (RTE 1054, Rhode & Schwarz, Munich, Germany) to observe the time-resolved ion current between oa-stage pulses. This enables the recording of droplet signatures. Additionally, an Arduino Uno microcontroller (Arduino DUE R3, Arduino, Ivrea, Turin, Italy) recorded the frequency or timestamps, respectively, of ion bursts hitting the SEM.

6.3.2 Automation

Predefined acquisition segments of specific periods and instrument parameters were written into the XML-based method files used by the Bruker instrument control software to conduct automated acquisitions with reproducible conditions. All instrument parameters accessible through the software are configured in the segments of the method file. Each automated data acquisition cycle in this study consisted of eight segments, with variations of one of the following parameters: capillary voltage, nebulizer pressure, and drying gas flow. All experiments were conducted in both ESI and APCI modes and were replicated three times to assess experimental uncertainty.

6.3.3 Observation of Spray Stability

The spray stability was monitored by optically observing the spray plume shape to support our hypothesis that droplet debris signals are not a result of an unstable spray. Consequently, a USB camera module (TX-158, Technaxx Deutschland GmbH und Co.KG, Schöneck, Germany) was placed inside the Apollo ion source. Furthermore, a laser module (LFD650-1-12(9x20), PICOTRONIC GmbH, Koblenz, Germany) was positioned below the ion source chamber, with its beam directed through a cylindrical lens and an additional window in the ion source enclosure to create a laser sheet that illuminates the cross-section of the spray. The camera captured images of the spray at a frequency of $1\,\mathrm{Hz}$. The image capture time was synchronized with the data acquisition timeline during post-processing. Images were adjusted for saturation, contrast, and cropping, as illustrated in Figure 6.2. This procedure allows the quantification of the spray cross-sectional area by calculating the ratio of illuminated (red) pixels to the total number of pixels in the observed area. This calculated value is referred to as the "spray area ratio", which serves as an indicator of the spray condition.

6.3.4 Chemicals

Reserpine (crystalline, $\geq 99.0\,\%$ HPLC grade from Sigma Aldrich) was used as an analyte. Reserpine is a well-known analytical calibration standard for LC-MS systems [20] and was used in previous studies [11, 12, 21]. It was prepared as a 1:1 solution of acetonitrile (HPLC-gradient grade, obtained from VWR chemicals) and water with $0.1\,\%$ formic acid ($\geq 98\,\%$ purity, obtained from Sigma-Aldrich) added and had a concentration of $8\,\mu\mathrm{mol\,L^{-1}}$.

Due to the storage of the solution in a glass vessel, the reserpine-sodium adduct was increasingly observed over time.

6.3.5 Observation of Droplet Signatures

Figure 6.3 shows an exemplary oscillogram recorded with the SEM using the aforementioned experimental arrangement. The highly intense and sharp transient signals (marked with (A) in the figure) result from crosstalk caused by the high-voltage pulse for pusher activation or deactivation, respectively, to the amplifier electronics of the SEM. The delay, corresponding to the horizontal distance in the oscillogram, between the two signals is exactly $5\,\mu\mathrm{s}$, which is the pusher on time. The delay between the pulse pairs resembles the entire push or acquisition cycle, respectively, and results from the selected m/z window to be recorded. A larger m/z window

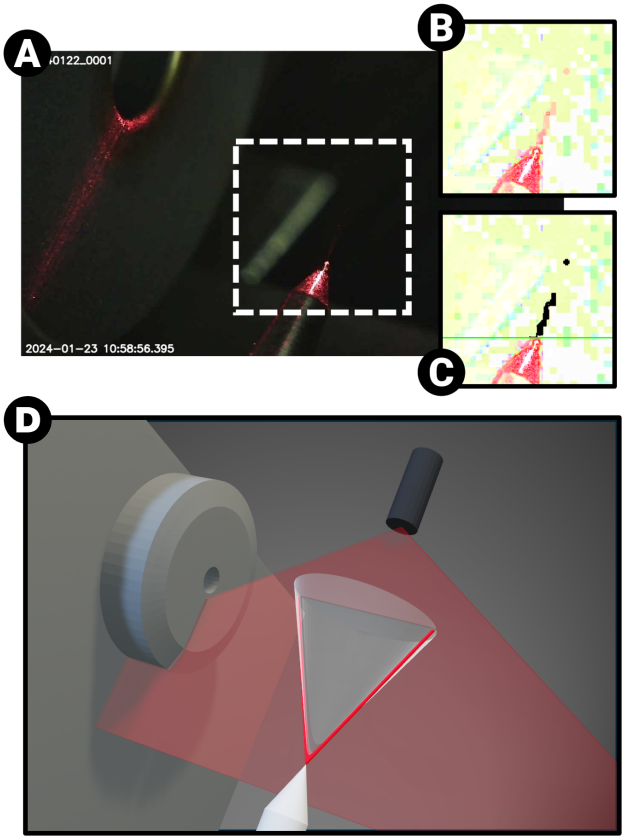

Fig. 6.2: A is the unedited photo recorded with the USB camera module placed diagonally at the top of the ion source chamber. The spray was illuminated with a laser beam directed through a cylindrical lens to fan out the beam. Due to the positioning of the camera module, the image is tilted since the spray needle tip is positioned at the chamber's top and sticks out vertically. The relationship between the laser module, spray tip, and spray shield is displayed in a 3D model in panel D. The white dashed box indicates the image section used for further processing. B is the cropped photo with saturation, brightness, and contrast adjustments. C illustrates the calculation of the spray area: Only the reddish pixels above the green line were counted to prevent the inclusion of red pixels from the spray tip. All considered pixels are represented as black pixels in panel C. The ratio between reddish and the total amount of pixels was calculated and called the "spray area ratio".

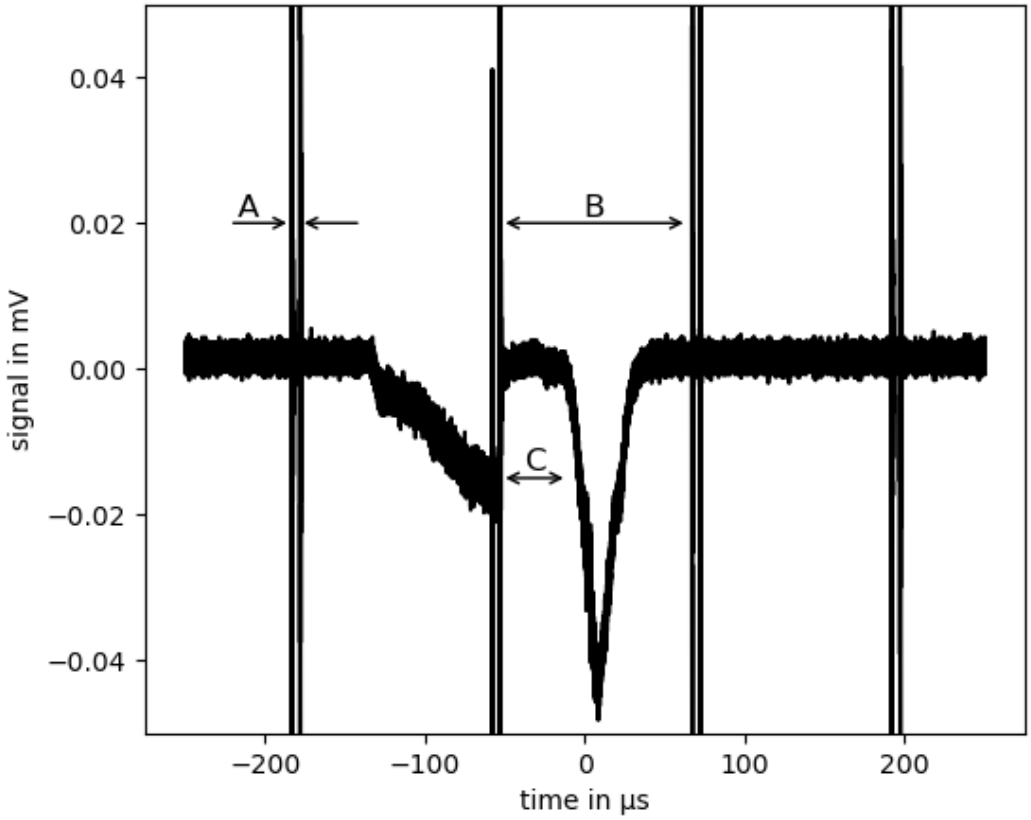

Fig. 6.3: Exemplary oscillogram of five oa-stage pulse cycles recorded by the SEM shown in Figure 6.1. One cycle (B) has a duration of about $100\,\mu$s. Massive ion burst signals are observed in the second and third cycles. They are "punched" by the oa-stage pulse orthogonally pushing ions from the ion current into the flight tube, resulting in a blank region (C) in the SEM signal of about. This blank space right after the two sharp peaks represents the time it takes for the ions, after the punching caused by the pusher, to reach the SEM again. The push event is visible as two sharp peaks (A) with an interval of $5\,\mu$s.

leads to a larger distance between the oa-stage pulses. The m/z window was set between m/z 50 and 6,000 in Figure 6.3, which results in an acquisition cycle of approx. $100\,\mu$s, marked with (B) in the figure.

Connecting the SEM to an oscilloscope enables time-resolved ion current recording. The signal between the sharp pulse pairs from the oa-stage pulse corresponds to the number of secondary electrons or ions striking the SEM, respectively. The observed signals (given in mV) are negative due to the negative charge of the secondary electrons. In the case of atmospheric pressure photoionization (APPI) and atmospheric pressure chemical ionization (APCI), there is continuous ion flow and only a small signal slightly above the electrical noise is observed [11]. In contrast, massive ion bursts are recorded with an ESI source. Figure 6.3 shows a typical example of such a signal burst in the second and third cycle. Switching off the ESI capillary voltage leads to the immediate elimination of ion bursts. There is a time interval of approximately $40\,\mu$s right after the sharp pulse pair structure where no ions reach the SEM, resulting in a blank region, marked with (C) in the figure. As discussed, this is caused by the orthogonal push of all ions into the flight tube, temporarily preventing the ions from reaching the SEM. After the push pulse, ions reach the SEM again at about $40\,\mu$s. Furthermore, the exemplary oscillogram in 6.3 demonstrates that the signal corresponds to a dense cloud of ions, rather than a monolithic particle, as the pusher punches out a segment of the cloud.

Ion bursts of varying lengths and intensities are observed in oscillograms with frequencies ranging from 0.2 to $10\,\mathrm{Hz}$. As mentioned above, it was demonstrated in earlier studies [12] that these intense bursts are observed only with ESI. In contrast, APPI and APCI are characterized by a rather stable ion current without showing any high-intensity signal bursts.

We configured the oscilloscope to trigger on ion burst signals using a custom trigger sequence to avoid triggering on every crosstalk pulse from the pusher. The absolute number of detected ion bursts is strongly influenced by the trigger level, as a higher trigger level will exclude less intense ion bursts from being counted. When required, the oscilloscope can also record the characteristic waveform for a specific ion burst, but it requires approximately $4\,\mathrm{s}$ to save one waveform; during this time, the instrument cannot detect any further ion bursts. The aforementioned Arduino controller was used for data recording, as previously described.

6.4 Results and Discussion

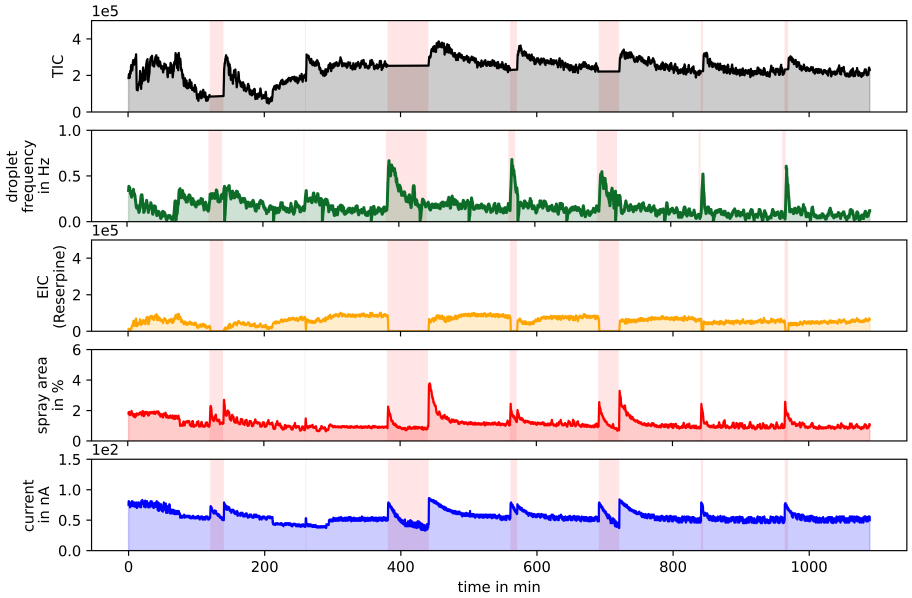

Fig. 6.4: The chromatogram of a long-term Reserpine experiment with alternating polarity switching displays several ESI key parameters over time, including the total ion current (TIC) in black, and the droplet signature occurrence frequency in green. The latter was calculated from the number of ion bursts received with the oscilloscope, which was connected to the auxiliary SEM, the extracted ion chromatogram (EIC) for Reserpine in yellow, the spray cross-section area derived from the camera recordings in red, and the measured ion current within the ionization chamber in both positive and negative modes in blue. A blue background indicates the negative acquisition mode.

6.4.1 Transient Spray Phenomena Induced by Polarity Switches

The experimental configuration allows intercorrelating multiple operational key parameters of the electrospray for example the observation of the spray stability and changes of the spray dynamics focusing on different diagnostic aspects enabled by the optical monitoring of the spray. The first panel of Figure 6.4 shows the total ion current (TIC) plotted against time. The second panel displays the observed droplet signature/ion burst occurrence frequency, recorded with the auxiliary SEM, as previously described. This droplet/burst frequency signal results from the oscilloscope detecting and counting the incoming ion bursts. Hence, the displayed droplet frequency is not to be confused with the mass spectra frequency of the TOF. The third panel shows the extracted ion chromatogram (EIC) for Reserpine. The fourth and fifth panels present the cross-sectional area of the spray, observed with the optical setup as detailed in Figure 6.2, and the ESI ion current recorded with the mass spectrometer between the ESI needle and the inlet capillary, respectively. Despite the rather low image resolution, Figure 6.4 demonstrates a qualitative correlation between the spray area and the ion current. Moreover, the figure shows

that droplet signatures consistently appear. Regardless of the spray conditions, the droplet frequency never reaches zero, as displayed in the green panel of Figure 6.4. This suggests that droplet signatures are likely not caused by transient spray instabilities but persist during stable spray conditions. In addition, the settings were selected so that only relatively intense ion bursts triggered the oscilloscope, ensuring that background noise was not interfering. As a result, the actual rate of ion bursts including ion burst events with lower intensity was higher than the recorded frequency.

Note that Figure 6.4 is in fact a reproduction of a measurement method used in earlier work [11], which fits well to examine the spray stability. There are additional effects induced by a polarity switch, such as an increase in the frequency of the occurrence of the droplet signature, as described in the introduction [11].

6.4.2 Raw Spectra in Dependence of ESI Source Parameters

Three experiments were conducted to investigate the dependence of single spectra on key operational ESI source parameters: (I) the capillary voltage between the inlet capillary and the ESI needle, (II) the pressure of the nebulizer gas, and (III) the dry gas flow. An automated method was developed with acquisition segments of three minutes each, incorporating eight variations for one of the three ion source parameters. All experiments were replicated three times to assess the uncertainty of the results. The experimental series was also performed with APCI under similar conditions as a reference.

Figure 6.5 illustrates the results for changing capillary voltages. The top panel displays a chromatogram with eight acquisition segments, each lasting $3\,\mathrm{min}$, including the corresponding capillary voltage. Each pulse in the chromatogram represents the intensity of a single spectrum, with some isolated spectra notably standing out due to their high intensity. In contrast, Figure 6.6 presents the experimental results using APCI. Significant differences in the intensity distribution are evident, as seen in the comparison of both chromatograms: The APCI chromatogram exhibits rather uniform intensities of the single spectra.

The distribution of the total intensities of the raw spectra is displayed in one histogram per section in Figure 6.5 and Figure 6.6 to assess the effect of the varied parameter on the total intensity distribution. The histograms confirm the conclusions drawn upon inspecting the chromatograms: In ESI mode, there is generally a broad intensity distribution with some spectra having total intensities of more than 25,000 counts, whereas the APCI histograms are limited to a maximum of approximately

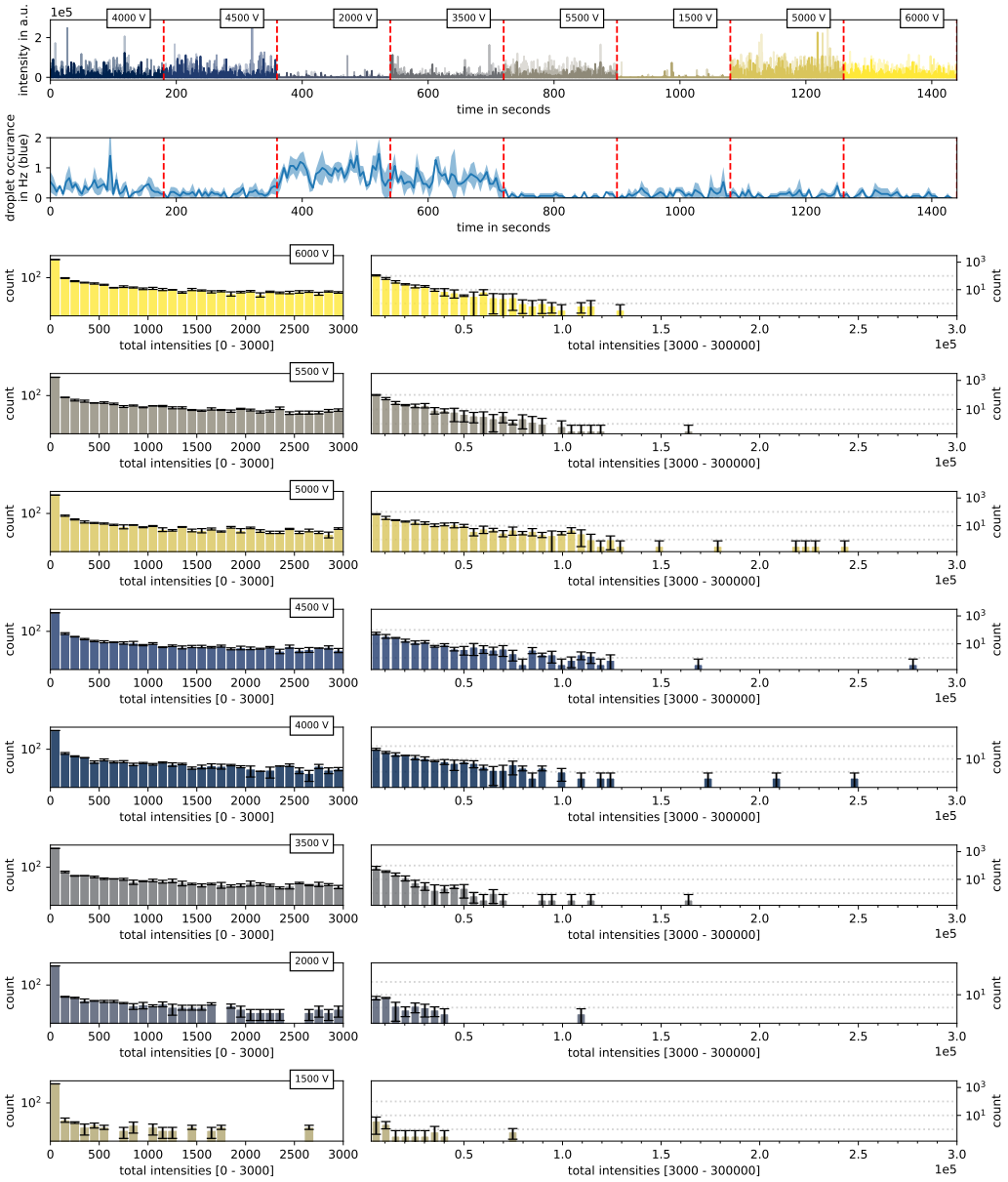

Fig. 6.5: Histograms of the intensity distribution of single spectra at various capillary voltages in ESI mode. The top panel provides an overview chromatogram, while the second panel shows the droplet signature occurrence frequency. The values represent the mean of three recordings, with error bars indicating the standard error of the mean. The histograms in the left column illustrate the intensity distribution for spectra with total intensities below 3,000 counts, while the right-hand histograms display the corresponding distribution for intensities between 3,000 and 300,000 counts. Note that the histogram bins are different: Each bar in the left histograms represents intensities within a range of 100 counts, while the bars in the right histogram cover a range of 5,000 counts. The counts are displayed on a logarithmic scale.

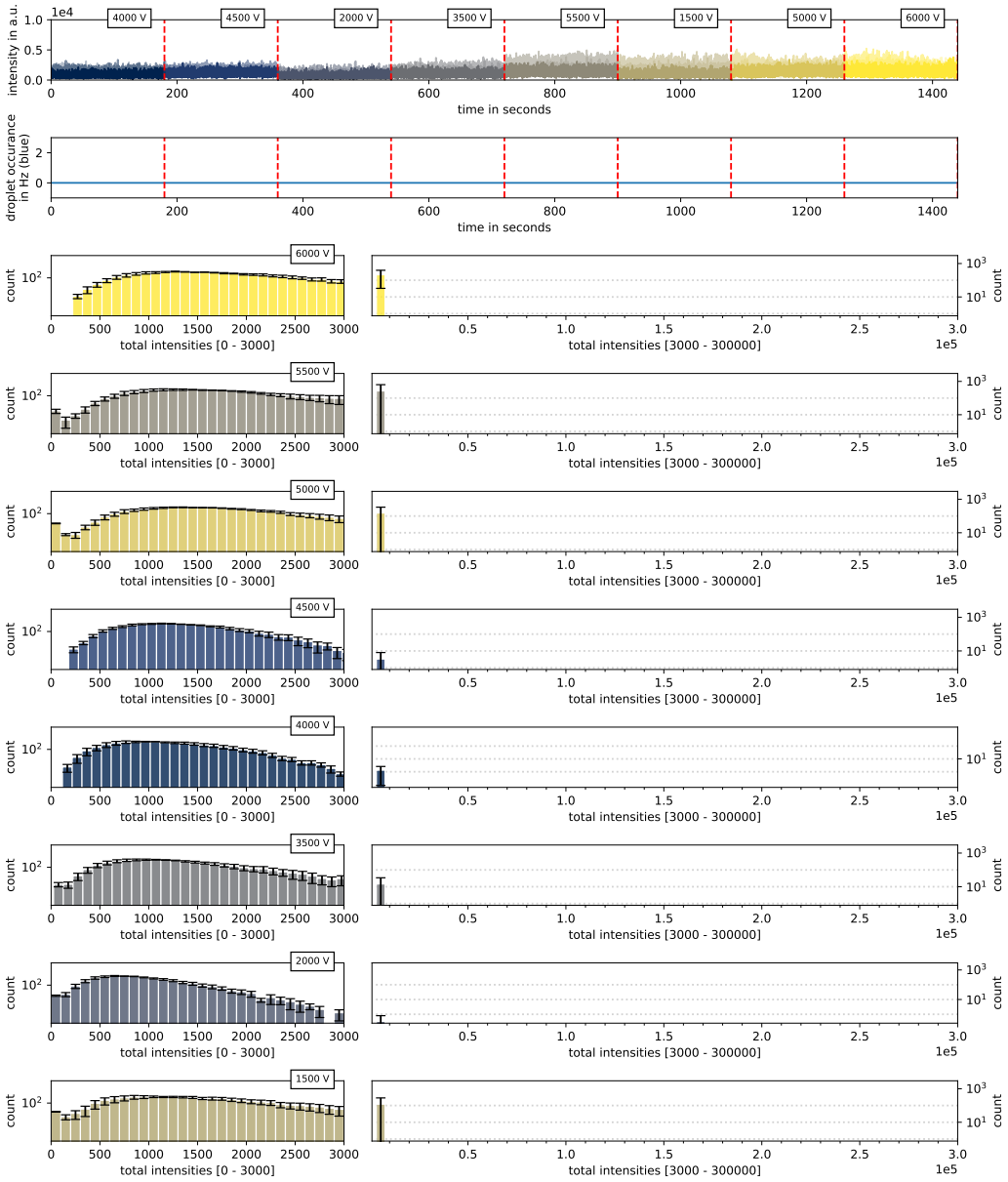

Fig. 6.6: Histograms of the intensity distribution of single spectra at various capillary voltages in APCI mode, analogous to Figure 6.5. The top panel provides an overview chromatogram, while the second panel shows the droplet signature occurrence frequency. The values represent the mean of replicate experiments, with error bars indicating the standard error of the mean. The histograms in the left column illustrate the intensity distribution for spectra with total intensities below 3,000 counts, while the right-side histograms display the distribution for intensities between 3,000 and 300,000 counts. Each bar in the left histogram represents a range of 100 counts, while the bars in the right histogram cover a range of 5,000 counts. Counts are displayed on a logarithmic scale.

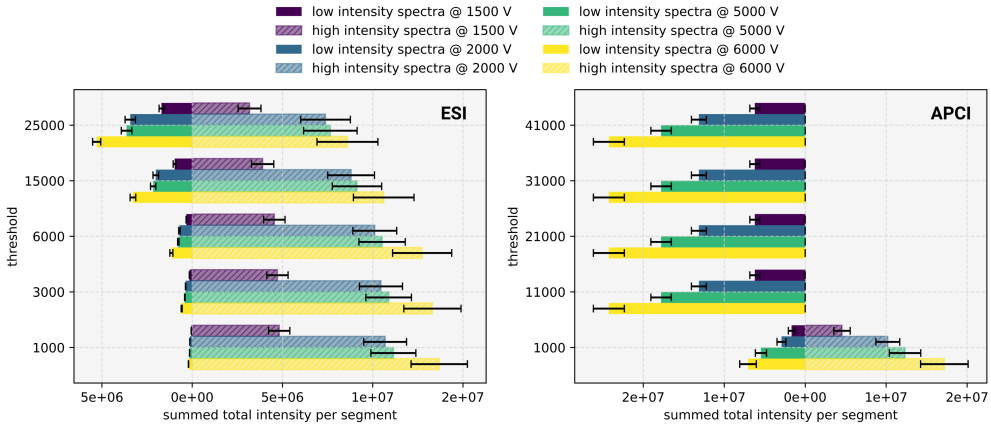

Fig. 6.7: Comparison of the summed total intensity per acquisition segment below and above different thresholds for ESI and APCI for selected capillary voltages.

3,000 counts. A surprising observation is that the vast majority of ESI spectra are "empty", as indicated by the first bar of the histograms in the left column in Figure 6.5. A closer inspection of the data shows that almost all counts in this histogram bin originate from entirely empty single spectra with an intensity of zero. The capillary voltage has almost no effect on the number of empty spectra recorded in ESI mode. Across all segments, approximately $90\,\%$ of all spectra recorded are essentially empty. Figure S1 of the supporting materials shows this in more detail. For variations in nebulizer pressure and drying gas flow, the proportion of empty spectra again remains around $90\,\%$ (see Figure S2 and Figure S3. In the case of drying gas variation, there is a notably higher scatter between the replicated experiments, leading to higher uncertainties. In contrast to ESI, the fraction of empty spectra in APCI mode remains very low for all parameters, ranging between 0 and $5\,\%$.

The histograms in Figure 6.5 and Figure 6.6 are divided into ranges of 0 to 3,000 and 3,000 to 300,000 counts, respectively, since nearly all APCI spectra have intensities below 3,000 counts. However, the distribution of the recorded intensity in a high and low-intensity tier for different thresholds reveals additional information about the intensity distribution in the single spectra. Therefore, the single spectra are separated into a low- and high intensity group, with intensities below and above a threshold value, respectively. Then, the sum of the intensities of all spectra in the respective group is calculated. This allows to assess which groups of single spectra contribute significantly to the observed ion signal in an analytical experiment, where thousands of raw spectra are summed for one recorded spectrum.

Figure 6.7 shows the result of this approach for different inlet capillary voltages and different thresholds for ESI and APCI. Nearly all ESI spectra are classified as having high intensity for a threshold of 1,000 counts, while a significant fraction of the

APCI spectra fall into the low-intensity category. At a threshold of 11,000 counts, the majority of ESI spectra are still in the high intensity classification, whereas all APCI spectra naturally remain below this threshold. This analysis provides evidence that in the case of ESI, the majority of signal intensity arises from a few high-intensity single spectra, while most single spectra remain empty. In contrast, APCI exhibits a narrow range of low-intensity single spectra with almost no empty spectra. This results in a summed spectrum where each single spectrum contributes to the total intensity.

In APCI, there is significantly less variance in the intensities of individual single spectra. ESI shows a much larger intensity scatter. The histograms show intensity distributions having a significantly longer tail towards higher intensity values. The shape and length of this tail depend on the ion source parameters. In contrast, APCI displays a relatively clear boundary towards the higher intensity range.

Droplet signatures are observed exclusively in ESI mode, and their occurrence depends on the capillary voltage, as shown in Figure 6.8. Most droplet signatures were observed at a capillary voltage of $2000\,\mathrm{V}$. Figure 6.8 also displays the mean intensity per segment; segments containing numerous single spectra with significantly higher total intensities result in an increased mean segment intensity. Figure 6.8 reveals that the acquisition segment at $2000\,\mathrm{V}$, which exhibits the highest droplet frequency, does not necessarily have the highest mean segment intensity. Instead, the highest mean segment intensity is observed at $4500\,\mathrm{V}$. It is likely that the recorded ion bursts or droplet signatures, respectively, are connected to the occurrence of single spectra with large total intensities since both vanish when APCI is used. Nevertheless, it seems that the current experimental configurations can only record specific droplet signatures. Since the oscilloscope triggers on the signal edge of the ion bursts, a comparably wide burst with no sharp edge will not be recognized by the current arrangement but could still lead to a higher intensity in the recorded single spectra. As a consequence, Figure 6.8 could indicate a shift in the apparent shape of droplet signatures from signals with a sharp edge in the case of $2000\,\mathrm{V}$ capillary voltage towards droplet signature pulses which are not observed with the oscilloscope in the current arrangement. However, the droplet frequency remains higher than zero for all capillary voltages. It is stressed that all measured droplet frequencies represent a lower limit, since the current experimental configuration cannot detect low-intensity or relatively wide ion signal bursts. The actual occurrence frequency of transient signal bursts at the SEM is most likely significantly higher.

The histograms for the variation of nebulizer pressure are also shown in the supporting materials. Figure S6 shows the results for ESI and Figure S7 for APCI. Similarly to Figure 6.9 and Figure 6.6, the histograms clearly demonstrate that the intensity distribution for APCI is much narrower as compared to ESI. However, in this case, the

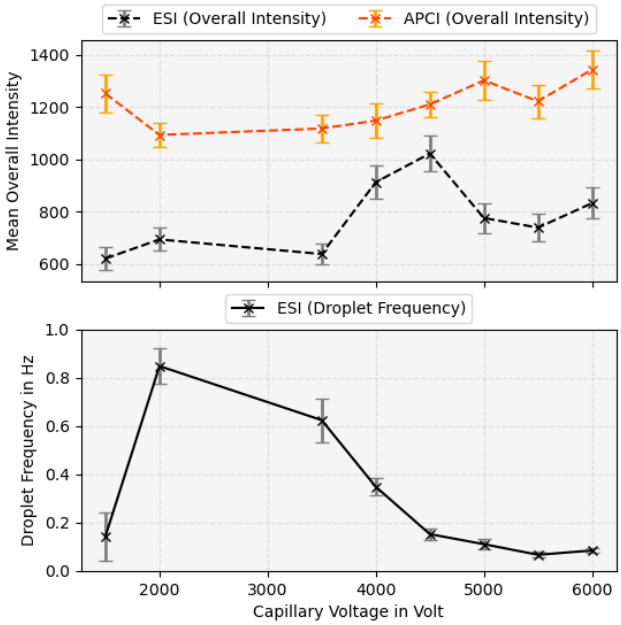

Fig. 6.8: Dependency of the mean overall intensity of the raw spectra and the droplet signature frequency on the capillary voltage. With APCI, no droplet signatures were observed. The error bars are the standard error of the mean values, calculated from the replicated measurements.

variation of the nebulizer pressure significantly affects the APCI intensity distribution, particularly at pressures below $2\,\mathrm{bar}$. The maximum total intensity remains below 3,000 counts. It appears as if in ESI mode, the nebulizer does not facilitate spray generation anymore at $0.2\,\mathrm{bar}$, since no spectra or droplet signatures are recorded, except during the brief transition between the acquisition segments.Figure S6 shows a relatively constant droplet signature frequency for all nebulizer pressures except for the $0.2\,\mathrm{bar}$ segment. The mean segment intensity remains fairly constant for pressures greater than $2.0\,\mathrm{bar}$. Data for pressures below $2.0\,\mathrm{bar}$ suggest that the nebulizer is either malfunctioning or the spray is not working as intended in this pressure regime.

The effect of varying the dry gas flow is shown in Figure S8 and Figure S9. Larger dry gas flows result in higher total intensities, i.e. more high-intense spectra in ESI mode. Figure S3 demonstrates that there is no clear relationship between dry gas flow and the number of empty spectra. Varying the dry gas flow has minimal impact on APCI results. Figure S5 shows that the droplet signature occurrence frequency peaks at $4\,\mathrm{L\,min^{-1}}$. There is also a peak in mean segment intensity at this flow rate, which was not observed when capillary voltages were changed. A minimum of mean segment intensity is observed at the same flow rate as for APCI, however, this may be coincidental.

6.4.3 Summed Raw Spectra

During normal operation of a TOF-MS the raw spectra are co-added in the spectrometer's hardware. For an exemplary measurement frequency of $1\,\mathrm{Hz}$ approx. 10,000 spectra will be co-added resulting in one mass spectrum per second transferred to the acquisition computer. It is currently not possible to record all single mass spectra with the used instrument due to the limited data transfer rate between the transient recorder card and the control computer and the limitations of the control software of the instrument. The system can record single spectra with approximately $50\,\mathrm{Hz}$, the data of all remaining TOF pulses are dropped. Nevertheless, the actually recorded single spectra can be combined into a summed mass spectrum in post-processing. During this process, we can also filter out single spectra for configurable conditions. This allows to co-add only spectra with a total intensity over 3,000 counts for comparison with co-added single mass spectra with a total intensity below 3,000 counts.

The result for the capillary variation experiment is depicted in Figure 6.9. The panels in the left column display the summed intensities for the high-intensity (orange) and low-intensity (black) single spectra, while the panels on the right show the normalized intensities. Remarkably, the co-added high-intensity mass spectra represent only about $3\,\%$ of the total recorded spectra but contribute significantly more total ion signal than the high frequency low-intensity spectra. The reserpine peak intensity of the summed low-intensity spectra ranges only from 0.8 to $9\,\%$ of the reserpine peak intensity of the combined high-intensity spectra, depending on the capillary voltage.

A similar trend is observed for variations of the nebulizer pressure depicted in Figure 6.10 and the dry gas flow. Interestingly, the top panel on the right side in Figure 6.10 shows that reserpine is exclusively found in the spectrum resulting from co-adding only high-intensity single spectra.

The analysis of the recorded data strongly suggests that co-added ESI spectra gain much of their intensity from the high-intensity single spectra, which we attribute to originate from sampling of aspirated droplets. Furthermore, the elimination of these droplets should then result in a significant reduction of the observed ion signals, unless it becomes possible to selectively trigger droplet fission before transfer, thereby generating a more continuous ion flow.

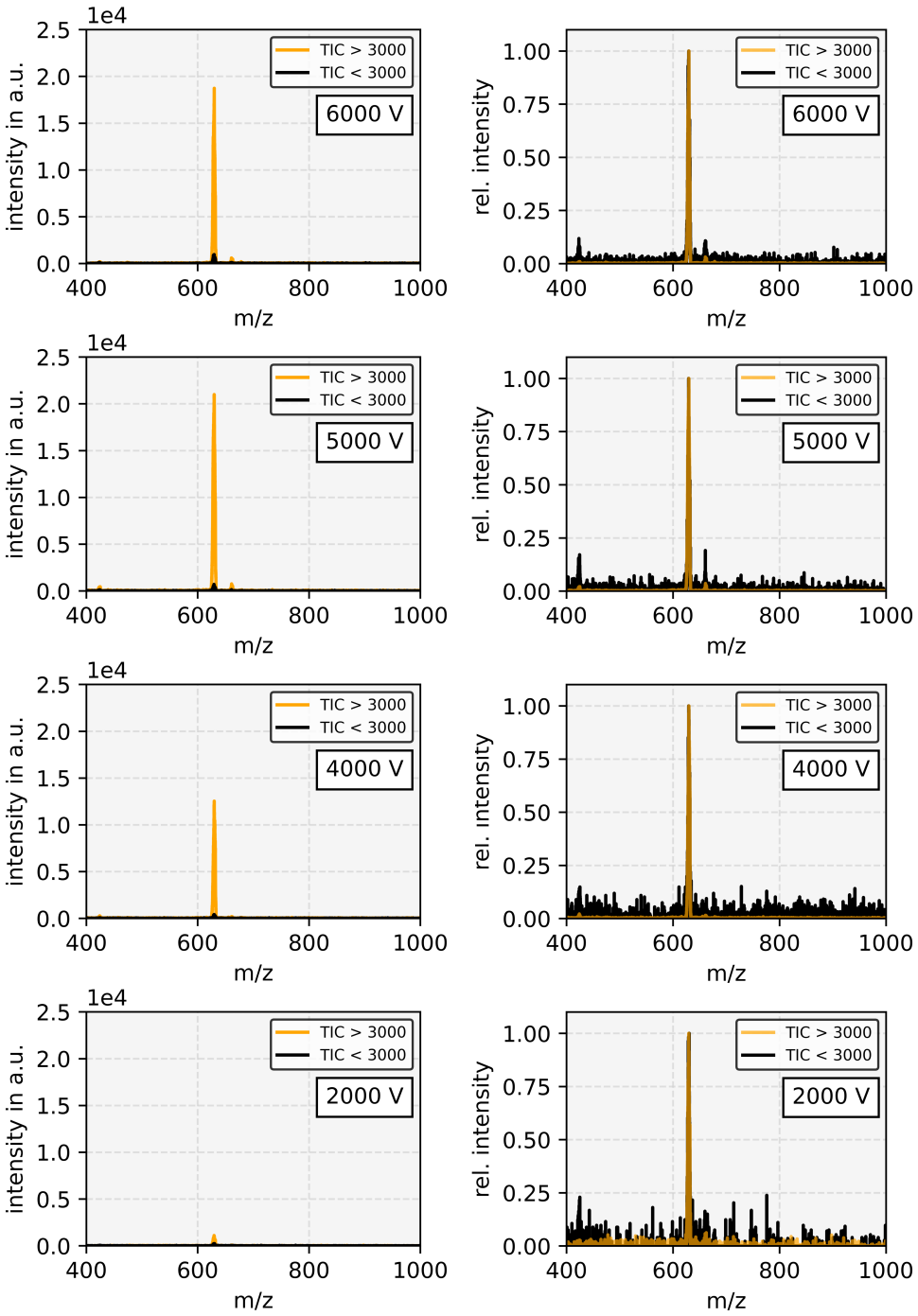

Fig. 6.9: Mass spectra calculated from different intensity groups, with raw spectra below 3,000 and above 3,000 counts, for different capillary voltages. The left column displays absolute and the right panel normalized intensities, respectively.

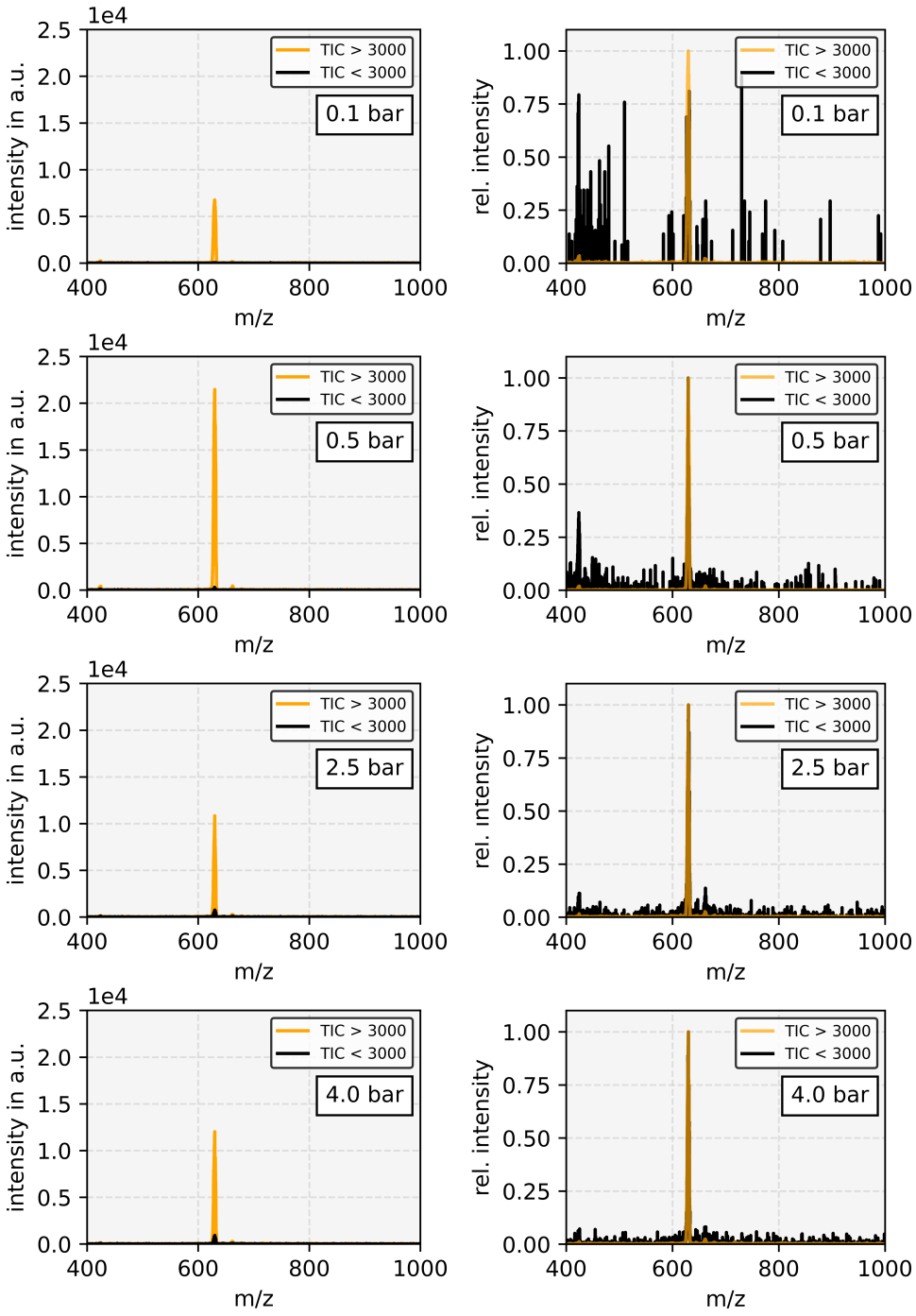

Fig. 6.10: Mass spectra calculated from different intensity groups, with raw spectra below 3,000 and above 3,000 counts, for different nebulizer pressures. The left column displays absolute and the right panel normalized intensities, respectively.

6.5 Conclusions

This study strongly suggests that signatures of aspirated droplets are visible in the statistics of the intensity distributions. Single mass spectra with outstanding large signals are a unique feature of ESI, while APCI produces a continuous and much smaller ion current without any signs of droplet aspiration.

The signatures of droplet show influence of various ESI source parameters, including capillary voltage, nebulizer pressure, and drying gas flow. The occurrence of high-intensity ion bursts (droplet signatures), recorded by the oscilloscope, is frequently observed, with an average frequency depending on the investigated parameters. In contrast, APCI mass spectra intensities remained almost constant, with a much narrower distribution of total single spectra intensities. The fact that the majority of single non-summed mass spectra in ESI were empty leads to the conclusion that a few ion burst/droplet signature events with high-intense single mass spectra make up the majority intensity of the summed mass spectra. Still unanswered is what causes the droplets to disintegrate to the observed ion bursts and where along the ion path of the instrument that fission actually takes place. The finding provides a possible explanation for the fact that the TIC fluctuates significantly more with ESI than APCI.

Optical monitoring of the spray stability confirmed that droplet signatures are not artifacts of temporary spray instabilities, but are ubiquitous during all carried-out ESI experiments. The results indicate that small variations in the source parameters may lead to significant changes in the ESI/spray dynamics resulting from, e.g., the fluid dynamics within the ionization chamber. All findings reinforce the importance of understanding the role of droplet dynamics in ESI-MS. The ability to detect and monitor droplet signatures in real-time provides valuable insights into the ionization process. It highlights the significant impact that instrument parameters have on mass spectrometric analysis. However, eliminating the aspiration of droplets would likely lead to a considerable reduction in overall ion intensity, since the present results suggest that aspirated droplets may contribute substantially to the recorded signal intensities in ESI-MS. Interesting, though, would be targeted fission of the droplets within the spray chamber to generate a more continuous ion beam and avoid contaminations within the high-vacuum regions.

6.6 Supporting Materials

- Additional plots containing the ratio of empty single non-summed spectra and the varied parameters for ESI and APCI.

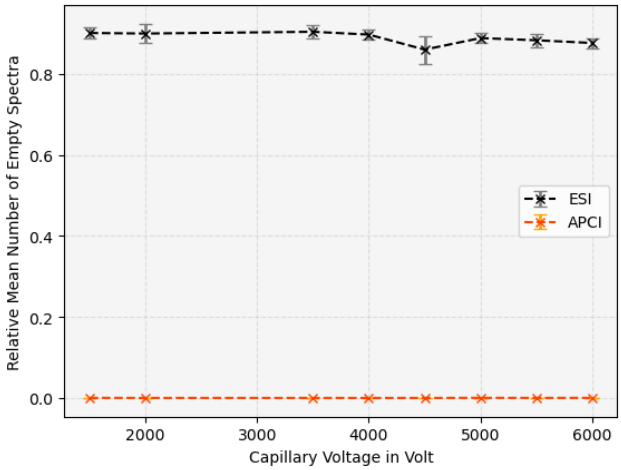

Fig. 6.S1: Ratio of empty single spectra and the varied capillary voltage for three replicate experiments in each mode, ESI and APCI.

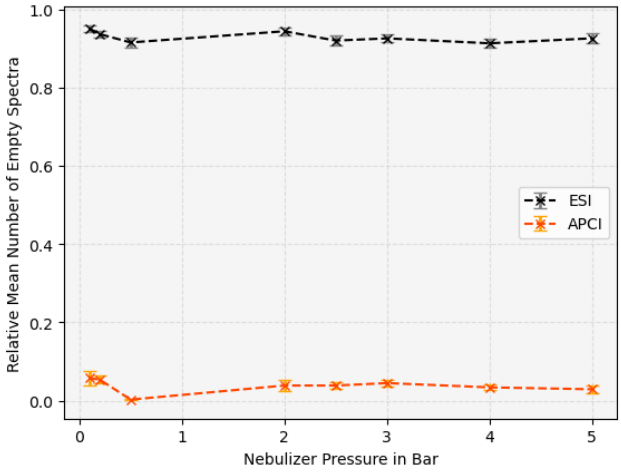

Fig. 6.S2: Ratio of empty single spectra versus the varied nebulizer pressure for three replicate experiments in each mode, ESI and APCI.

- Additional plots referring to Figure 6.8 for variation of the nebulizer pressure and drying gas flow.

- Additional histograms referring to Figure 6.5 and Figure 6.6 for variations of nebulizer pressure and drying gas flow.

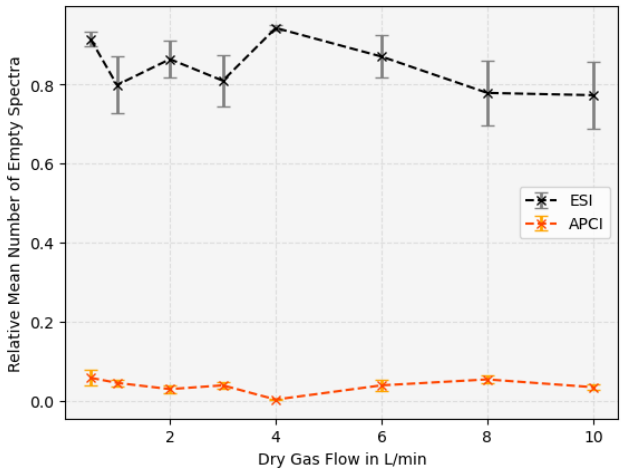

Fig. 6.S3: Ratio of empty single spectra versus the varied dry gas flow rate for three experimental sets in each mode, ESI and APCI.

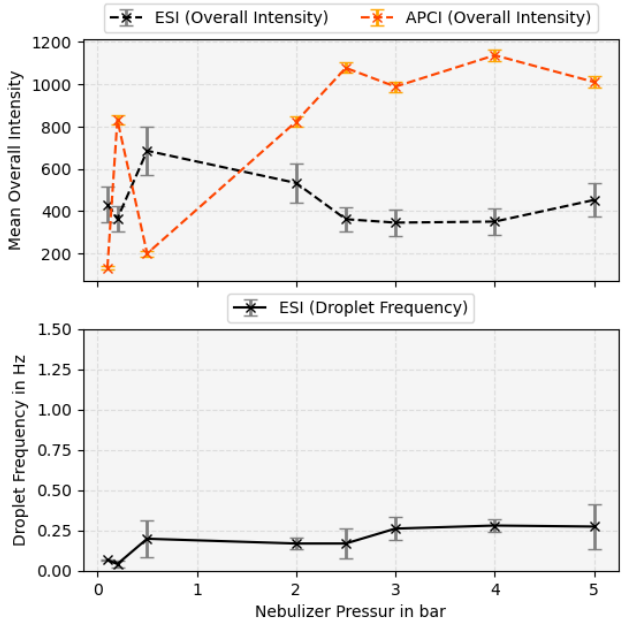

Fig. 6.S4: Dependency of the mean overall intensity of raw spectra and the droplet signature frequency on the nebulizer pressure. With APCI, no droplet signatures were observed. The error bars are the standard error of the mean values, calculated from the reproductions of the experiments.

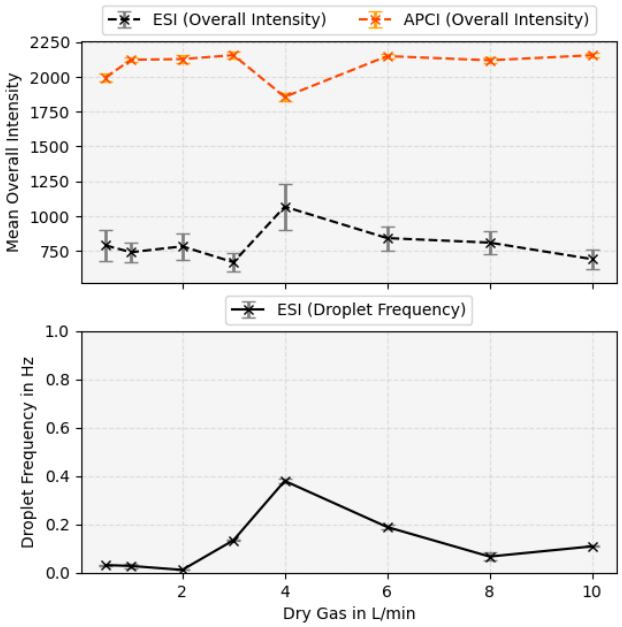

Fig. 6.S5: Dependency of the mean overall intensity of the raw spectra and the droplet signature frequency on the drying gas flow. With APCI, no droplet signatures were observed. The error bars are the standard error of the mean values, calculated from the replicated experiments.

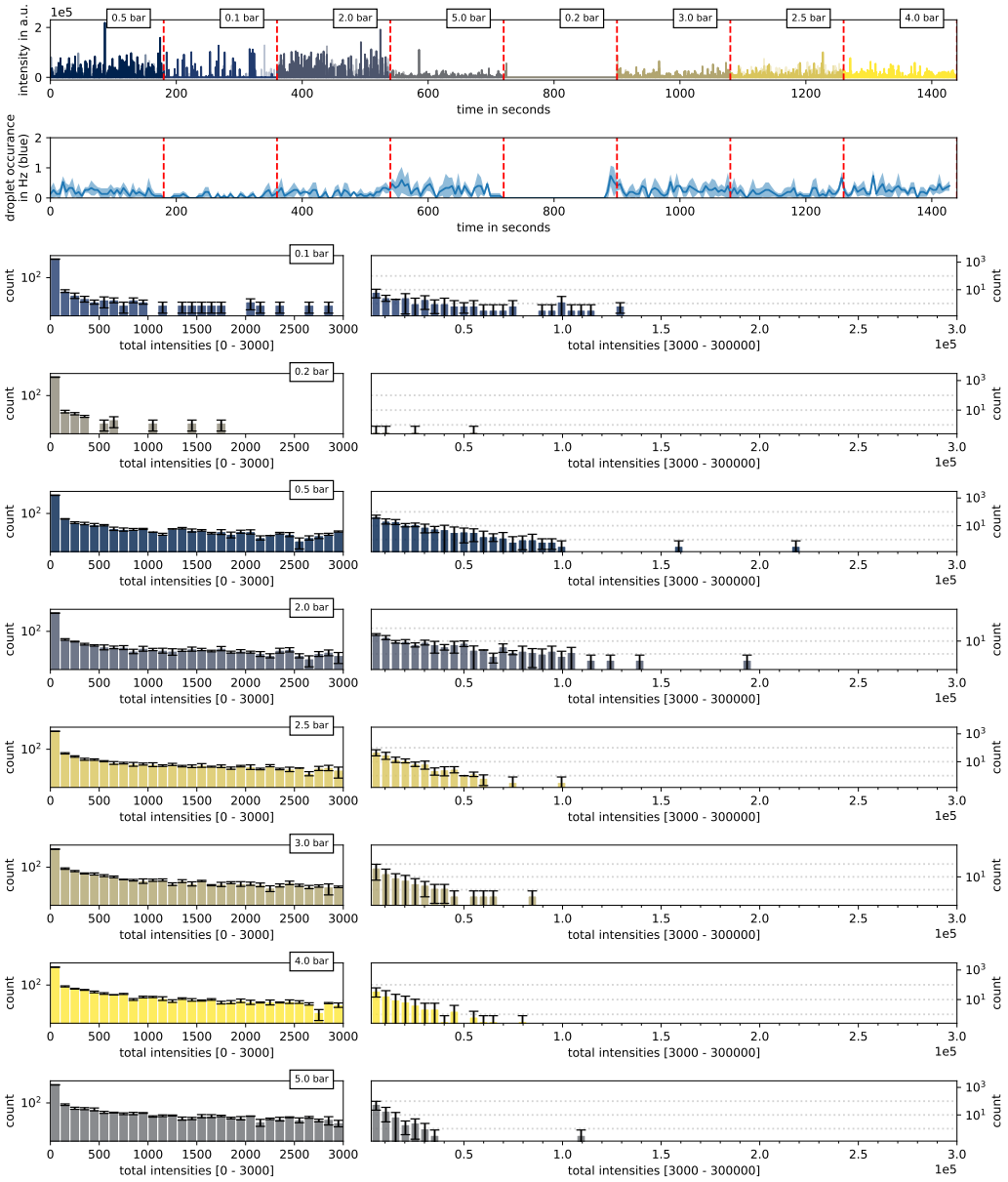

Fig. 6.S6: Histograms of the intensity distribution of single spectra at various nebulizer pressures in ESI mode. The top panel shows an overview chromatogram, while the second panel shows the droplet signature occurrence frequency. The values represent the mean of three replicate experiments, with error bars indicating the standard error of the mean. The histograms in the left column illustrate the intensity distribution for spectra with total intensities below 3,000 counts, while the right-side histograms display the corresponding distribution for intensities between 3,000 and 300,000 counts. Note that the histogram bins are different: Each bar in the left histograms represents intensities within a range of 100 counts, while the bars in the right histogram cover a range of 5,000 counts. The counts are displayed on a logarithmic scale.

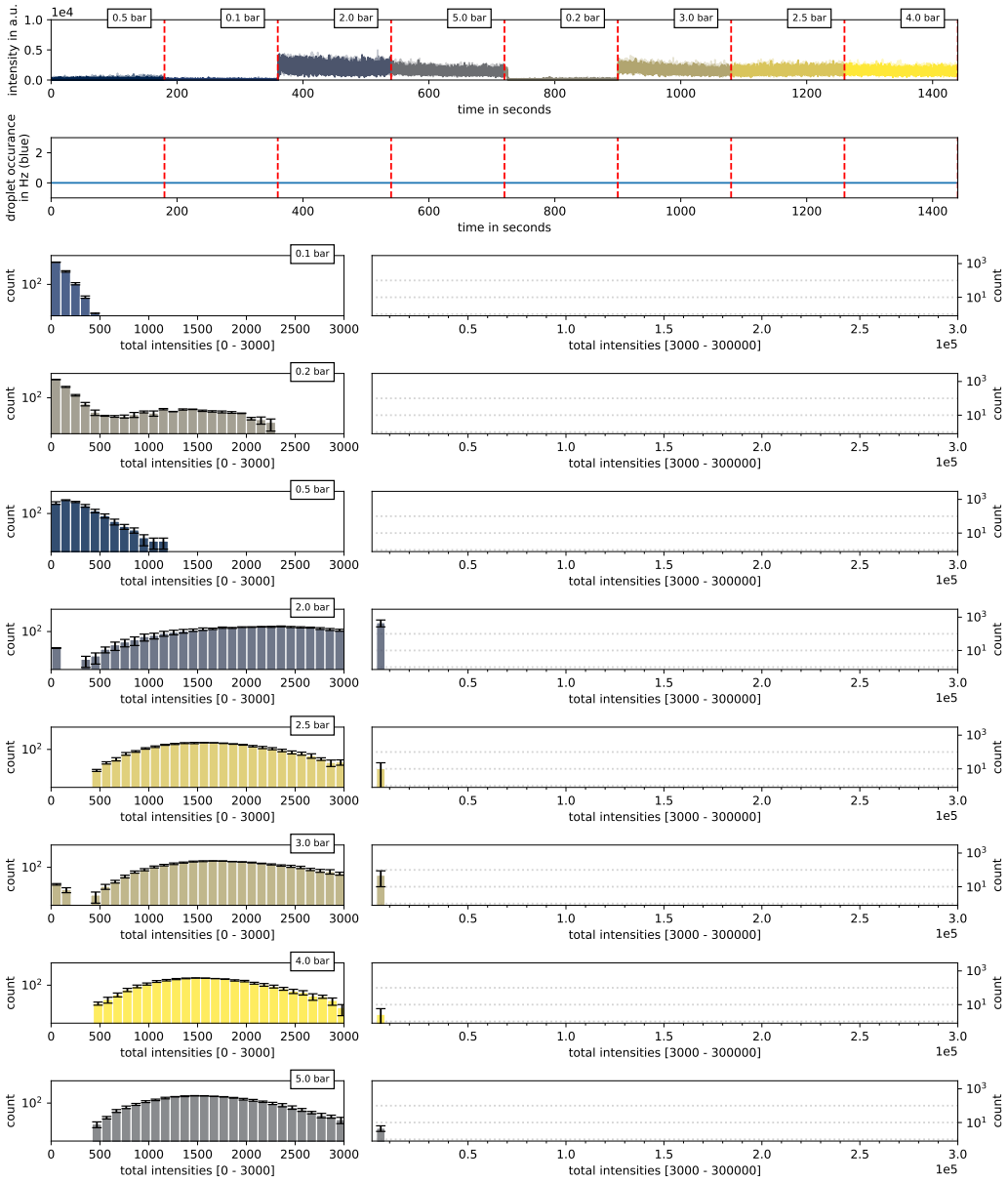

Fig. 6.S7: Histograms of the intensity distribution of single spectra at various nebulizer pressures in APCI mode, analogous to 6.S6. The top panel provides an overview chromatogram, while the second panel shows the droplet signature occurrence frequency. The values represent the mean of three recordings, with error bars indicating the standard error of the mean. The histograms in the left column illustrate the intensity distribution for spectra with total intensities below 3,000 counts, while the right-side histograms display the distribution for intensities between 3,000 and 300,000 counts. Each bar in the left histogram represents a range of 100 counts, while the bars in the right histogram cover a range of 5,000 counts. Counts are displayed on a logarithmic scale.

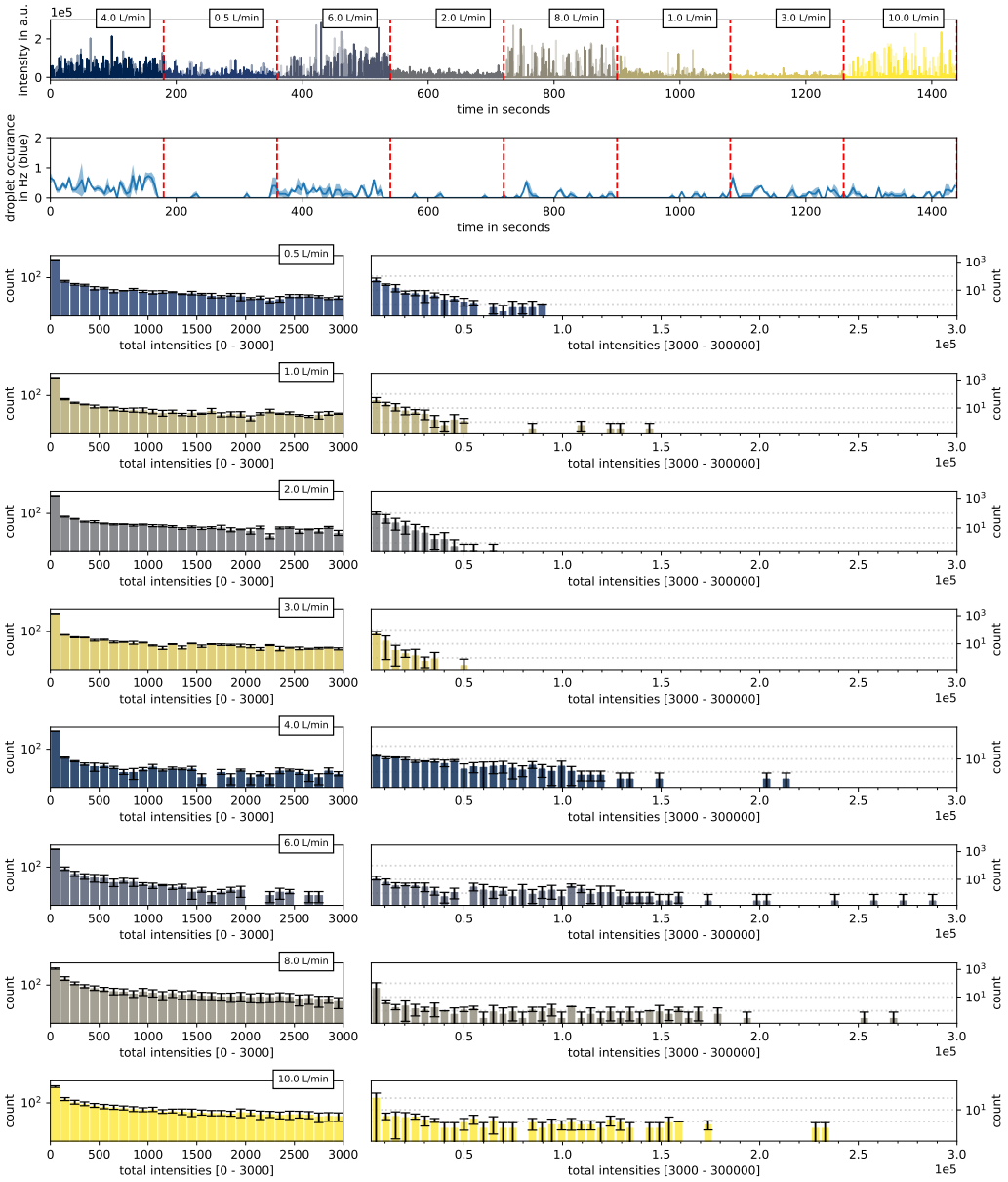

Fig. 6.S8: Histograms of the intensity distribution of single spectra at various dry gas flows in ESI mode. The top panel provides an overview chromatogram, while the second panel shows the droplet signature occurrence frequency. The values represent the mean of three recordings, with error bars indicating the standard error of the mean. The histograms in the left column illustrate the intensity distribution for spectra with total intensities below 3,000 counts, while the right-side histograms display the corresponding distribution for intensities between 3,000 and 300,000 counts. Note that the histogram bins are different: Each bar in the left histograms represents intensities within a range of 100 counts, while the bars in the right histogram cover a range of 5,000 counts. The counts are displayed on a logarithmic scale.

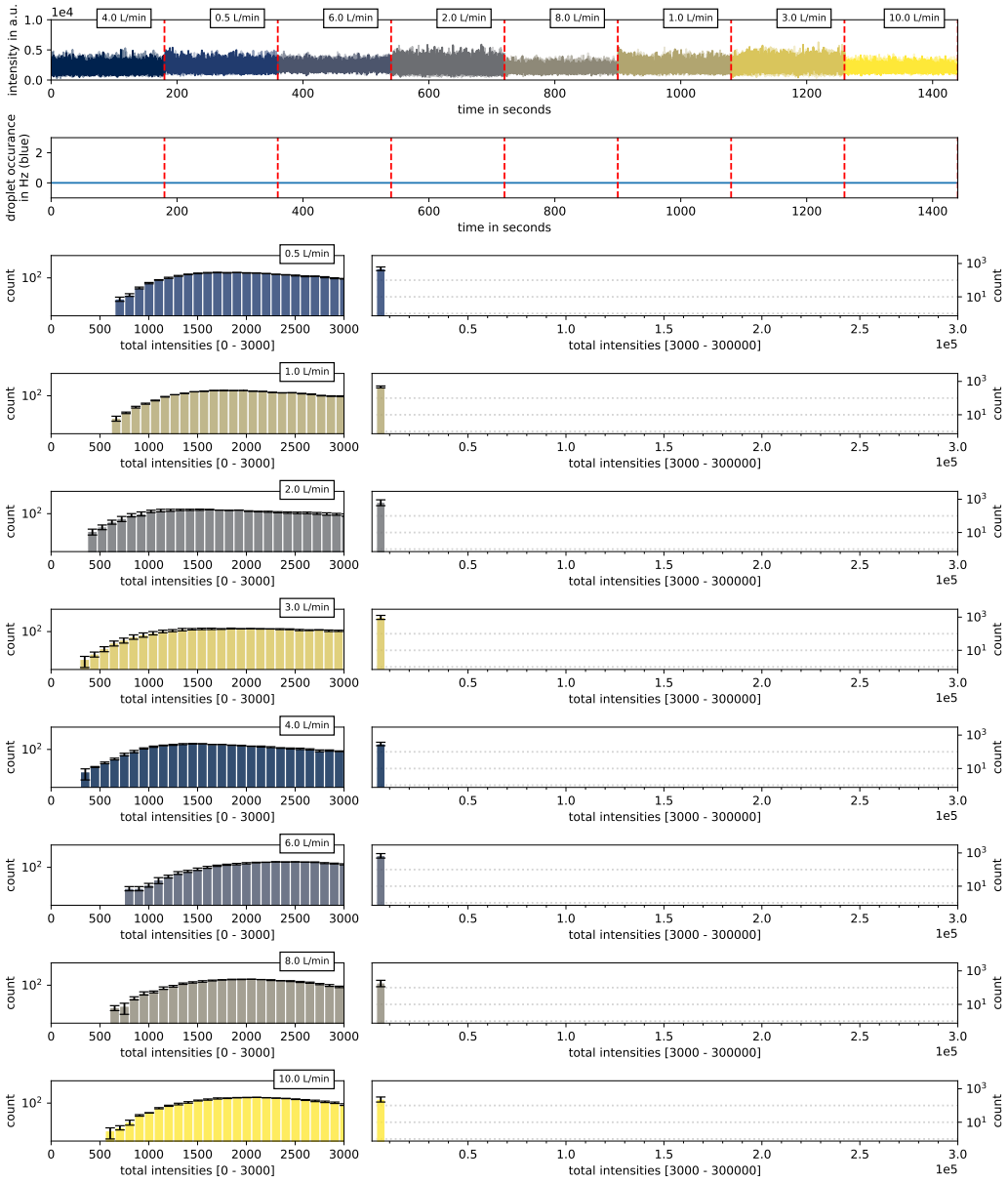

Fig. 6.S9: Histograms of the intensity distribution of single spectra at various dry gas flows in APCI mode, analogous to 6.S8. The top panel provides an overview chromatogram, while the second panel shows the droplet signature occurrence frequency. The values represent the mean of three recordings, with error bars indicating the standard error of the mean. The histograms in the left column illustrate the intensity distribution for spectra with total intensities below 3,000 counts, while the right-side histograms display the distribution for intensities between 3,000 and 300,000 counts. Each bar in the left histogram represents a range of 100 counts, while the bars in the right histogram cover a range of 5,000 counts. Counts are displayed on a logarithmic scale.

References

[1] Andries P. Bruins. „Mechanistic aspects of electrospray ionization“. In: *Journal of Chromatography A* 794 (1998), pp. 345–357 (cit. on p. 83).

[2] Richard B. Cole. *Electrospray and MALDI Mass Spectrometry*. Ed. by Richard B. Cole. John Wiley & Sons, Inc., Apr. 2010 (cit. on pp. 82, 83).

[3] Richard B. Cole. „Some tenets pertaining to electrospray ionization mass spectrometry“. In: *JOURNAL OF MASS SPECTROMETRY J. Mass Spectrom* 35 (2000), pp. 763–772 (cit. on pp. 82, 83).

[4] Thomas R. Covey, Bruce A. Thomson, and Bradley B. Schneider. „Atmospheric pressure ion sources“. In: *Mass spectrometry reviews* 28.6 (2009), pp. 870–897 (cit. on p. 83).

[5] Christopher D. Daub and Natalie M. Cann. „How are completely desolvated ions produced in electrospray ionization: Insights from molecular dynamics simulations“. In: *Analytical Chemistry* 83 (22 Nov. 2011), pp. 8372–8376 (cit. on p. 82).

[6] John B. Fenn, Matthias Mann, Chin Kai Meng, Shek Fu Wong, and Craig M. Whitehouse. „Electrospray Ionization for Mass Spectrometry of Large Biomolecules“. In: *Science* 246.4926 (1989), pp. 64–71. eprint: `https://www.science.org/doi/pdf/10.1126/science.2675315` (cit. on p. 82).

[7] Alfonso M. Gañán-Calvo, José M. López-Herrera, Miguel A. Herrada, Antonio Ramos, and José M. Montanero. „Review on the physics of electrospray: From electrokinetics to the operating conditions of single and coaxial Taylor cone-jets, and AC electrospray“. In: *Journal of Aerosol Science* 125 (Nov. 2018), pp. 32–56 (cit. on p. 82).

[8] Marion Girod, Xavier Dagany, Véronique Boutou, et al. „Profiling an electrospray plume by laser-induced fluorescence and Fraunhofer diffraction combined to mass spectrometry: Influence of size and composition of droplets on charge-state distributions of electrosprayed proteins“. In: *Physical Chemistry Chemical Physics* 14 (26 July 2012), pp. 9389–9396 (cit. on p. 82).

[9] Ronald L. Grimm and J. L. Beauchamp. „Evaporation and discharge dynamics of highly charged droplets of heptane, octane, and p-xylene generated by electrospray ionization“. In: *Analytical Chemistry* 74 (24 Dec. 2002), pp. 6291–6297 (cit. on p. 82).

[10] Jürgen H. Gross. *Mass Spectrometry*. Springer International Publishing, 2017 (cit. on pp. 82–84).

[11] Chris Heintz, Lisa Schnödewind, Oliver Braubach, et al. „Influence of polarity mode switching and standby times on signal stability and detection of aspirated droplet signatures in electrospray mass spectrometry“. In: *International Journal of Mass Spectrometry* 499 (May 2024), p. 117232 (cit. on pp. 83, 84, 86, 89, 91).

[12] Chris Heintz, Lisa Schnödewind, Oliver Braubach, et al. „Observation of Large, Charged Droplet Signatures within the High-Vacuum Region of a Commercial Electrospray TOF-MS“. In: *Journal of the American Society for Mass Spectrometry* (Feb. 2024) (cit. on pp. 83, 86, 89).

[13] Kenzo Hiraoka. *Fundamentals of Mass Spectrometry*. Springer New York, NY, June 2013 (cit. on pp. 82, 83).

[14] Edmond de Hoffmann and Vincent Strootbant. *Mass Spectrometry: Principles and Applications*. 3rd ed. John Wiley & Sons, 2007 (cit. on p. 83).

[15] Patricia Itzenhäuser, Ferdinand Max Wachter, Laura Lehmann, et al. „Dynamics of the Aspiration of Charged Droplets into a LC-ESI-MS System“. In: *Journal of the American Society for Mass Spectrometry* (Sept. 2024) (cit. on p. 83).

[16] Reinhard Juraschek, Thomas Dülcks, and Michael Karas. „Nanoelectrospray - More than just a minimized-flow electrospray ionization source“. In: *Journal of the American Society for Mass Spectrometry* 10.4 (1999), pp. 300–308. eprint: `https://doi.org/10.1016/S1044-0305(98)00157-3` (cit. on p. 82).

[17] P. Kebarle. *A brief overview of the present status of the mechanisms involved in electrospray mass spectrometry*. 2000 (cit. on pp. 82, 83).

[18] P. Kebarle and M. Peschke. „On the mechanisms by which the charged droplets produced by electrospray lead to gas phase ions“. In: *Analytica Chimica Acta* 406 (2000), pp. 11–35 (cit. on p. 83).

[19] Paul Kebarle and Liang Tang. „From ions in solution to ions in the gas phase - the mechanism of electrospray mass spectrometry“. In: *Analytical Chemistry* 65.22 (1993). PMID: 22881012, 972A–986A (cit. on p. 82).

[20] Sunil Kumar, Awantika Singh, Vikas Bajpai, et al. „Structural characterization of monoterpene indole alkaloids in ethanolic extracts of Rauwolfia species by liquid chromatography with quadrupole time-of-flight mass spectrometry“. In: *Journal of Pharmaceutical Analysis* 6 (6 Dec. 2016), pp. 363–373 (cit. on p. 86).

[21] Clara Markert, Marco Thinius, Laura Lehmann, et al. „Observation of charged droplets from electrospray ionization (ESI) plumes in API mass spectrometers“. In: *Analytical and Bioanalytical Chemistry* 413 (22 Sept. 2021), pp. 5587–5600 (cit. on pp. 83, 86).

[22] J. Fernandez De La Mora and I G Loscertales. „The current emitted by highly conducting Taylor cones“. In: *J. Fluid Mech* 260 (1994), pp. 155–184 (cit. on pp. 82, 83).

[23] J. Fernandez De La Mora, J Navascues, F Fernandez, and J Rosell-Llompart. „Generation of submicron monodisperse aerosols in electrosprays“. In: *Journal of Aerosol Science* 21 (1990), pp. 673–676 (cit. on p. 82).

[24] Peter Nemes, Ioan Marginean, and Akos Vertes. „Spraying Mode Effect on Droplet Formation and Ion Chemistry in Electrosprays“. In: *Analytical Chemistry* 79 (8 Apr. 2007), pp. 3105–3116 (cit. on pp. 82, 83).

[25] Michelle Rajkovic, Thorsten Benter, and Walter Wißdorf. „Investigation of Surface-Induced Dissociation Processes via Molecular Dynamics Simulations of Wall Collisions of Large Droplets Produced by Electrospray Ionization“. In: *Journal of the American Society for Mass Spectrometry* 36 (4 Apr. 2025), pp. 760–770 (cit. on p. 83).

[26] Ioan Marginean Ryan T. Kelly and Keqi Tang. *Encyclopedia of Microfluidics and Nanofluidics*. Springer New York, 2015 (cit. on pp. 82, 83).

[27] Andrea Schmidt, Michael Karas, and Thomas Dülcks. „Effect of different solution flow rates on analyte ion signals in nano-ESI MS, or: When does ESI turn into nano-ESI?“ In: *Journal of the American Society for Mass Spectrometry* 14 (5 2003), pp. 492–500 (cit. on p. 82).

[28] James N. Smith, Richard C. Flagan, and J. L. Beauchamp. „Droplet evaporation and discharge dynamics in electrospray ionization“. In: *Journal of Physical Chemistry A* 106 (42 Oct. 2002), pp. 9957–9967 (cit. on p. 82).

[29] Daniel C. Taflin, Timothy L. Ward, and E. James Davis. „Electrified droplet fission and the Rayleigh limit“. In: *Langmuir* 5.2 (1989), pp. 376–384 (cit. on pp. 82, 83).

[30] Andre Venter, Paul E. Sojka, and R. Graham Cooks. „Droplet dynamics and ionization mechanisms in desorption electrospray ionization mass spectrometry“. In: *Analytical Chemistry* 78 (24 Dec. 2006), pp. 8549–8555 (cit. on p. 82).

[31] Arno Wortmann, Anna Kistler-Momotova, Renato Zenobi, et al. „Shrinking Droplets in Electrospray Ionization and Their Influence on Chemical Equilibria“. In: *Journal of the American Society for Mass Spectrometry* 18 (3 Mar. 2007), pp. 385–393 (cit. on p. 82).

[32] Zijie Xia and Evan R. Williams. „Effect of droplet lifetime on where ions are formed in electrospray ionization“. In: *The Analyst* 144 (1 2019), pp. 237–248 (cit. on p. 83).

7 Summary and Conclusion

7.1 Appearance and Recording

7.1.1 Waveforms in Oscillogram

Connecting an oscilloscope to the auxiliary SEM detector enabled the direct monitoring of the ion current passing through the oa-stage of the Bruker micrOTOF. By using an appropriate input impedance, the ion current and push signals within the oa-stage could be observed in oscillograms.

The oscillograms reveal regular, wide pulses of very high intensity in the ion current. These anomalies, which are referred to throughout this text as ion bursts, have been considered to be signatures of aspirated droplets. It is ruled out that monolithic particles striking the SEM detector generate the observed signals, since the pusher can cut out entire sections of the signal. Instead, the observed signals are most probably generated by dense ion clouds of unknown composition, possibly containing bare ions and clusters, which are a result of fragmented droplets. Going further, several conclusions are drawn:

The intensity and width of the recorded ion bursts vary even though other parameters were kept constant, as pictured in Figure 7.1. It is most likely that the location of the fission and thus the geometry of the ion bursts leads to variations in their appearance in the oscillograms. For instance, a brief but intense signal could indicate that the burst is denser than a wider, less intense signal. Furthermore, it is unclear where the initially monolithic droplet undergoes fission and transforms into a highly correlated ion burst. The ion burst signal shape may correspond to the fission location, as earlier fissions would result in a more elongated ion burst. All burst components must be charged and will repel each other, resulting in an increasing volume over a longer flight time.

Figure 7.2 shows the burst width distribution of an experiment under typical analytical conditions. Assuming that the burst width results from a combination of the location of the droplet's fission and the size of the droplet, one can deduce that there is a favored fission area and a usual range of droplet sizes.

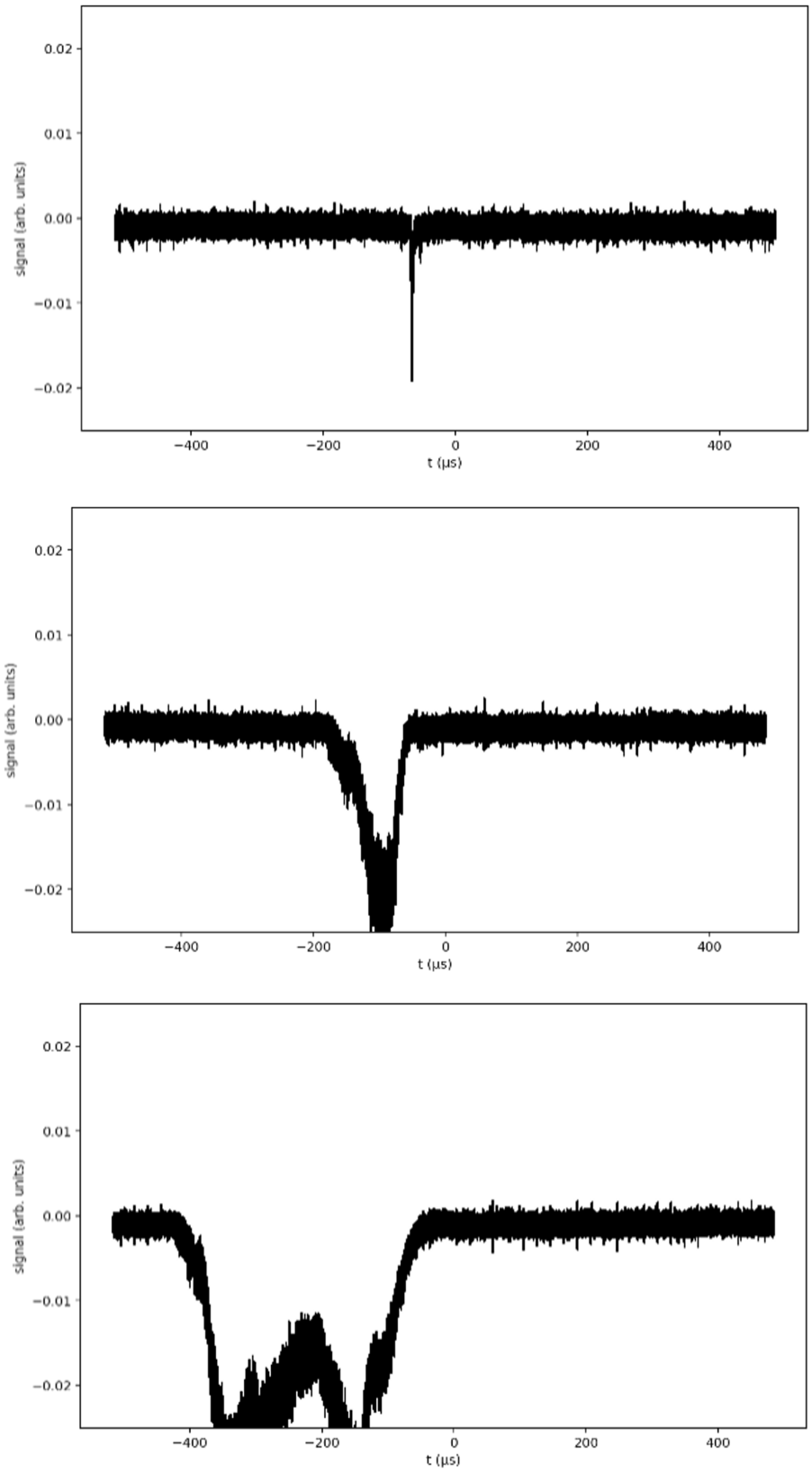

Fig. 7.1: Collection of sampled ion burst oscillograms with different shapes. All ion bursts were recorded during one experiment with the same set of parameters.

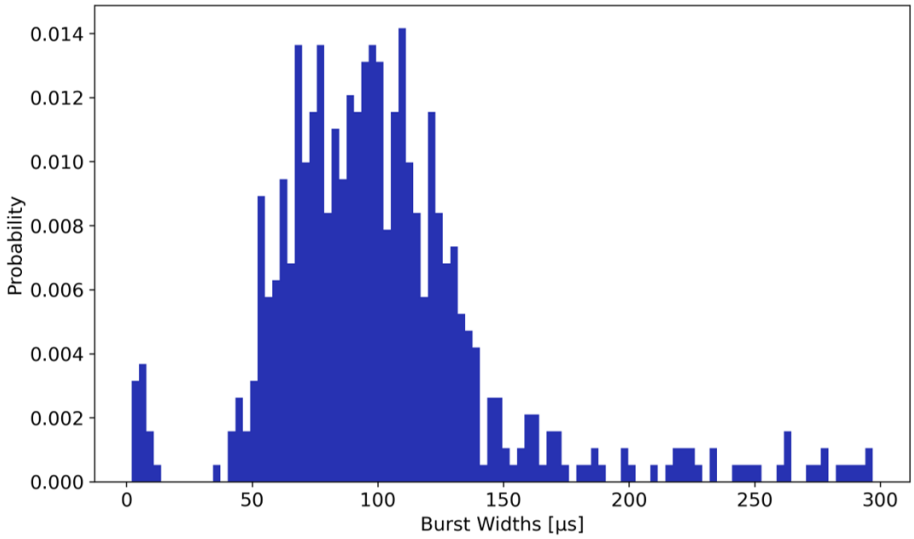

Fig. 7.2: Ion bursts width distribution during one experiment under typical analytical conditions.

7.1.2 Dependence of Source and Transfer Parameters

The appearance of ion bursts and their frequency correspond to several source and transfer parameters. Regarding the source parameters, all factors critical for spray generation, such as capillary voltage, liquid flow, nebulizer gas flow, drying gas flow, and drying gas temperature, exert a moderate to high influence on the ion burst frequency but have no clear impact on the burst's signal shape. In contrast, varying the radio frequency (RF) of the hexapoles significantly affects the appearance of the burst signal, as demonstrated in Figure 7.3.

Remarkably, the shape of the observed ion burst signals depends on the amplitude of the hexapole RF. The complex signal shape per amplitude setting is highly reproducible across different RF amplitudes. The direct connection between hexapole RF and signal shape strongly suggests that the hexapole region is a critical location for droplet fragmentation. However, the observation of reproducible signal shapes in this experiment is limited to a specific set of source and transfer parameters. Additionally, the shown oscillograms are explicitly selected examples; occasionally, there are ion bursts that do not match the pattern. For this specific experiment, the location of fission is likely primarily in the hexapole area, but it generally varies depending on the source, transfer, and other unknown parameters.

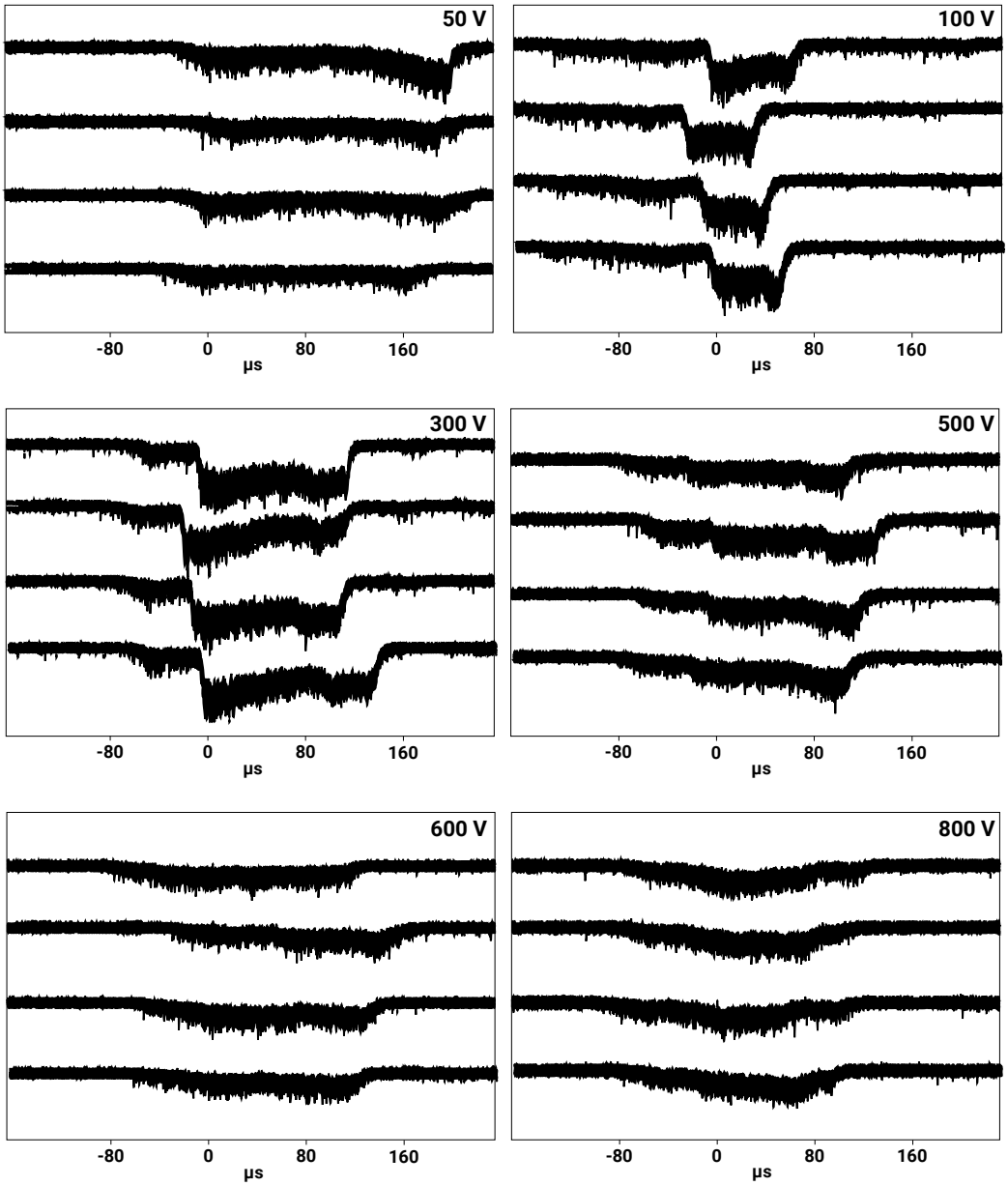

Fig. 7.3: Examples of observed ion burst signals in dependence on the hexapole RF amplitude

7.1.3 Comparison to other Ionization Techniques

Some experiments were also conducted using APCI and APPI techniques to eliminate potential sources for the droplet signatures other than ESI. None of the experiments resulted in ion bursts, which strongly supports the hypothesis that solely ESI generates them.

7.2 Individual Non-Summed TOF mass spectra

7.2.1 Dependence of Source Parameters

A second method for directly demonstrating the existence of droplet signatures involved examining the (non-summed) individually recorded TOF spectra. Typically, a TOF instrument averages around 10^4 spectra per second before transmitting the data to the computer, owing to electronic data transmission speed limitations. Nevertheless, capturing about fifteen of these single spectra per second was possible for troubleshooting purposes with the microTOF.

The analysis of single spectra initially revealed that most of the recorded spectra were empty. Occasionally, individual spectra exhibited very intense signals. The fact that TOF instruments typically sum thousands of these single mass spectra explains why the empty spectra have remained undiscovered; the summation process averaged them out.

Another finding indicated that the distribution of the total intensities of the individual spectra depends on ion source parameters. Additionally, the source parameters appear to have only a minor influence on the number of empty spectra. However, certain sets of parameters lead to more spectra with very high intensities, while others tend to narrow the distribution of total intensities.

7.2.2 Connection to ion bursts

It is reasonable to assume that the blanks in the ion burst signals, caused by the TOF pushes, contribute to the observed very intense individual spectra. Unfortunately, providing indisputable evidence for this assumption has not yet been possible. One issue is the synchronization between the SEM and MCP data. A potential solution may be the proposed custom HV switch for the TOF pusher (see section 2.12).

7.2.3 Comparison to other Ionization Techniques

Experiments with APCI indicate that the phenomena observed are caused by ESI rather than other factors. The experiments demonstrate that singular, highly intense, single mass spectra are characteristic of ESI. In contrast, the total intensity distribution for APCI experiments is consistently narrower and less dependent on ion source parameters. Additionally, there are virtually no entirely empty single spectra with APCI, in contrast to the high number of empty spectra obtained with ESI.

7.3 Long-Term Experiments

7.3.1 Signal Stability

Long-term experiments revealed instabilities within the first hour, as indirectly noted by manufacturers recommending a warm-up time of $30\,\mathrm{min}$ to $60\,\mathrm{min}$. During this initial period, analyte and TIC signals fluctuate, while high rates of droplet signatures are observed at the SEM. After this warm-up period, the droplet signature frequency decreases over a few hours to a low level, but it never completely vanishes.

When repeating the experiments, it became evident that the next initial warm-up time is shorter if there is a brief interval between experiments. A delay of $1\,\mathrm{d}$ to $2\,\mathrm{d}$ results in the complete signal recovery of the droplet signature frequency and the original warm-up time of approximately $30\,\mathrm{min}$ to $60\,\mathrm{min}$. The same effect was observed when switching the polarity mode. After a few minutes in the opposite polarity mode, the droplet signature frequency fully recovered.

Some data suggested that the spray started to oscillate after a specific period. Optical monitoring was implemented to determine whether spray instability leads to the production of larger-than-average droplets in the spray chamber, for instance. However, the recorded images do not indicate that spray instabilities are the cause of these observations. Nevertheless, the optical spray data correlate with the ion current measured in the spray chamber by the micrOTOF.

8 Outlook

8.1 Further Experiments on Other Instruments

The existence of droplet signatures was successfully demonstrated for the Bruker micrOTOF as well as for other instruments by Markert *et al.* [2], as mentioned in section 1.2. The next step would be to replicate some of the experiments from this work, which were performed using the Bruker micrOTOF, on other instruments with a different setup.

Itzenhäuser *et al.* [1] already performed promising statistical analyses of single spectra recorded with a Bruker amaZon ETD quadrupole ion trap. They investigated the impact of different solvents on the intensity distribution of single, non-summed mass spectra. Reproducing these experiments with other commercial instruments would be very valuable in understanding the underlying principles and mechanisms that result in the recorded spectra. Instruments that do not provide single, non-summed spectra recording could be connected to a custom transient recorder.

Additionally, as mentioned throughout this work, many unanswered questions remain regarding the appearance, fission, and composition of droplet signatures. Laser scattering events in the desolvation unit of the Bruker micrOTOF or other commercial instruments would yield essential details about the combustion of the gas flow containing bare ions and droplets. However, implementing such an experiment within a commercial instrument is challenging.

Knowing the exact composition of the observed ion bursts would also be very interesting. To achieve this, among other things, the manual HV switch from section 2.12 would be of great value, as well as other detection methods upstream of the orthogonal acceleration stage, as, for instance, a charge detection system.

8.2 Dependence of Different Analyte Systems

Itzenhäuser [1] and Markert [2] showed that the observed ESI droplet phenomena are strongly dependent on the used analyte as well as the solvent system. A significant

open question is whether a different chemistry occurs within droplets of varying composition. This work shows that individually recorded mass spectra with low total intensity and those with high total intensity show similar mass signals, but with different intensity distributions of those signals. In the case of proteins, it could be possible that charge states differ between bare proteins inside the gas flow and proteins inside the droplets, which a detailed analysis of non-summed mass spectra could detect.

References

[1] Patricia Itzenhäuser, Adem Bulut, Chris Heintz, et al. „Statistical Analysis of Aspirated Charged Droplet Signatures in Non-summed Mass Spectra from various commercial LC-ESI-MS Systems“. In: *Proceedings ASMS 2024, Anaheim*. 2024 (cit. on p. 117).

[2] Clara Markert, Marco Thinius, Laura Lehmann, et al. „Observation of charged droplets from electrospray ionization (ESI) plumes in API mass spectrometers“. In: *Analytical and Bioanalytical Chemistry* 413 (22 Sept. 2021), pp. 5587–5600 (cit. on p. 117).

List of Figures

List of Tables

Declaration

I hereby declare that I have composed the submitted dissertation independently. Furthermore, I confirm that in the preparation of this work, I have used only the resources and aids referenced in the dissertation, and that all passages taken verbatim or in essence from other sources have been clearly identified as such.

Wuppertal, May 15, 2025

Chris Vico Heintz